Longitudinal Diagnostics for Beam-Based Intra Bunch-Train Feedback at FLASH and the European XFEL

Dissertation
zur Erlangung des Doktorgrades
an der Fakultät für Mathematik, Informatik und Naturwissenschaften
Fachbereich Physik
der Universität Hamburg

vorgelegt von

Hannes Dinter
aus Erfurt

Hamburg

2018

Gutachter der Dissertation:	Prof. Dr. Florian Grüner PD Dr. Bernhard Schmidt
Zusammensetzung der Prüfungskommission:	Prof. Dr. Florian Grüner PD Dr. Bernhard Schmidt Prof. Dr. Günter Sigl Prof. Dr. Wolfgang Hillert Prof. Dr. Wilfried Wurth
Vorsitzender der Prüfungskommission:	Prof. Dr. Günter Sigl
Datum der Disputation:	19.06.2018
Vorsitzender des Fach-Promotionsausschusses PHYSIK:	Prof. Dr. Wolfgang Hansen
Leiter des Fachbereichs PHYSIK:	Prof. Dr. Michael Potthoff
Dekan der Fakultät MIN:	Prof. Dr. Heinrich Graener

Abstract

Diagnostics and control of the electron beam parameters in order to provide stable and reproducible experimental conditions for the photon users are a crucial part of operating a free-electron laser. For the beam-based longitudinal feedback at FLASH and the European XFEL, three monitor types are discussed: bunch arrival time monitor (BAM), bunch compression monitor (BCM) and synchrotron radiation monitor (SRM). The influence of the amplitudes and phases of the accelerating modules on the electron beam properties is studied analytically, with simulations and in measurements. For the simulations, models of the monitors are integrated into an existing longitudinal particle tracking code and a beam-based feedback framework is developed.

An upgrade of the electro-optical units for the BAMs at FLASH and the European XFEL as well as the development of a BCM for the European XFEL are required. All monitors need to be installed, commissioned and characterised. The bunch pattern at FLASH and the European XFEL allowing for the generation of many thousand photon pulses per second with repetition rates up to several megahertz makes great demands on the beam diagnostics and controls. An intra-train feedback is required for stabilising the electron beam parameters along the bunch train. The feedback performance must be evaluated and the control parameters need to be optimised.

Kurzdarstellung

Diagnose und Kontrolle der Elektronenstrahlparameter zwecks Bereitstellung stabiler und reproduzierbarer Experimentierbedingungen für die Photonennutzer*innen sind entscheidend für den Betrieb eines Freie-Elektronen-Lasers. Für das strahlbasierte longitudinale Feedback bei FLASH und am Europäischen XFEL werden drei Arten von Monitoren betrachtet: Bunchankunftszeitmonitor (BAM), Bunchkompressionsmonitor (BCM) und Synchrotronstrahlungsmonitor (SRM). Der Einfluss der Amplituden und Phasen der Beschleunigermodule auf die Elektronenstrahleigenschaften wird analytisch, mit Simulationen und in Messungen untersucht. Für die Simulationen werden Modelle der Monitore in einen existierenden Teilchentrackingcode integriert und ein strahlbasiertes Feedback-Framework entwickelt.

Ein Upgrade der elektro-optischen Einheiten für die BAMs bei FLASH und am Europäischen XFEL sowie die Entwicklung eines BCMs für den Europäischen XFEL sind erforderlich. Alle Monitore müssen installiert, in Betrieb genommen und charakterisiert werden. Das Bunchschema bei FLASH und am Europäischen XFEL, welches die Erzeugung vieler tausend Photonenpulse pro Sekunde mit Wiederholraten bis zu mehreren Megahertz ermöglicht, stellt große Anforderungen an die Strahldiagnose und -kontrollen. Ein Intra-Train-Feedback wird zur Stabilisierung der Elektronenstrahlparameter entlang des Bunchzuges benötigt. Die Leistungsfähigkeit des Feedbacks ist zu beurteilen und die Kontrollparameter müssen optimiert werden.

Contents

List of Figures

List of Tables

Preface

Free-electron lasers (FELs) provide ultrashort, high intensity photon pulses for the use in numerous fields of research. The radiation is generated in a self-amplifying spontaneous process by relativistic electron bunches travelling through periodic magnetic structures. The properties of the FEL radiation – such as wavelength, intensity and pulse duration – are determined by the electron beam parameters and the magnetic field geometry. In order to provide stable and reproducible experimental conditions for the photon users, diagnostics and control of the electron beam are a crucial part of operating an FEL.

The FEL facilities FLASH and European XFEL feature a unique bunch pattern consisting of macropulses with a repetition rate of 10 Hz, each comprising bursts of several hundreds of bunches. This scheme enables the generation of many thousand photon pulses per second, allowing for a significant reduction of the required measurement time in the user experiments due to the high event rate and the large mean photon flux. The high bunch repetition rates of up to several megahertz make great demands on the beam diagnostics and stabilisation systems. In order to detect and correct deviations of the beam properties on a shot-to-shot basis, fast diagnostics and a low-latency intra bunch-train feedback strategy are required.

The concepts and methods used throughout this thesis are based on various fields of previous work done by the respective authors. The bunch arrival time monitor has been developed by [Löh09] and was further optimised by [Boc12]. Bunch compression monitors at FLASH have first been described by [Gri07], the current state is detailed in [Wes12]. A synchrotron radiation monitor formerly installed in the magnetic chicane of the first bunch compressor at FLASH is presented in [Ger07] and [WG09].

Beam-based feedback at FLASH, both intra bunch-train and from macropulse to macropulse, has been demonstrated by [LAF+10] and [KBB+10]. An improved controller design and the optimisation of the feedback parameters are shown in [Pfe14]. The integration of the slow longitudinal feedback into the accelerator control system at FLASH is described in [KS14].

Motivation and Relevance

Based on these foundations, several topics requiring further attention have been identified. They comprise necessary upgrades as well as new developments of the respective subsystems to improve the measurement resolution and the reliability of components.

This thesis presents the relevant process steps as well as the results and findings obtained during the course of this work.

For the implementation of an intra bunch-train feedback system, fast beam diagnostics providing bunch-resolved measurements and low-latency data transfer are required: at the European XFEL, the minimum bunch distance within the macropulse is 222 ns, at FLASH 1 µs. This can be achieved by employing diagnostics which directly measure beam properties or quantities proportional to these without the need of interposed model computations.

For the scope of this work, bunch arrival time and compression monitors as well as synchrotron radiation monitors have been studied. Depending on the detector type and the requirements defined by the employed feedback scheme – such as the needed measurement resolution and limits for the system bandwidth and delay – the used components and involved subsystems must be characterised and tested for their suitability for this purpose.

An upgrade of the electro-optical unit of the bunch arrival time monitors is needed to increase the system bandwidth for improving the measurement resolution for small bunch charges below 100 pC. In addition, the existing detectors can only provide information for a single sub-bunchtrain. In order to support the newly available multi-beamline operation at FLASH and the European XFEL, an upgrade of the detection system is urgently needed.

For the measurement of bunch arrival times with femtosecond resolution, environmental influences must be taken into account. Drifts of the optical and radio frequency components caused by temperature and humidity variations have a significant impact on the measurement stability. Therefore, the influence of environmental variables which might change over time on the detection system must be considered and techniques for its reduction need to be implemented and evaluated. The respective components and systems must be installed and commissioned. Procedures for the installation and characterisation of the individual components and subsystems need to be established and tested.

The transition of the accelerator control and detector electronics from the legacy VME system to the MicroTCA standard at FLASH and the use of the new system at the European XFEL from the start necessitates the adaptation of the associated components to the new environment. Prior to the studies presented in this thesis, the beam-based intra bunch-train feedback had not yet been reinstated on the MicroTCA based system. The optimal control parameters for the intra bunch-train feedback must be determined.

The bunch compression monitors for the European XFEL need to be developed, installed at the respective locations along the accelerator and commissioned. The constituents determining the detector signal – the longitudinal profile of the electron bunch, the radiation generation at the diffraction screen and its transport to the detector as well as the spectral responsivity of the measurement system – and their influencing variables must be understood.

For the design and evaluation of a feedback scheme which takes not analytically describable electron beam dynamics into account, beam transport simulations are an essential tool. In addition, they allow to study accelerator systems without needing to have access to and use valuable beam time at a real facility. The integration of a particle tracking software, implementations of the employed beam diagnostics and the handling of different timing schemes and bunch patterns in a common framework allows for the description and simulation of the complete system with one tool.

Studies at FLASH and the European XFEL are needed for commissioning the newly installed beam diagnostics and assessing the employed control schemes and feedback systems. If the particles are not yet ultrarelativistic in the farthest upstream section of the accelerator, the influence of single cavities of the first accelerating module on the time-of-flight of the bunches can lead to a change of the effective phase at the subsequent accelerating stations resulting in a systematic error between the desired and actual working point.

The operating point of the beam diagnostics and the correlation between the measured quantities and other diagnostics need to be determined. The beam-based feedback responses of the bunch arrival time and compression depending on the accelerator working point must be studied. The comparison of analytically obtained results, simulations and measurements can help assess the accuracy of the employed models and identify options for further improvement.

Scope and Contribution

The new electro-optical unit for the bunch arrival time monitors at FLASH and the European XFEL is presented. The signal flow and the physical composition of the device are explained. Individual components and subsystems – optical delay stage, fibre-optic switch and temperature control – are characterised and their suitability for the intended use is verified with measurements. The assembly and alignment procedure of the optical delay stages is described, including the required materials, tools and methods. The influence of environmental effects on the measurement stability is analysed for different parts of the unit and options for its reduction are evaluated. The temperature stabilisation is tested in a climate chamber.

The bunch compression monitor for the European XFEL is introduced. The physical composition of the detector stations and the radiation transport inside the optics box are described. The spectral intensity at the detector is simulated for all four stations. Its dependency on the electron beam energy and the diffraction screen dimensions is studied. Based on the characteristics obtained for the individual constituents of the detection system, start-to-end simulations of the BCM signal at all three compression stages of the European XFEL are presented.

In the course of this work, a beam-based feedback simulations framework has been developed. It is built around an existing particle tracking software and provides modules

for various beam diagnostics. It includes a description of the low-level radio frequency system and supports different bunch train patterns. An application programming interface for scripted access to the particle tracking code and the beam diagnostics modules is provided. For ease of use, additional graphical interfaces are available as well.

The individual framework components and their usage are documented. The program flow logic of the graphical expert windows for the beam diagnostics elements is presented. The realisation of a complete accelerating station including the low-level radio frequency and beam-based feedback loops within this framework is demonstrated. The option to automatically generate block diagrams visualising the system under investigation including plausibility tests for debugging purposes is presented.

For the commissioning of the newly installed systems and the evaluation of the beam-based feedback, machine studies at FLASH and the European XFEL are undertaken. At FLASH, the influence of single cavity phases of the first accelerating module on the time-of-flight of the bunches is analysed. The beam-based feedback responses of the bunch arrival time and compression are determined for both bunch compressors. All investigations are carried out in simulations and measurements, the arrival time feedback response matrix is additionally derived analytically in linear order.

The reinstatement of the beam-based intra bunch-train feedback with the new MicroTCA based controls and the optimisation of the feedback parameters are demonstrated. The data processing for the beam-based feedback measurements in order to identify and reject corrupted events caused by intermittent malfunctions of the employed subsystems is explained.

For the European XFEL, the signal of the first bunch compression monitor is simulated as a function of the phase set points of the first two accelerating modules. The relation between the bunch length and the compression signal downstream the third bunch compressor is investigated with simulations and measurements. The beam-based feedback responses of the bunch arrival time and compression are simulated for the first two bunch compressors. The arrival time response matrix is additionally derived analytically in linear order.

Structure of this Thesis

This thesis is structured as follows: in chapter 1, a short introduction into the applied principles of longitudinal beam dynamics and bunch compression as well as an overview over the FEL user facilities FLASH and European XFEL is given. The existing beam dynamics simulation tools used during the course of this work are presented. Chapter 2 describes the measurement principles and installation locations at FLASH and the European XFEL of longitudinal beam diagnostics suited for intra bunch-train feedback. The general concept of feedback and examples illustrating possible applications are presented.

The upgrade of the electro-optical unit for the new bunch arrival time monitors at FLASH and the European XFEL is described in chapter 3. Chapter 4 covers the

bunch compression monitors for the European XFEL. The development of a framework for beam-based feedback simulations and its usage are documented in chapter 5. In chapter 6, performance studies at FLASH are shown. Case studies for the European XFEL are presented in chapter 7. Further considerations and details of individual subsystems can be found in the Appendix.

1 Introduction

In the context of particle accelerators, the motion of charged masses can be described with the help of beam dynamics. Every particle has six basic degrees of freedom, namely its position and momentum in the three dimensions of space. Additional properties – such as the particles' mass or charge – may be taken into account if they differ among the regarded types or might change during the transport. For electron machines, the rest mass and charge of all particles are identical and invariable.

A particle's state is represented by a phase space vector defining the values of the free parameters at a given point of its trajectory. Instead of using the transverse momenta (p_x, p_y) in the description of the phase space, these values can be normalised by the longitudinal momentum p_z to obtain the corresponding trace space quantities

$$x' = \frac{\mathrm{d}x}{\mathrm{d}z} = \frac{p_x}{p_z}\,, \quad y' = \frac{\mathrm{d}y}{\mathrm{d}z} = \frac{p_y}{p_z}\,.$$

A particle's state is then given by its deviation

$$\mu \coloneqq \begin{pmatrix} \delta x \\ \delta x' \\ \delta y \\ \delta y' \\ \delta z \\ \frac{\delta p_z}{p_z} \end{pmatrix} \tag{1.1}$$

from the defined reference trajectory, with $\delta\xi = \xi_{\text{particle}} - \xi_{\text{reference}}$, $\xi \in \{x, x', y, y', z, p_z\}$. Longitudinal beam dynamics is confined to the nominal direction of motion and thus comprises two degrees of freedom, corresponding to the last two components in Equation 1.1. The longitudinal momentum deviation is given in relative units with respect to the reference value.

The motion of charged particles can be influenced with electromagnetic forces. In accelerators, electric and magnetic fields are employed in various areas of application. These include trajectory control (bending, kicking, injection, extraction), bunching and focussing. A momentum change parallel to the direction of motion – as in acceleration – can only be achieved by means of electric fields, due to the magnetic force always acting perpendicularly to the velocity vector and causing no energy transfer to the particles.

The influence of a beam transport section – such as a magnetic chicane, an accelerating module or a drift – on the particle trajectory can in first order be described by a transport

matrix. It maps the particle's state at the section output to the input conditions, based on the transport characteristics, in linear order

$$\mu_{\text{final}} = \mathbf{R}_{\text{section}} \mu_{\text{initial}} \,. \tag{1.2}$$

For a six-dimensional trace space as in Equation 1.1, $\mathbf{R}$ has 6×6 elements. The longitudinal beam dynamics is governed by the 2×2 submatrix at the bottom right.

Accelerating structures installed at large facilities are usually composed of metal cavity resonators, in which an electromagnetic field oscillates. The choice of the resonator mode and the field shape determined by the cavity geometry result in a non-zero net energy transfer to the charged particles when they traverse the structure. To a certain extent, the field shape is adjustable during operation by changing the cavity geometry, for instance with mechanical tuners. However, the typical regulation parameters with respect to beam dynamics are the amplitude and phase of the electric field by which the particles get accelerated. Those properties can be controlled on short time scales by adjusting the forward power of the radio frequency (RF) signal fed to the cavities. Therefore, they are well suited as actuators in fast feedback systems (see section 2.4).

For a given resonator mode, the electromagnetic field inside the cavities has a sinusoidal course in time. The momentum gain of a particle traversing an accelerating module in longitudinal direction is[1]

$$\Delta p_z = \frac{|q|}{c} A \cos(\phi) \,. \tag{1.3}$$

A and ϕ denote the amplitude and phase set point in volts and radians with respect to the reference phase $\phi = 0$. The reference phase is defined such that particles traversing the module experience the maximum momentum transfer.[2] $|q|$ is the absolute charge of the particle, corresponding to the elementary charge e in case of electrons.

In an accelerator, usually not single particles are used, but beams or bunches comprising many discrete charges are treated as an entity. The properties of a particle ensemble can in principle be described by regarding the state, and its evolution over time, of every individual member. However, this description is impractical for large numbers of objects. As an example, an electron bunch with a charge of $q = -100\,\text{pC}$ contains

$$N = \frac{|q|}{e} \approx 6.24 \times 10^8 = 624 \text{ million} \tag{1.4}$$

individual particles.

Oftentimes it is more practical to study collective characteristics of an ensemble: not the properties of every single particle, but collective quantities – such as the bunch

[1] Strictly speaking, this description is only valid for 'beta matched' cavities, where the particles arrive at the same RF phase in each cell. Within the scope of this work, this condition is fulfilled if not stated otherwise (see e.g. section 6.1).

[2] This usually means maximum momentum gain, with the exception of ACC39 at FLASH, where it means maximum momentum loss (see section 6.2.1).

centroid and size – are of interest. Depending on the number of parameters under investigation, the complexity of the system can be significantly reduced in this way. Such an approach is for example advantageous in conjunction with analytical derivations or computer simulations.

1.1 Bunch Compression

At free-electron laser (FEL) facilities, electrons are used for generating ultrashort photon pulses with high brilliance. For this purpose, an accelerator provides electron bunches with suitable properties – such as beam energy and charge density – which are subsequently guided through periodic magnetic structures, called undulators. By following an oscillatory trajectory controlled by the shape of the magnetic field, the electrons generate self-amplified spontaneous emission (SASE) radiation, which is then transported to the photon experiments [SNF+07].

The electron beam properties in the undulator section affect the characteristics of the SASE process. Important parameters in this context are the beam energy, the current profile (longitudinal charge distribution over the bunch) and the degree of correlation of the particles' trajectories (described by the emittance). For the SASE process, a high peak current and a low emittance are needed [SNF+07, p. 14]. The beam energy, in combination with the undulator field geometry, defines the wavelength of the FEL radiation [SNF+07, p. 20].

The generation of short electron bunches with a high peak current is hindered by space charge effects [SNF+07, p. 15]. After exiting the gun and before getting accelerated, the particles' momenta are small compared to the value needed in the undulator section. As they all have charges of the same sign (negative in the case of electrons), the particles repel each other due to space charge forces. This situation leads to a blow-up of the bunch size and an emittance degradation.

The space charge forces scale with $1/\gamma^2$, with γ denoting the Lorentz factor [CMTZ13, p. 137]. For this reason, the electron bunches are not created short. Instead, a cascaded approach is used: the bunches exiting the gun contain the required number of electrons, but distributed over a longer length. Thus, the space charge density is lower and the repelling forces are smaller. Subsequently, the bunches are accelerated and compressed longitudinally in several steps, until the required beam energy and charge density is reached. For this purpose, acceleration sections and magnetic chicanes are installed in an alternating order, a scheme which can be recognised in the layouts of FLASH and the European XFEL shown in Figure 1.3 and Figure 1.5. In this way, a high peak current in the undulator section can be achieved while keeping the emittance small.

In order to implement the longitudinal bunch compression a beamline section with a variable time-of-flight is needed: the bunch head must be delayed with respect to the bunch tail. Due to the velocity of the particles being very close to the speed of light ($v \approx c$), this can only be achieved by varying the path length with the help of a magnetic

chicane: by employing longitudinal dispersion, the particles' transit time through the structure is made dependent on their momentum.

In order for this scheme to work, a correlation between the particles' longitudinal position δz in the bunch and their momentum deviation $\frac{\delta p_z}{p_z}$ is needed. This can be realised by choosing appropriate operating points of the accelerating stations upstream the magnetic chicane. As the field inside the cavities has a sinusoidal course in time (see Equation 1.3), both the amplitude and the phase at which the particles traverse the accelerating module control the momentum gain and its slope over the bunch.

Particles in the head of the bunch (having a larger δz) arrive at earlier times at a fixed position of the beamline. By operating the accelerating station at a phase set point on the rising edge of the cosine, the leading particles experience less momentum gain than the trailing ones. This off-crest acceleration scheme results in a correlation between the longitudinal position in the bunch and the momentum deviation of the particles, referred to as energy chirp. The absolute momentum gain can be adjusted with the amplitude set point.

A possible realisation [Cas03] of a bunch compression chicane is shown in Figure 1.1. It comprises four identical dipole magnets arranged in a symmetrical way. The first dipole deflects the particles from their straight path by an angle depending on the beam energy: given that all particles have the same charge and rest mass, the ones with a higher momentum experience less trajectory bending than the ones with a lower momentum.

The second dipole has the same effective field length and strength as the first one, but with an inverted polarity. It deflects the particles by the same amount, but in the opposite direction, thus restoring the original propagation direction. The beam is now split up transversely according to the particle momenta. The final two dipoles bring back the beam to the original trajectory and cancel the transverse path separation.

Due to the different deflection angles, particles with a higher momentum travel a shorter distance and thus traverse the chicane faster than ones with a lower momentum. In Equation 1.2, the longitudinal dispersion in first order is described by the term

$$\delta z_{\text{final}} = \delta z_{\text{initial}} + R_{56} \frac{\delta p_z}{p_z} \,. \tag{1.5}$$

The coefficient R_{56} depends on the geometric properties of the bunch compressor, such as the effective magnetic field lengths and strengths as well as the distances between the dipoles [Cas03].

For ultrarelativistic particles travelling very close to the speed of light, the arrival time change downstream the chicane with respect to the reference trajectory is

$$\delta t_{\text{A}} \approx -\frac{\delta z_{\text{final}} - \delta z_{\text{initial}}}{c} = -\frac{R_{56}}{c} \frac{\delta p_z}{p_z} \,. \tag{1.6}$$

The minus sign originates from the choice of coordinate systems: particles in the head of the bunch (having a larger δz) arrive at earlier times at a fixed position of the beamline

$$\frac{\mathrm{d}t}{\mathrm{d}(\delta z)} = -\frac{1}{c} \,. \tag{1.7}$$

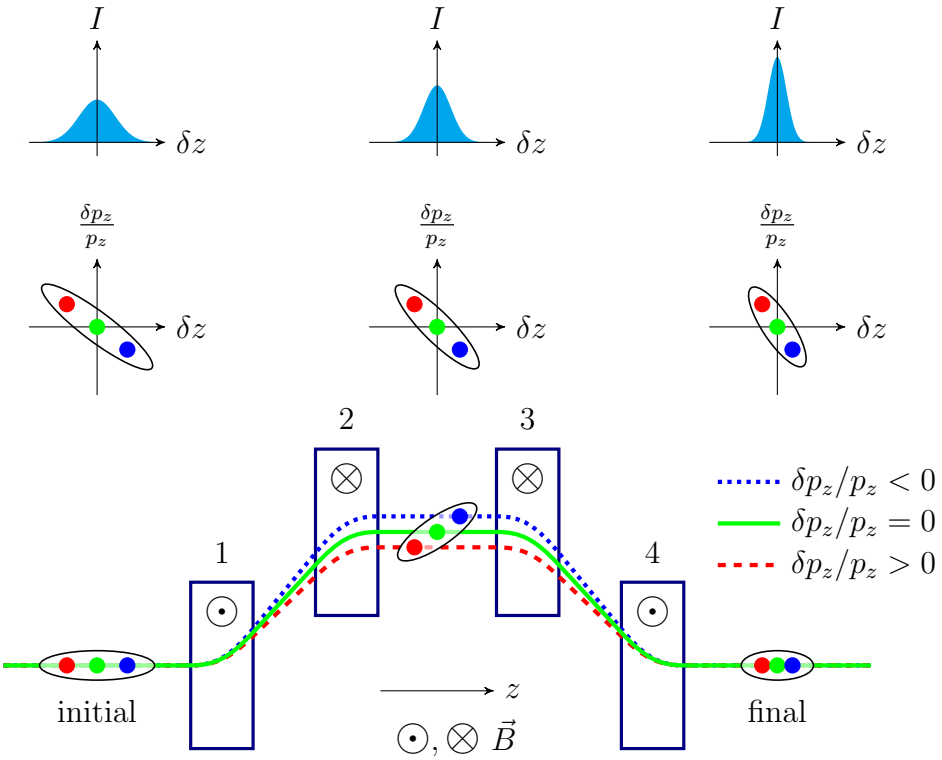

Figure 1.1: Schematic layout and operating principle of a C-type magnetic chicane of a bunch compressor. From bottom to top: geometric layout, longitudinal phase space and current profile of the bunch at different positions along the section. The electrons travel from the left to the right. The colours represent the particle momentum: nominal (green), lower (blue) and higher (red). Adapted from [Boc12, p. 170], [Löh09, p. 14] and [Wes12, p. 10].

As particles with a higher momentum have a shorter travelling time through the chicane than lower momentum ones, R_{56} is positive. When the leading particles in the bunch have less momentum than the trailing ones, the bunch is shortened after traversing the section.[3]

Phase Space Linearisation

The correlation between the particles' longitudinal position in the bunch and their relative momentum deviation induced by the off-crest acceleration scheme is non-linear: the sinusoidal course in time of the field in the cavities is imprinted on the longitudinal

[3]This model is of course only valid until the initially trailing particles get ahead of the initially leading ones. At this point, over-compression is achieved and the bunch becomes longer again.

momentum profile of the bunch. By linear compression in the magnetic chicanes, a current spike is produced in which only a small fraction of the particles is included.

In order to let more particles contribute to the current spike, the phase space can be linearised. A possible method for realising such a linearisation is the installation of an additional accelerating module – which operates at a higher harmonic of the frequency used by the existing modules – upstream the magnetic chicane of the bunch compressor [FLP01]. The amplitude and phase set points of the fundamental and higher harmonics modules can then be adjusted such that the sum momentum gain the particles experience when traversing the combination is linearised over the bunch. The underlying principle of this method is the Fourier transform: a linear slope is approximated by the sum of two sine curves with different frequencies.

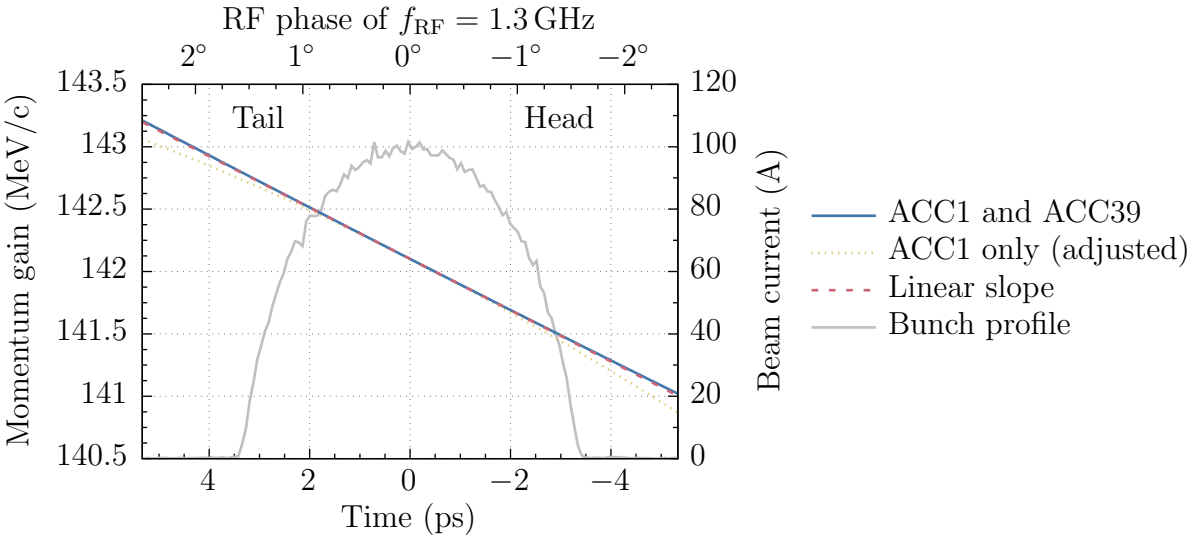

Figure 1.2: Linearisation of the sum momentum gain over the bunch with a higher harmonics module at FLASH. For the 'ACC1 only' case, the operating point of the module is chosen such that it matches the value and slope of the combined case at zero-time. The current profile for a bunch charge of 500 pC is computed from [Zag13, ACC1]. In order to correspond to a beam travel direction from left to right, the time axis is reversed (q.v. Equation 1.7).

Figure 1.2 illustrates the phase space linearisation effect. The deviation from an ideal linear correlation (dashed curve) between the particles' longitudinal position and their momentum gain is almost completely removed. For this reason, both FLASH and the European XFEL are equipped with phase space linearising higher harmonic modules (see subsequent sections).

1.2 Free-Electron Laser FLASH

The Free-Electron Laser in Hamburg (FLASH) [Deu17b] is a soft X-ray, high repetition rate free-electron laser (FEL) user facility located at the Deutsches Elektronen-Synchrotron in Hamburg, Germany. Its key parameters are listed in Table 1.1. The wide range of bunch charges the machine can be operated with needs to be considered in connection with beam diagnostics (see chapter 2).

Parameter	Unit	FLASH1	FLASH2
Electron beam at the undulator entrance			
Bunch charge	nC	$0.02 \ldots 1$	
Energy	GeV	$0.35 \ldots 1.25$	$0.4 \ldots 1.25$
Peak current	kA	$1 \ldots 2.5$	
RF pulse length (flat top)	µs	≤ 800	
Bunch repetition rate within macropulse	MHz	≤ 1	
Bunches per macropulse[a]		≤ 600	
Macropulse repetition rate	Hz	≤ 10	
FEL radiation (first harmonic)			
Wavelength	nm	$4.2 \ldots 51$	$4 \ldots 90$
Single pulse energy	µJ	$1 \ldots 500$	$1 \ldots 1000$
Pulse duration (FWHM)	fs	$< 30 \ldots 200$	$< 10 \ldots 200$

[a] limited by the flat top length of the gun RF pulse.

Table 1.1: Key parameters of FLASH. Adapted from [Deu17a].

The schematic layout of the facility is shown in Figure 1.3. A pulsed injector laser extracts electron bunches from a photo cathode mounted inside a normal conducting RF cavity, which accelerates them to approximately 5 MeV [SNF+07, p. 15]. The longitudinal momentum of the particles is then increased with the help of the first accelerating module. In the subsequent higher harmonic module – operated at a frequency of $3f_{\mathrm{RF}} = 3.9\,\mathrm{GHz}$ in contrast to the $f_{\mathrm{RF}} = 1.3\,\mathrm{GHz}$ used at all other stations – the longitudinal phase space of the electrons is linearised (see section 1.1). All accelerating cavities except for the electron gun are superconducting.

Downstream the first accelerating section, a C-type magnetic chicane completes the first of two bunch compression stages. The subsequent second stage comprises another accelerating section for further boosting the particle momentum and an S-type magnetic chicane for the compression of the longitudinal bunch profile. A final accelerating section is used for tuning the beam energy at the undulators. Downstream the final accelerating section a collimator is installed for filtering out particles with the wrong energy or large transverse offsets and angles. This is done in order to avoid beam losses in the undulators which would degrade the magnetic field [SLP+08].

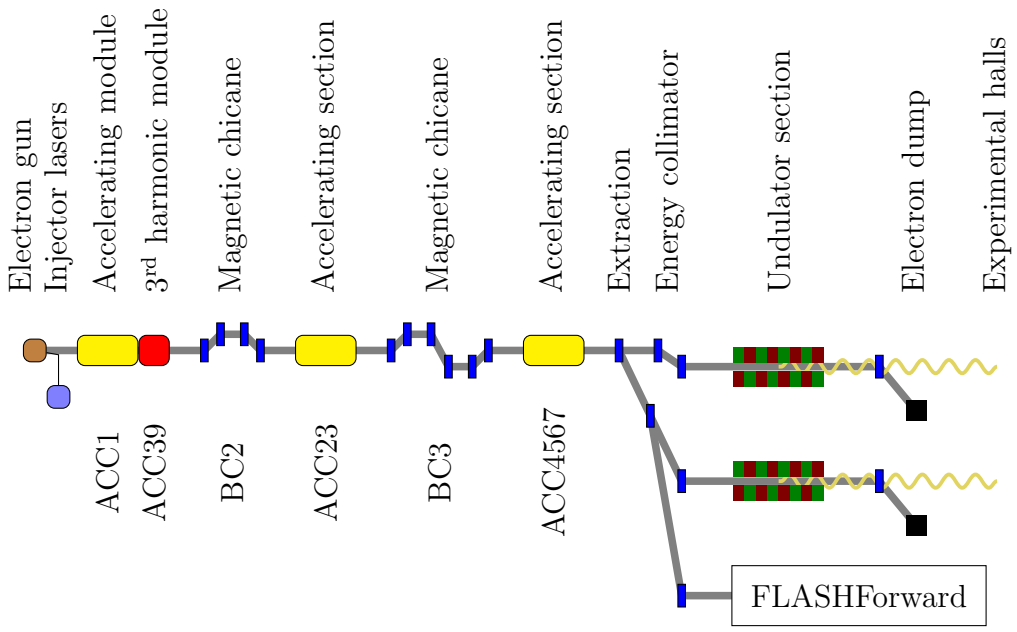

Figure 1.3: Schematic layout and section names of FLASH (not to scale).

Subsequently the beamline divides into two branches named 'FLASH1' and 'FLASH2'. Each branch has its own undulator section and experimental hall, enabling the simultaneous operation of two user experiments. The distribution of electron bunches to the different trajectories is carried out by a series of fast kicker magnets in combination with a magnetic septum [SDF+12][OK15]. An additional beamline for the research and development of beam-driven plasma-wakefield acceleration [ABB+16] is installed alongside the FLASH2 undulator section.

In the undulators, the magnetic field configuration forces the electron bunches on an oscillatory trajectory which results in the emission of SASE radiation. The photons are guided to the user stations located in the respective experimental hall. After exiting the undulators, the electrons are deflected into a beam dump.

The bunch pattern used at FLASH is shown in Figure 1.4. The macropulse repetition rate is usually 10 Hz. Every macropulse consists of bursts of bunches destined for the three beamlines. The bunches within the train have a repetition frequency of $f_B = 1\,\mathrm{MHz}/n$ with $n \in \mathbb{N}$.

The sub-trains destined for the individual beamlines can have different bunch spacing, number of bunches and bunch charge. In order to allow for small adjustments of the beam parameters in the branches, the RF set points of the accelerating modules can differ for the sub-trains within certain limits [AAB+15]. For trajectory switching and RF settings adjustment, the bunches delivered to different beamlines are separated by a gap of 40 µs.

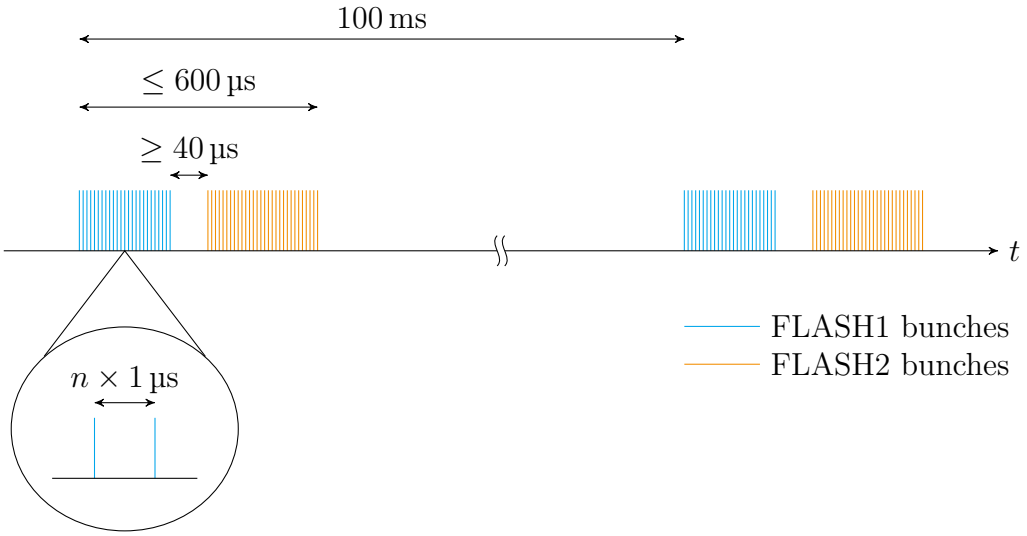

Figure 1.4: Bunch pattern at FLASH. Adapted from [SNF+07, p. 29].

The maximum length of the entire bunch train (burst duration) is usually limited to a value between 500 µs and 600 µs by the flat top length of the gun RF pulse in order to protect the RF window from damage. When serving only FLASH1 or FLASH2, up to 6000 bunches per second can be generated in this way. If both beamlines are operated, this number is reduced to 5600 due to the gap needed between the sub-trains.

1.3 European XFEL

The European X-Ray Free-Electron Laser (European XFEL) is an FEL user facility providing ultrashort, high brilliant X-ray pulses with a high repetition rate. It extends from the Deutsches Elektronen-Synchrotron in Hamburg, Germany, to the nearby city Schenefeld. Its key parameters are listed in Table 1.2. The range of bunch charges the machine can be operated with spans the same wide interval as at FLASH.

The schematic layout of the facility is shown in Figure 1.5. Like at FLASH, the electron bunches are generated by a pulsed injector laser illuminating a photo cathode mounted inside a normal conducting RF cavity. Downstream the gun, an accelerating module is installed for increasing the particles' longitudinal momentum. In the subsequent higher harmonic module – operated at a frequency of $3f_{\mathrm{RF}} = 3.9\,\mathrm{GHz}$ in contrast to the $f_{\mathrm{RF}} = 1.3\,\mathrm{GHz}$ used at all other stations – the longitudinal phase space of the electrons is linearised (see section 1.1). All accelerating cavities except for the electron gun are superconducting.

Downstream the first accelerating section, a laser heater [HZ13] is installed. In this small C-type magnetic chicane a laser beam interacts with the electron bunches in a short undulator, thereby increasing the longitudinal momentum spread of the particles to

Parameter	Unit	SASE1/2	SASE3
Electron beam at the undulator entrance			
Bunch charge	nC	0.02 . . . 1	
Energy	GeV	10.5 . . . 17.5	
Peak current	kA	4.5 . . . 5	
RF pulse length (flat top)	µs	$\leq$ 600	
Bunch repetition rate within macropulse	MHz	$\leq$ 4.5	
Bunches per macropulse		$\leq$ 2700	
Macropulse repetition rate	Hz	$\leq$ 10	
FEL radiation (first harmonic)			
Wavelength	nm	0.05 . . . 0.45	0.15 . . . 5
Single pulse energy	mJ	0.03 . . . 3.7	0.1 . . . 12
Pulse duration (FWHM)	fs	1.7 . . . 107	

Table 1.2: Key parameters of the European XFEL. Adapted from [DL13] and [SY11].

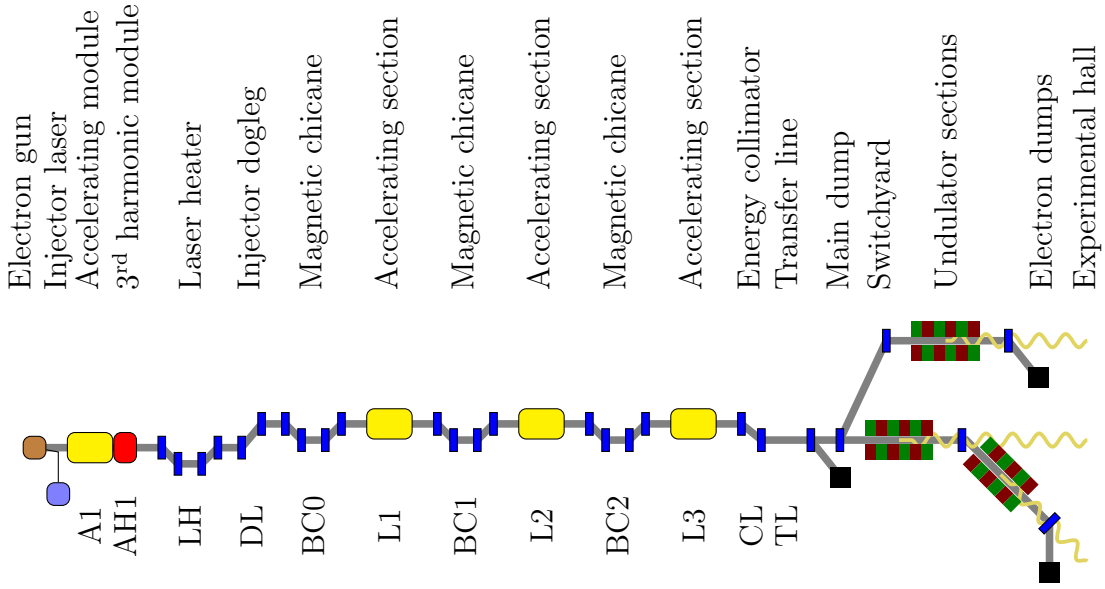

Figure 1.5: Schematic layout and section names of the European XFEL (not to scale).

prevent micro-bunching instabilities. Downstream the laser heater, the electron beamline is transferred from the injector building to the main linac tunnel via a dogleg chicane.

A subsequent C-type magnetic chicane completes the first of three bunch compression stages. The second and third stage each comprise another accelerating section for further increasing the particle momentum and a C-type magnetic chicane for the compression of the longitudinal bunch profile. The final accelerating section is used for boosting the beam energy to the value needed at the undulators.

Like at FLASH, a collimator is installed downstream the final accelerating section for filtering out particles with the wrong energy or large transverse offsets and angles. This is done in order to avoid beam losses in the undulators which would degrade the magnetic field. In the subsequent switchyard, the bunches are distributed to the undulator sections serving the different user stations located in the experimental hall. Downstream the undulator sections, the electrons are deflected into beam dumps. Additional beam dumps are installed at several locations along the accelerator, allowing for stepwise machine set-up and emergency beam stop.

The bunch pattern used at the European XFEL is similar to the one at FLASH. The macropulse repetition rate is 10 Hz, with every macropulse consisting of bursts of bunches destined for the different undulator sections. The bunches within the train have a repetition frequency of $f_\mathrm{B} = 9\,\mathrm{MHz}/n$ with $n \in \mathbb{N}, n \geq 2$, hence $f_\mathrm{B} \leq 4.5\,\mathrm{MHz}$. With a maximum RF pulse length of 600 µs, up to 27 000 bunches can be generated per second.

1.4 Beam Dynamics Simulations

For a given accelerator lattice, a variation of machine parameters at some point of the facility leads to changes in the beam dynamics downstream the manipulated element. The possible input variables can be of various kinds, such as cavity gradients and phases, magnet strengths or timing changes. Likewise, the influenced quantities arise from diverse areas, concerning for instance the single particle trajectories or collective properties of the bunch such as peak current, compression and emittance.

It is of interest to study the influence of changed input settings on beam dynamics without needing to have access to and use valuable beam time at a real facility. In this case, computer simulations can be carried out to emulate the effect of varying the machine operating point. Furthermore, these tools are used during the process of designing and commissioning an accelerator. In this context, they also play an important role in defining and tuning the operating point of the facility.

Depending on the particular question, various tools can be used to analyse different aspects and individual subsystems. The simulations done in the course of this work have been carried out using the frameworks `RF Tweak` for fast two-dimensional, longitudinal, ultrarelativistic tracking and ASTRA for full six-dimensional computations in the non-ultrarelativistic regime.

1.4.1 RF Tweak

`RF Tweak 5` [BDD15] is a longitudinal particle tracking software designed to assist in machine operation, written in Matlab. For a given accelerator lattice, input particle distribution and settings of the accelerating modules, it computes the particle distributions at different locations of the machine. Due to its restriction to the longitudinal phase space of ultrarelativistic beams and the non-consideration of space charge forces, the tracking is relatively fast. A single pass through FLASH with one million particles is completed in about two seconds on a standard office PC, compared to several hours needed for full six-dimensional, space-charge considering tracking codes such as ASTRA (see next section).

The input particle distribution files are stored in the ASTRA format. This facilitates the cascaded use of different tools for individual parts of the accelerator, such as ASTRA for the low-energy section and `RF Tweak 5` for the ultrarelativistic domain. Several precomputed input particle distributions are available for different bunch charges between 20 pC and 1 nC, further can be created with ASTRA if needed. The lattices of FLASH and the European XFEL are supported.

The current development branch is `RF Tweak 5 GUI`, which supplements the core `RF Tweak 5` tracking code with a graphical user interface (GUI). This extension allows for an easy and intuitive handling of the RF settings as well as the immediate display and visual analysis of the tracking results. Via the GUI, the input particle distribution, the amplitude and phase set points of the accelerating modules as well as the properties of dispersive sections (magnetic chicanes) can be adjusted. The electron bunch is tracked through the machine and the particle distribution is visualised at various locations of the lattice (downstream every lattice element). In addition, the current profile over the bunch at the different stations is calculated and plotted.

During the course of this work, an application programming interface (API) enabling scripted access to the tracking inputs and results has been developed and integrated into the `RF Tweak 5 GUI` code (see section 5.1). In addition, beam diagnostics elements transforming the particle distribution to detector readouts (see section 5.1.1) have been developed. For these detectors, additional diagnostics windows have been integrated into the GUI (see section 5.5).

The RF gun set point can not be varied in `RF Tweak`, because it would significantly change the particle distribution in the bunch as well as the beam dynamics in the section between the gun and the first accelerating module where the beam is not yet ultrarelativistic. In this case, the fast 2D tracking without the consideration of space charge forces is not applicable. If the RF gun parameters are to be varied, full 6D ASTRA simulations are necessary.

1.4.2 ASTRA

`A Space Charge Tracking Algorithm` (ASTRA) [Flö17] is a software framework for computing the movement of charged particles in electromagnetic fields, written in Fortran 90. It takes space charge forces and the full six-dimensional phase space into account. Therefore, ASTRA is especially suited for investigating the beam dynamics in the low-energy regime where the particles are not yet ultrarelativistic and space charge forces arise.

The description of the accelerator lattice, input particle distributions and electromagnetic field geometries are declared in text files. The data files defining the particle distributions can also be used by `RF Tweak`. Due to the more complex tracking scheme, the simulations are more time-consuming – though more versatile – than `RF Tweak` runs with comparable settings. In the scope of this work, ASTRA is used for the investigation of time-of-flight effects in the low beam-energy domain up to the exit of the first accelerating module at FLASH (see section 6.1).

2 Longitudinal Diagnostics for Intra Bunch-Train Feedback

Longitudinal bunch properties – such as the arrival time, compression or energy – define, among others, the working point of a particle accelerator and subsequently the characteristics as well as the quality of the radiation delivered to the user experiments. Monitoring and controlling those quantities – as well as their temporal and spatial behaviour along the machine – therefore plays an important role in setting up, tuning and operating an accelerator.

In addition, longitudinal beam diagnostics provide valuable information for the user experiments themselves. By correlating electron arrival time measurements with laser pulse timing information in a pump-probe experiment, for a measurement series with multiple events the data can be sorted by time and the temporal development of a physical, chemical or biological process can be reconstructed [SBB+17].

A further task of longitudinal beam diagnostics is the verification of stability requirements defined for the accelerator. In order to ensure a steady and reliable operation of the facility, precise monitoring of these properties is needed. This application also concerns the necessary resolution of the monitors. They must be able to measure quantities smaller than the changes typically caused by the controlling systems' operating steps, in order to quantify the residual regulation errors.

This chapter focuses on those longitudinal beam diagnostics elements which are suitable for fast intra bunch-train feedback. An introduction to feedback concepts is given in section 2.4. The devices and techniques described here have also been implemented as diagnostics elements in the longitudinal beam dynamics code `RF Tweak` presented in section 1.4.1.

2.1 Bunch Arrival Time Monitor

The bunch arrival time is defined as the moment in time at which the centroid of the electron bunch passes a given longitudinal position of the accelerator. It affects both the machine operation as well as the performance of the user experiments:

- By determining the phase $\phi_{\mathrm{ACC}} = 2\pi f_{\mathrm{RF}} t + \phi_0$ at which the beam gets accelerated in the RF cavities, the energy gain and compression of the bunches are influenced.

- Jitter of the electron timing in the undulators results in a changed photon creation time.

- For seeding and pump-probe experiments, the correct timing between the electron bunches (or photon pulses) and an external laser system needs to be ensured.

In conjunction with a dispersive beamline section, arrival time measurements can be used for determining the beam energy (see Equation 1.6 on page 10).

Typically, the electron bunch length in the undulators is in the order of 50 fs to 100 fs. On the other hand, a RF phase stability of $\delta\phi = 0.01°$ at $f_{\mathrm{RF}} = 1.3\,\mathrm{GHz}$ corresponds to a required timing stability of $\frac{\delta\phi}{360°} f_{\mathrm{RF}}^{-1} \approx 21.4\,\mathrm{fs}$. In order to provide the necessary measurement precision for the aforementioned applications, a resolution in the femtosecond range is thus needed.

The arrival time measurement is carried out with respect to a common reference clock used by all subsystems of the accelerator (i.a. photo injector laser and RF modules), which provides a defined time base for the machine operation. Due to this scheme, drifts of the common reference clock do not influence the machine operating point as all connected systems are affected in the same, correlated way. Only uncorrelated timing changes of the individual subsystems have an impact on the accelerating conditions.

2.1.1 Laser-Based Synchronisation System

A necessary prerequisite for a detector system with femtosecond resolution is a reference clock with a stability better than the desired measurement precision. At FLASH and the European XFEL, this reference is provided by a laser-based synchronisation system [SGB+15] as outlined in Figure 2.1. It makes use of ultra-short laser pulses from a Master Laser Oscillator (MLO) which are distributed to multiple optical fibres (referred to as *optical links*) connecting the different end stations to the system. The links are individually actively length-stabilised in order to compensate for environmental changes, like temperature- or humidity-induced drifts along the fibre. Due to the common origin of the laser pulses, all link end stations – such as bunch arrival time monitors (BAMs) or the laser systems for seeding and pump-probe experiments – are synchronised within the level of the link jitter, which is in the order of a few femtoseconds.

The active link stabilisation is implemented by reflecting part of the laser light at the link end back upstream the optical fibre to the synchronisation system, where it is correlated with fresh laser pulses from the MLO. The timing difference between the new and reflected laser pulses is then used as an input for a feedback system which dynamically adjusts the fibre length with a piezo stretcher. In this way, the timing of the laser pulses at the link end can be stabilised down to the femtosecond level, providing a reference clock for the connected end station. This scheme is carried out for each link individually, as the fibres experience different environmental changes due to their respective routing.

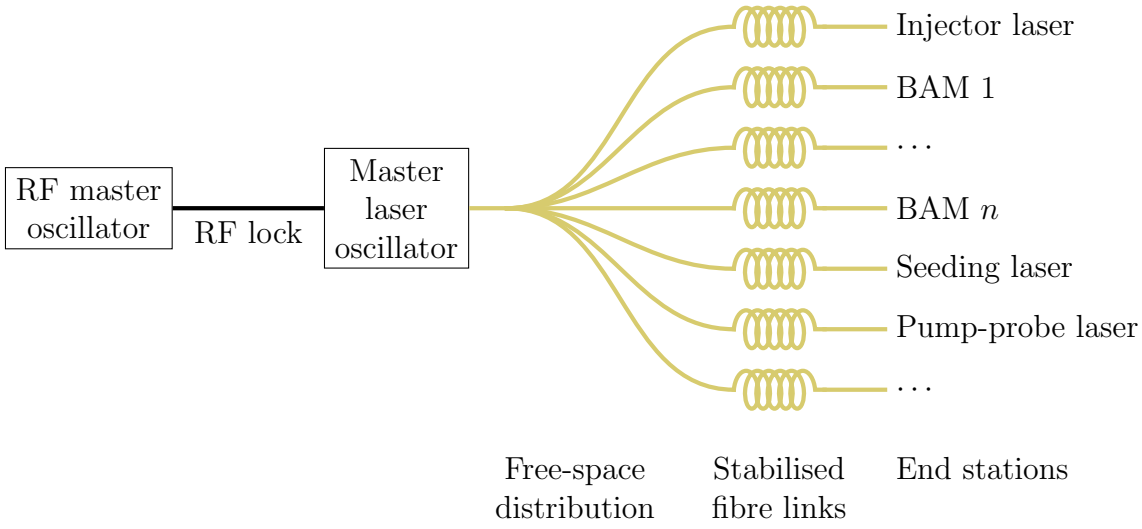

Figure 2.1: Schematic layout of the laser-based synchronisation system.

The MLO itself is locked to the RF Master Oscillator (MO) which provides the timing reference for further accelerator subsystems. In order to minimise drifts on the connection between the MO and the MLO, both systems are installed inside climate-stabilised rooms in immediate vicinity. The free-space laser distribution as well as the electronics and optics for the link stabilisation also are located inside climate-stabilised compartments.

2.1.2 Measurement Principle

The bunch arrival time detection scheme is based on electro-optical modulation, as illustrated in Figure 2.2. Pick-ups mounted in the beam pipe capture the electric field of the passing bunches. By combining the signals of two opposing pick-ups, the beam orbit dependence of the measurement is reduced [Löh09][Boc12]. The sum RF pulse is applied to an electro-optical modulator (EOM), which changes the amplitude of passing laser pulses depending on the voltage.

By feeding the pulses from the laser-based synchronisation system to the EOM, a reference clock is established. Under the assumption that the individual components are not subject to drifts, the modulation voltage at the time of the laser pulse passage only depends on the relative timing between the electric signal from the pick-ups (i.e. the bunch arrival time) and the reference clock. As a result, the laser pulses sample the pick-up signal at a defined time.

The amplitude of the modulated pulses exiting the EOM is a measure for the applied voltage at the reference time. It is subsequently sampled using a fast photodiode and further processed in the detector electronics: by dividing the modulated amplitude by the signal of the unmodulated pulses (zero voltage, sampled before the bunch arrives

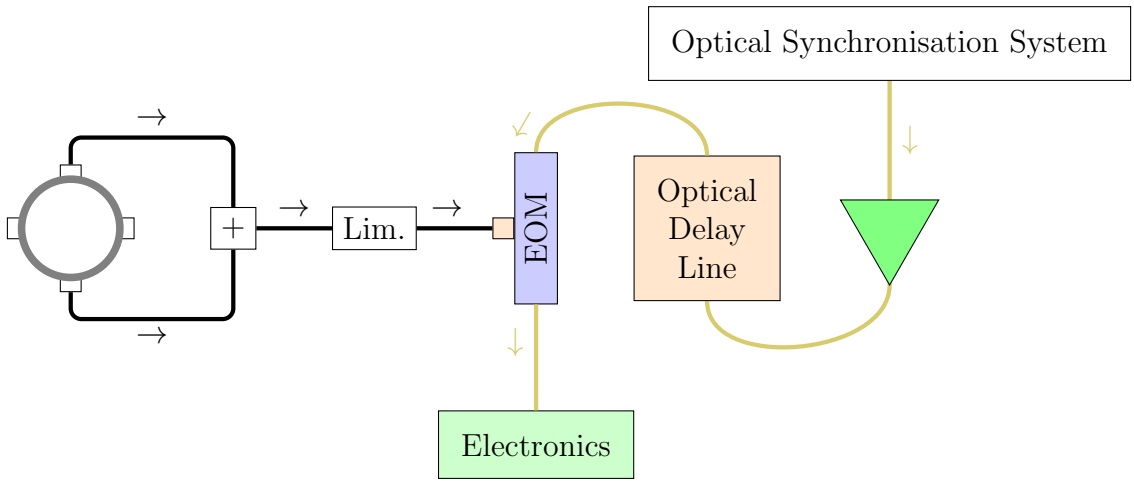

Figure 2.2: Basic layout of the BAM cabling scheme (only one detection channel is shown). The arrows indicate the signal flow. Adapted from [DCG+15, p. 478].

at the pick-ups), the relative modulation is obtained. This value is – in contrast to the absolute number – robust against long-term drifts of the laser pulse amplitude from the optical synchronisation system.

The operating point of the system is chosen in such a way that the electric pulse is sampled at the first zero crossing for bunches arriving at the pick-ups at the defined zero time. In this case, the relative modulation is unity. For bunches being early or late with respect to the reference clock, the modulation signal changes with the amount of change being a measure for the timing difference. Using the first zero crossing of the electric field has the advantage that the detection is carried out at the position of the steepest slope of the modulation signal, yielding a maximum measurement resolution.

Further components are included in the system for signal preparation and adjustment: The amplitude of the incoming laser pulses from the synchronisation system is increased by an amplifier in the optical fibre upstream the EOM in order to make use of the full measurement range of the sampling photodiode. An optical delay line between the laser-based synchronisation system and the EOM allows for changing the zero time by delaying the reference pulses with respect to the pick-up signal. It can also be used for calibrating the modulation slope as a function of the arrival time by scanning the time delay and recording the modulation change.

In order to protect the EOM from high voltage damage, a limiter is included in the RF signal path downstream the combiner. Alternatively, an attenuator can be used to implement a coarse channel with a lower resolution and a wider dynamic range. By installing a BAM body with four pick-ups in the beam pipe, as indicated in Figure 2.2, a system with two channels of different sensitivities can be realised [Boc12, p. 75].

2.1.3 Installation Locations

At FLASH and the European XFEL, bunch arrival time monitors are installed at several locations along the facilities, as indicated by the green dots in Figure 2.3 and Figure 2.5. For both machines, the first BAM is located downstream the third harmonic accelerating module (upstream the magnetic chicane of the first bunch compressor). Figure 2.4 shows a photograph of the bunch arrival time monitor installed at the European XFEL injector.

FLASH presently features two more BAMs, located in the diagnostics sections downstream the bunch compressors. Additional systems are currently being prepared to be put into operation, marked with white dots in Figure 2.3. The BAM downstream the last accelerating module will provide out-of-loop timing information for the beam-based feedback in the second bunch compressor and will be the first one at FLASH equipped with the new electro-optical unit described in chapter 3. Further monitors will allow for arrival time measurements in each of the separate beamlines, with an additional device installed downstream the FLASH2 undulator section for out-of-loop and correlation studies.

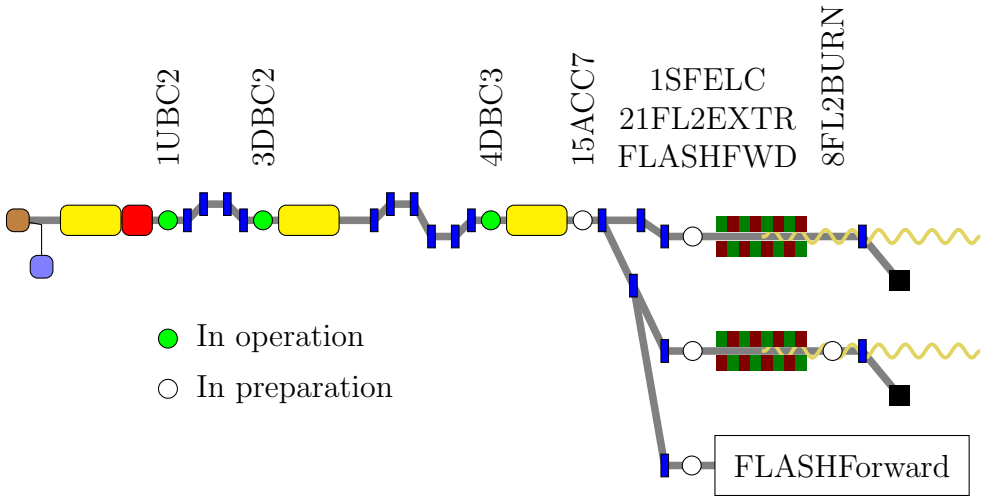

Figure 2.3: Locations and names of the bunch arrival time monitors at FLASH. Adapted from [VCD+17b, p. 697].

At the European XFEL, bunch arrival time monitors along the main linac are located in the diagnostics sections up- and downstream of each of the last two bunch compression chicanes. Two BAMs installed in series downstream the final collimation section will allow for out-of-loop and correlation measurements. The optical reference for the first one is provided by the master laser oscillator located close to the injector, while the second one is supplied by the slave laser oscillator located in the experimental hall [SCF+13]. As an option for a future upgrade, three additional BAM systems can be set up downstream the SASE undulators. All devices installed at the European XFEL are equipped with the new electro-optical unit described in chapter 3.

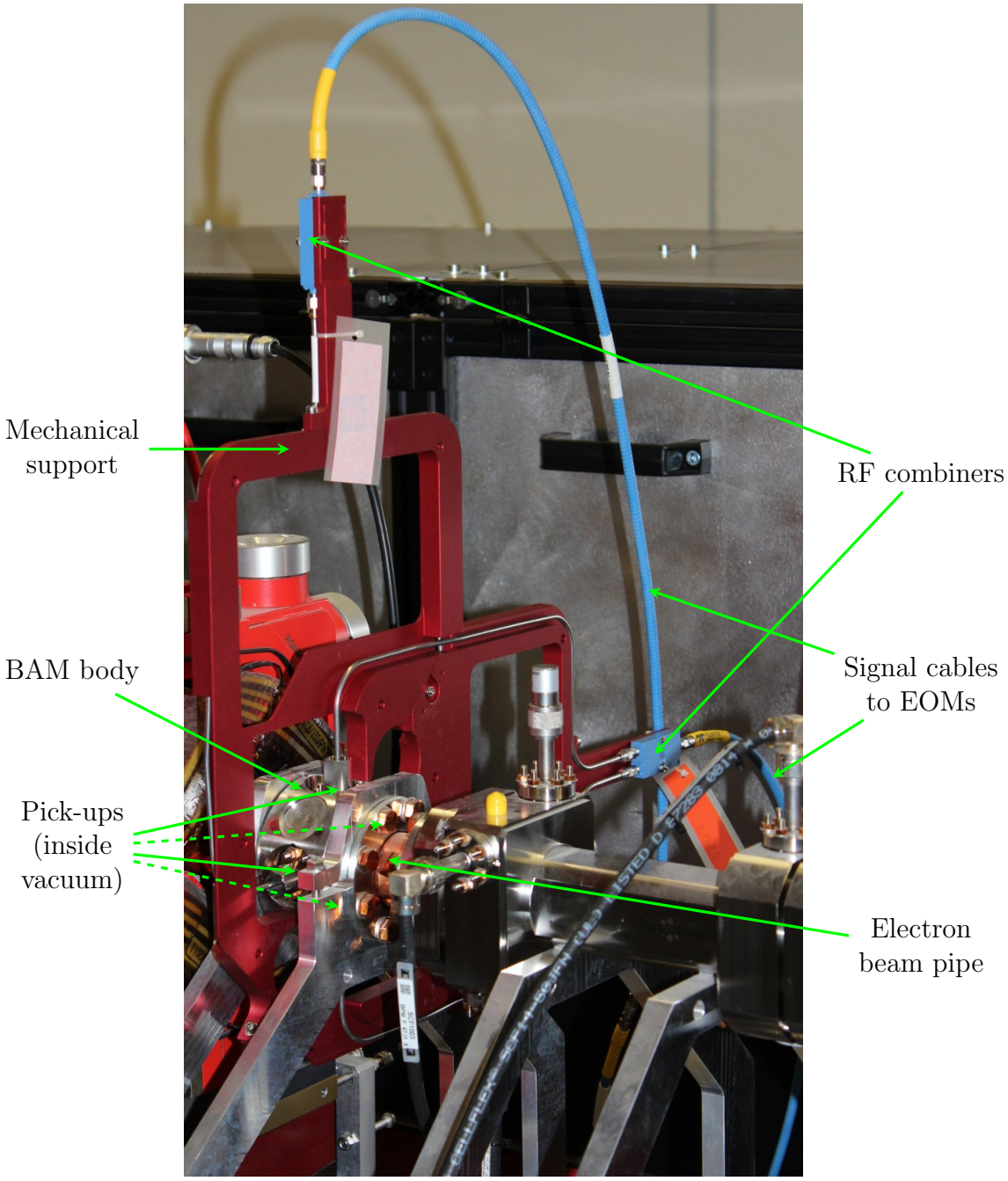

Figure 2.4: Photograph of the RF unit of the bunch arrival time monitor installed in the injector beamline at the European XFEL. The pick-ups indicated by dashed lines are hidden by other parts.

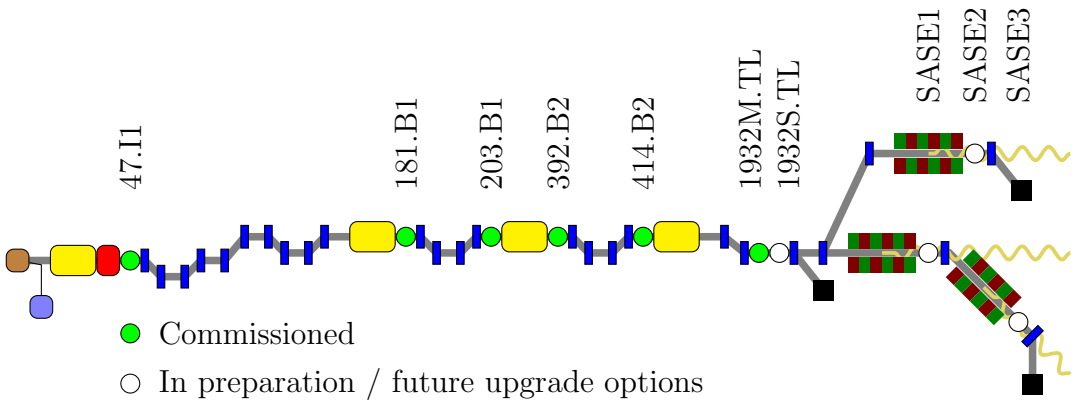

Figure 2.5: Locations and names of the bunch arrival time monitors at the European XFEL. Adapted from [VCD+17b, p. 697].

2.1.4 Integration into RF Tweak

A module for bunch arrival time measurements has been implemented in the longitudinal beam dynamics code `RF Tweak 5 GUI` [BDD15] during the course of this work. The measurement signal is determined by calculating the longitudinal shift of the bunch centroid with respect to the reference position. By instantiating the respective class at user-specified locations along the accelerator lattice, arrival time measurements can be performed at arbitrary positions of the machine. For the purpose of flexibility and versatility, the list of bunch arrival time monitor stations is not hard-coded for a particular accelerator, but can be freely adapted to any given machine lattice.

2.2 Bunch Compression Monitor

As described in section 1.1, operating an accelerator at a properly chosen compression scheme plays an important role in preparing the beam for the SASE process. Bunch compression monitors (BCMs) installed at critical lattice locations – where the defined compression values are to be maintained – allow for monitoring and controlling their evolution along the machine. By representing the defined accelerator operating point, BCM signals inherently qualify as monitors for a feedback system stabilising the machine conditions.

The term ‘bunch compression’ refers to the spatial distribution of the particles inside the bunch. Therefore, BCMs are typically installed between the magnetic chicane of a bunch compressor (where the longitudinal positions of the particles with respect to each other can change) and the next accelerating module (which alters the momentum of the particles, but not the spatial distribution due to the particle velocity being very close to the speed of light, $v \approx c$).

Depending on the operation mode of the facility, the detectors must be able to cover a wide measurement range: the scope of possible bunch charges typically extends from below 100 pC up to 1 nC at FLASH and the European XFEL, with the detector signal being proportional to the square of the charge (see Equation 2.1). Moreover, the electron bunches can be uncompressed, slightly or highly compressed. In order to obtain the necessary peak current for SASE operation, the bunches get compressed in several steps down to a final length of typically 50 fs to 100 fs at the end of the accelerator (see section 1.1 and Table 4.1 on page 68). For covering the diversity of possible measurement values, it can be necessary to use detectors of different types or sensitivities at the various monitor locations. Additionally, installing multiple detectors with different sensitivities at specific stations can help to support a wider signal range.

2.2.1 Measurement Principle

The bunch compression monitors employed at FLASH and the European XFEL make use of coherent diffraction radiation (CDR) emitted by the electron bunch passing through a diffraction screen placed in the beam path. Figure 2.6 shows the basic scheme of a BCM station. The diffraction screen is a metallic aperture installed in the beam pipe at an angle of 45° with respect to the beam axis. It has a central elliptic hole which, projected into the beam direction, appears as a circular cross section allowing for the electron bunch to pass through.

Due to the inclination of the screen, the diffraction radiation is emitted perpendicularly to the beam axis [CSS05]. This enables extracting it out of the electron beam pipe through a vacuum window. A mirror captures the radiation and focuses it on the detector, where it is converted into an electric signal. Further processing stages comprise

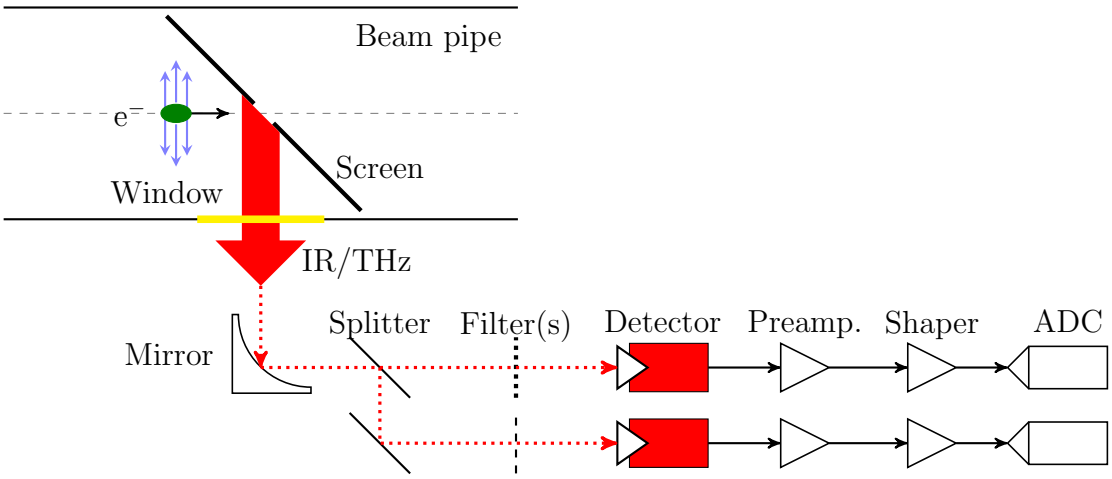

Figure 2.6: Diffraction radiation measurement with BCM. Reproduced from [Pei13, p. 14].

a low-noise pre-amplifier and a shaping circuit. Subsequently, the electric signal is digitised by an analogue-to-digital converter (ADC) and the reading transferred to the accelerator control system.

In order to extend the available measurement range by using multiple detectors of different types or sensitivities, the beam path can be divided into two branches with a splitter. Optional wavelength-dependent filters upstream the detectors enable spectral shaping of the diffraction radiation for an increased sensitivity in the region of interest. Screens with different hole sizes and profiles – e.g. mounted on a movable holder – can be used for controlling the characteristics of the generated diffraction radiation and adapting the system to varying electron beam parameters.

In the current implementation of the BCMs at FLASH and the European XFEL, the ADC output voltage is used as measurement value in the accelerator control system. This quantity can however vary even for constant electron bunch parameters, as it depends not only on the properties of the emitted diffraction radiation, but also on the geometry of the CDR transport path outside of the electron beam pipe. The measured signal intensity is affected by the alignment of the focussing mirror and the exact positions of the detectors, which are movable with the help of motorised mounts. A possible future upgrade could instead use normalised signals in order to eliminate the influence of the CDR beam path geometry.

Spectral Intensity

An analytical derivation for the spectral intensity of the emitted coherent radiation is given in [Wes12]. For small observation angles with respect to the radiation propagation direction, a longitudinal approximation can be used [Wes12, p. 27]:

$$\frac{\mathrm{d}U_{\mathrm{coh}}}{\mathrm{d}\omega} = N^2 \left(\int_{\Omega_\mathrm{a}} \frac{\mathrm{d}^2 U_1}{\mathrm{d}\omega \mathrm{d}\Omega} \left| F_\mathrm{t}(\omega, \Omega) \right|^2 \mathrm{d}\Omega \right) \left| F_\ell(\omega) \right|^2 , \tag{2.1}$$

in which

U_{coh}	spectral intensity of the coherent radiation,
ω	angular frequency,
N	number of electrons per bunch,
Ω	solid angle of the observation point with respect to the radiation propagation,
Ω_a	acceptance solid angle of the radiation transport and detection system,
U_1	single electron spectral intensity,
F_t	transverse form factor,
F_ℓ	longitudinal form factor.

$N = \frac{|q|}{e}$ is given by the bunch charge q, the term in parentheses can for example be obtained from numerical simulations with `THzTransport` [CSS+09]. The longitudinal

form factor is the Fourier transform of the longitudinal charge distribution (i.e. the beam current profile) ρ_ℓ

$$F_\ell(\omega) = \int_{-\infty}^{\infty} \rho_\ell(ct) e^{-i\omega t} \, \mathrm{d}t \,, \tag{2.2}$$

with c denoting the speed of light.

The single electron spectral intensity is affected by the geometry of the diffraction screen [CSS05][Löh09]: the hole allowing for the electron beam to pass through leads to a strong suppression of short wavelengths. The boundary below which a significant reduction occurs decreases with increasing electron beam energy. In addition, the finite size of the diffraction screen causes a reduction of the single electron spectral intensity at long wavelengths. Both effects are taken account of in `THzTransport`.

The spectral intensity of the coherent diffraction radiation is highly dependent on the bunch length and current profile, which makes it eligible for use in a bunch compression monitor. As stated in [CSS05, p. 21]:

> The form factor has the property that $F_{long}(\omega) \to 1$ for $\omega \to 0$, or more accurately, $F_{long}(\omega) \approx 1$ for $\omega \ll 2\pi/T$ where T is the time duration of the bunch. This implies that all electrons radiate coherently and the intensity grows proportional to N^2 if the wavelength exceeds the bunch length.

With N in the order of 10^9 (see Equation 1.4), the incoherent radiation is exceeded by the coherent contribution by several orders of magnitude in intensity and can therefore be neglected. For the bunch lengths commonly used at FLASH and the European XFEL, the coherent radiation emission typically takes place in the infrared regime (q.v. Table 4.2 on page 68).

In order to describe the entire measurement chain, the spectral response of the radiation transport line T and the detection system D must also be known. By multiplying the respective contributions in frequency domain, the total spectral intensity at the detector is obtained. Integration over the whole spectrum then gives the measurement value

$$S = \int_0^{\infty} D(\omega) T(\omega) \frac{\mathrm{d}U_{\mathrm{coh}}}{\mathrm{d}\omega} \, \mathrm{d}\omega \,. \tag{2.3}$$

The measurement principle of the BCM providing a single numerical value from the integration of the coherent diffraction radiation over the entire spectrum does not enable the deduction of the longitudinal bunch profile. It allows for detecting changes of characteristic length scales, such as the overall bunch length or substructures of the bunch. This feature makes it eligible for use in feedback systems where the operating point of the accelerator shall be maintained and only small drifts need to be corrected. It is however not guaranteed that solely by restoring the BCM reading, the accelerator operating point can be re-established from scratch. For measuring the longitudinal bunch profile by means of diffraction radiation, spectrally resolved techniques can be used [Wes12][Wun16].

2.2.2 Installation Locations

At the European XFEL, bunch compression monitors are located in the diagnostics sections up- and downstream of the magnetic chicanes of each of the last two bunch compressors, as shown in Figure 2.7. This placement allows for monitoring and control of the compression scheme at each of the three compression stages along the accelerator (downstream each of the three bunch compressors) as well as correlation and out-of-loop measurements using both central monitors. The two channels per station can be equipped with different detector types. See chapter 4 for more details.

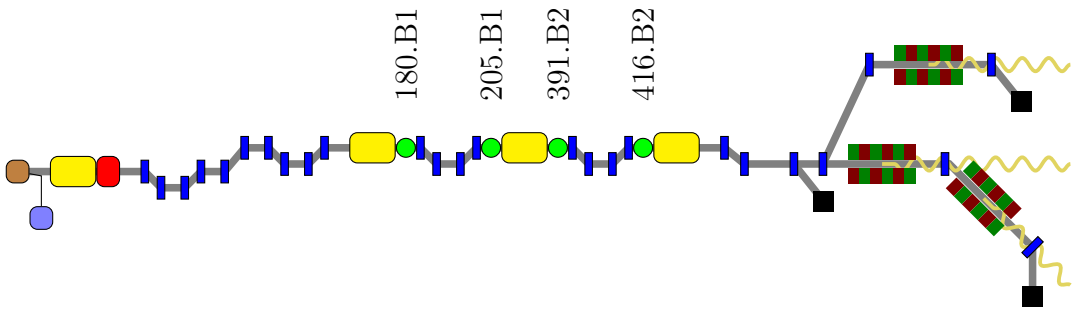

Figure 2.7: Locations and names of the bunch compression monitors at the European XFEL.

FLASH is equipped with bunch compression monitors as well. They are located downstream the magnetic chicanes of each of the two bunch compressors as well as upstream the undulator sections in the individual beamlines, as indicated by green dots in Figure 2.8. The layout and characteristics of the BCMs at FLASH are detailed in [Wes12].

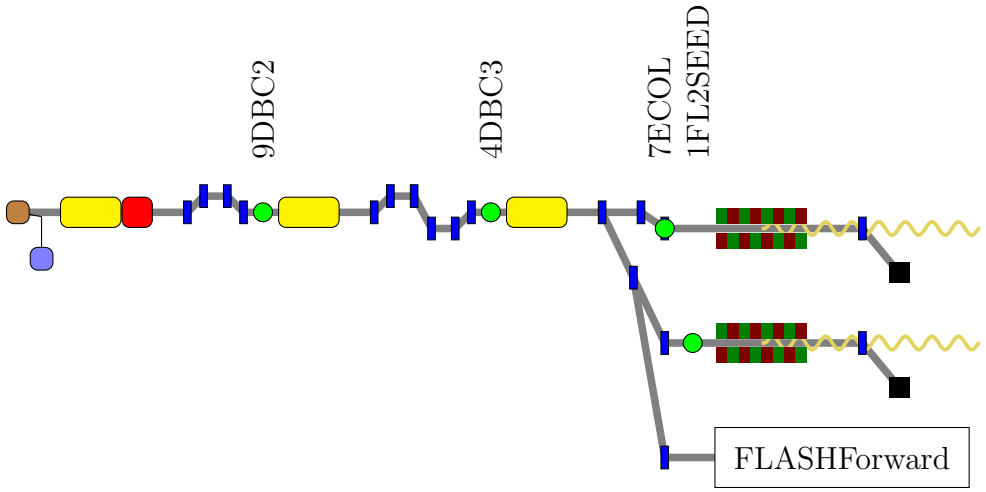

Figure 2.8: Locations and names of the bunch compression monitors at FLASH.

At the first BCM station (labelled '9DBC2' in Figure 2.8), located downstream the magnetic chicane of the first bunch compressor, different sensor types are used for the two measurement channels: one pyroelectric element (coarse channel) and one Schottky diode with a high sensitivity (fine channel). Downstream the magnetic chicane of the second bunch compressor a BCM station (labelled '4DBC3' in Figure 2.8) with two detectors of the same type (pyroelectric element), but with different sensitivities, is installed: one offering a better resolution with the drawback of clipping at high signal levels (fine channel) and one with lower sensitivity (coarse channel). Depending on the accelerator operating point – i.e. the bunch charge and compression scheme – either of the two channels is better suited for measurement. Since the BCM signal scales with the square of the bunch charge, the fine channel is usually used for lower charges and the coarse one for higher charges.

2.2.3 Integration into RF Tweak

Analogously to the bunch arrival time monitor, a module for bunch compression measurements has been developed and integrated into the longitudinal beam dynamics code `RF Tweak 5 GUI` [BDD15] during the course of this work. By instantiating the respective class at user-specified locations along the accelerator lattice, bunch compression measurements can be performed. Like for the BAMs, the list of BCM stations is not hard-coded for a particular facility, but can be adapted to the given machine.

The BCM module comprises all parts of the signal genesis as described in section 2.2.1: single electron spectrum, radiation transport line characteristics and detector responsivity are loaded from data files specific for the chosen location and detector type. The former two are combined in a single data file (created using `THzTransport` [CSS+09]), as they commonly define the spectral intensity at the detector position. The latter one is kept separate in order to support different detector types per station.

Determination of the longitudinal form factor is carried out by computing the fast Fourier transform of the current profile at the specified lattice position. The signal at the detector is then calculated by multiplication of all these values in frequency domain. Finally, the detector reading is obtained via numerical integration of the ADC signal over all frequencies according to Equation 2.3.

For ease of use, a graphical interface has been created in addition to the command line support. A screenshot of the according expert panel is shown in Figure 2.9a. It allows for the selection of a monitor location and type, automatically using the correct data files for single electron spectrum and radiation transport line as well as detector characteristics depending on the user's choice. The corresponding curves are displayed alongside the computed longitudinal form factor and ADC signal[1]. A scroll bar allows for zooming into the frequency axis of the plots for further inspection of the signal genesis.

[1]The BCM voltage readings have a negative polarity with a growing absolute value for increasing signal strength. This behaviour is emulated by the BCM diagnostics module of `RF Tweak 5 GUI`.

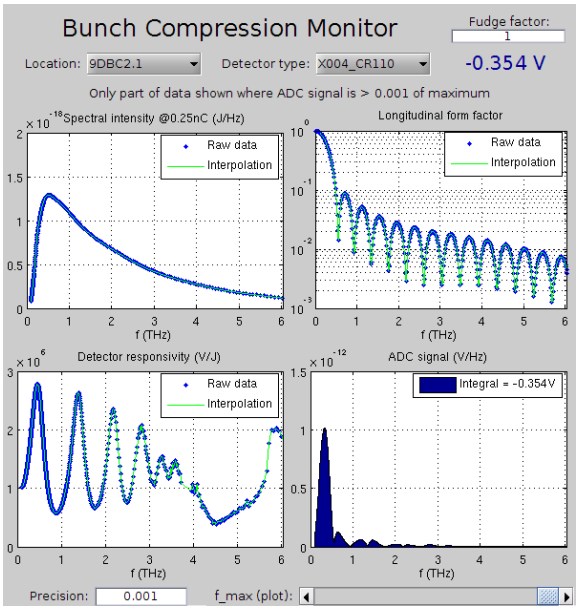

(a) Screenshot of the expert window displaying the signal constituents and the computed detector value (q.v. [BDD15, p. 179]).

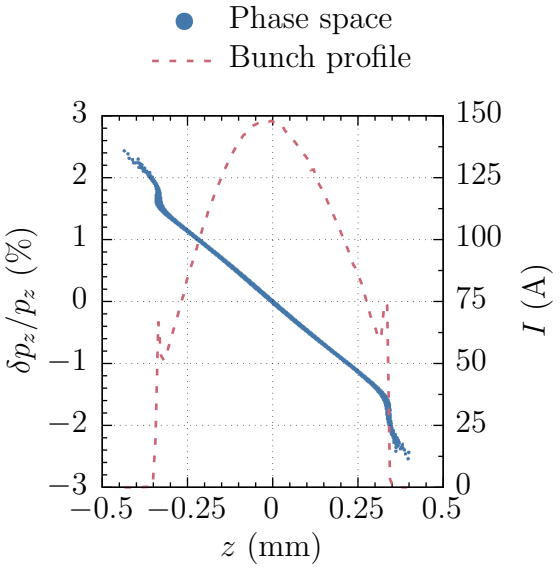

(b) Phase space and bunch profile at the detector location used in Figure 2.9a.

Figure 2.9: Bunch compression monitor in `RF Tweak 5 GUI`.

The internal program logic of the expert window is illustrated in Figure C.1. When the RF settings in `RF Tweak 5 GUI` or any parameter on the panel change, an automatic recomputation is triggered and the values are updated accordingly. As many instances of this window as desired can be opened and operated independently, for instance in order to monitor multiple BCM locations at the same time or to compare different detector types for a specific station.

2.3 Synchrotron Radiation Monitor

Arrival time monitors, as presented in section 2.1, can be used in conjunction with a dispersive beamline section for measuring the energy of the bunch centroid. In addition, it can be beneficial to obtain further information about the energy *distribution* of the particles in the bunch. This property is controlled by higher moments of the accelerating voltage, determined by the amplitude and phase set points of the fundamental and third harmonic modules (see section 1.1). Beam diagnostics sensitive to these quantities can help tuning the machine operating point and provide further monitor data for feedback systems.

2.3.1 Measurement Principle

In a dispersive beam transport section, such as the magnetic chicane of a bunch compressor, a particle's trajectory depends on its momentum (see section 1.1). The relation between the momentum and the transverse displacement in the centre of the chicane is governed by the dispersion parameter (R_{16} in Equation 1.2) for the first half of the system. By recording the transversal particle distribution at this location, the energy spectrum of the bunch can be reconstructed.

The transverse displacement in the centre of the chicane, depending on the bending angle of the beam trajectory, is [Cas03, p. 4]

$$\Delta x = 2l_{\text{eff}} \frac{1 - \cos\alpha}{\sin\alpha} + d\tan\alpha\,, \tag{2.4}$$

in which

x	transverse axis,
z	longitudinal axis,
l_{eff}	effective magnetic length of one dipole,
d	magnet-free distance along z between the first two dipoles,
α	bending angle.

The bending angle is determined by the momentum of the electrons and the magnetic field properties

$$\sin\alpha = \frac{eBl_{\text{eff}}}{p}\,. \tag{2.5}$$

By combining Equation 2.4 and Equation 2.5, a mapping between the particle momentum and the signal position on the detector can be created.

For measuring the transverse distribution of the particle positions inside the chicane in a non-destructive way, synchrotron radiation is used. It is emitted when charged

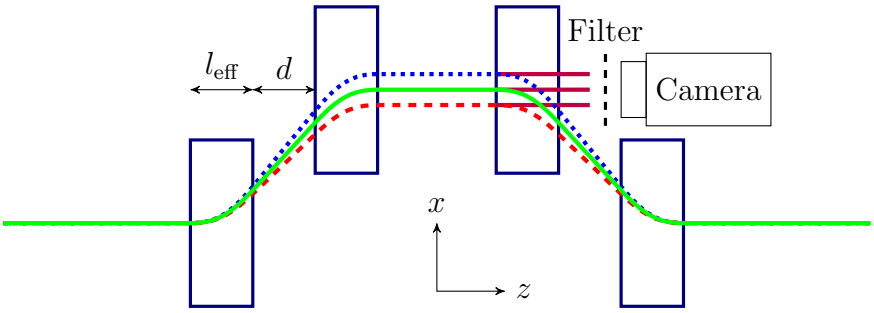

Figure 2.10: Measurement principle of a synchrotron radiation monitor in a magnetic chicane of a bunch compressor. Adapted from [Ger07, p. 150].

particles are deflected in a magnetic field. For ultrarelativistic particles, the synchrotron radiation is collimated in forward direction, tangentially to the beam trajectory [Wie03].

The measurement setup is illustrated in Figure 2.10. A camera pointed at the entrance of the third dipole records the intensity profile of the emitted synchrotron radiation from which an energy histogram is reconstructed. In order to suppress background light and increase the sensitivity in the wavelength range of interest, an optical filter can be installed in the synchrotron radiation propagation path.

The transverse position separation of the particles in the centre of the magnetic chicane caused by dispersion is given by [Cas03, p. 6]

$$D = R_{16} = 2\,\frac{l_{\text{eff}}}{\sin\alpha}\left(\frac{1}{\cos\alpha} - 1\right) + d\,\frac{\tan\alpha}{\cos^2\alpha}\,. \tag{2.6}$$

For the magnetic chicane of the first bunch compressor at FLASH, the standard operating point is $\alpha = 18°$. With $l_{\text{eff}} = d = 0.5\,\text{m}$, this corresponds to $R_{16} = 346\,\text{mm}$. For a momentum deviation of $\frac{\delta p}{p} \approx \pm 2\,\%$, $R_{16} \times \frac{\delta p}{p} \approx \pm 6.9\,\text{mm}$. Hence, the resulting total dispersion-induced beam spread in the centre of the magnetic chicane is 13.8 mm.

The achievable resolution of this method is limited by the transverse beam size which smears out the trajectory displacement information. For the synchrotron radiation monitor (SRM) formerly installed in the magnetic chicane of the first bunch compressor at FLASH [Ger07], the transverse electron beam size without dispersion is $(0.23 \pm 0.02)\,\text{mm}$. This value corresponds to a dispersion-induced displacement caused by 0.07 % relative momentum deviation.

The spatial orientation of the electron bunch has an impact on the achievable measurement resolution, too: if it is tilted in the dispersion plane, the energy histogram is smeared out. By measuring a spectrum, no information on the correlation between the momentum and the longitudinal position of the particles in the bunch is obtained.[2] An initial transverse orbit offset of the bunch entering the chicane changes the centroid position, but not the profile of the signal.

Installation Locations

Currently, no synchrotron radiation monitors are installed at FLASH or the European XFEL. In principle, any C-type magnetic chicane (see Figure 1.3 and Figure 1.5) with a suitable transverse dispersion could be used. Measurements done with a SRM formerly installed in the magnetic chicane of the first bunch compressor at FLASH are presented in [Ger07] and [GBH+12].

[2] For measuring the correlation between the particle momentum and the longitudinal position, a transversely deflecting cavity can be used [Yan16]. However, this method is not suited for intra bunch-train feedback. Due to it being a destructive diagnostics, it can only be used for single bunches of a train.

2.3.2 Integration into RF Tweak

Similarly to the bunch arrival time and bunch compression monitors, a diagnostics module implementing a synchrotron radiation monitor has been developed and integrated into the longitudinal beam dynamics code `RF Tweak 5 GUI` [BDD15]. When instantiating the respective class, the user can either directly pass the R_{16} of the bunch compressor – or the chicane geometry and bending angle, from which the corresponding R_{16} value is computed automatically with help of Equation 2.6. The measurement signal is determined by calculating the transverse displacement of the particles in the centre of the bunch compressor depending on their momentum according to Equation 1.2. User-specified values for the detector size and resolution are used for binning the resulting spectrum to the individual pixels.

For ease of use, a graphical interface has been created in addition to the command line support. A screenshot of the according expert panel is shown in Figure 2.11a. It allows for the selection of a monitor location and detector geometry (size and number of pixels). For the chosen location, the correct dispersion value is automatically calculated from the `RF Tweak 5 GUI` magnet settings of the respective chicane and displayed on the panel. From the user-specified detector geometry, the resulting resolution and pixel

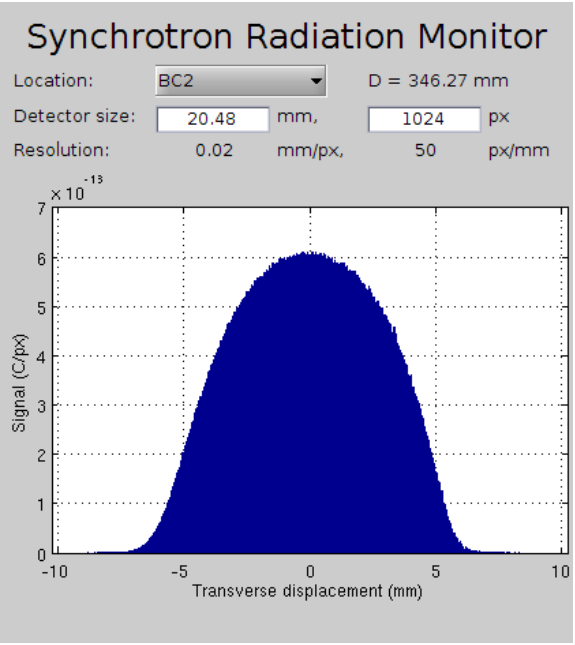

(a) Screenshot of the expert window displaying the computed detector signal (q.v. [BDD15, p. 179]).

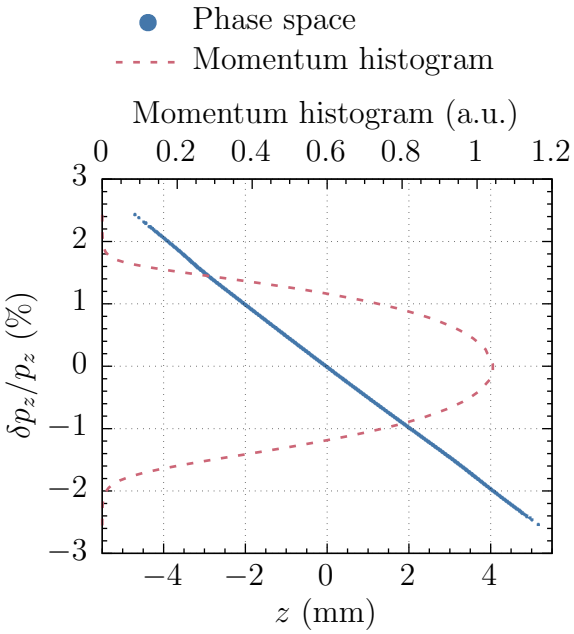

(b) Phase space and momentum histogram upstream the magnetic chicane in which the detector used in Figure 2.11a is installed.

Figure 2.11: Synchrotron radiation monitor in `RF Tweak 5 GUI`.

size are calculated. The computed signal is displayed in a histogram plot as charge equivalent per pixel.

Like for the BAMs and BCMs, the list of possible SRM locations is not hard-coded for a particular facility. Instead, it is automatically generated from the accelerator lattice, supporting all C-type bunch compressors. When the RF parameters or magnet settings in `RF Tweak 5 GUI` or any parameter on the panel change, an automatic re-computation of the signal is triggered. As many instances of the expert window as desired can be opened and operated independently, for instance in order to monitor multiple SRM locations at the same time or to compare different detector geometries for a specific station. A flow chart of the program logic is shown in Figure C.2.

2.4 Feedback Concept

Measurement and regulating devices are subject to drifts over time. For an accelerator – being a complex system composed of a variety of subcomponents – drifts influence the machine working point and the general performance of the facility. They can be of various kinds and occur on a wide range of time scales, like dependencies on temperature changes over the course of a day or detuning of accelerating cavities caused by microphonics in a range up to a few hundred hertz [Sch10, p. 16]. Fast fluctuations – such as injector laser timing or intensity jitter and RF field instabilities – can even affect individual bunches within a train (see sections 1.2 and 1.3 for details on the bunch pattern at FLASH and the European XFEL).

As varying electron beam parameters result in changing photon characteristics, drifts and instabilities can influence the user experiments as well. Pump-probe methods, for example, are sensitive to timing changes. Bunch compression and peak current variations affect the intensity of the generated undulator radiation. In order to minimise drifts and jitter of photon characteristics relevant for the user experiments, the underlying electron beam properties need to be stabilised.

By using beam diagnostics elements as monitors in one or multiple feedback loops, deviations of acceleration characteristics can be detected and corrected. Drift compensation ensures that the beam properties and thus the machine operating point are kept stable over time. These actions can be automated or manually controlled and occur on different time scales – just like the drifts they aim to compensate. The actuator of a feedback loop is usually located upstream the respective monitor, due to the principle of causality.[3]

An example of manual feedback is a human operator observing and tuning the accelerator working point in order to compensate for drifts. This process typically takes place on time scales of minutes to hours. On the other hand, fast feedbacks are used for regulation on consecutive bunches within a single macropulse (intra bunch-train feedback).

[3] An exception to this principle is a predictive system, in which the actuator is located downstream the monitor.

Due to the high bunch repetition rates of up to 1 MHz at FLASH and up to 4.5 MHz at the European XFEL, those systems operate in an automated manner. In between these extremes, feedback loops with different regulation speeds can be established.

Depending on the system characteristics and the regarded time scales, different actuators qualify for implementing the feedback. The bunch arrival time, for example, is influenced by the electron beam dynamics in the bunch compression sections upstream the respective monitor. According to Equation 1.6, it can be varied by either changing the lattice properties (R_{56}) or the particle momentum in the chicane.

The former – being defined by the magnetic field strength and the chicane geometry – can only be modified on a relatively slow time scale in the order of seconds by adjusting the magnet currents. The chicane geometry is fixed at FLASH and the European XFEL. Varying the lattice properties is therefore not suited for realising a fast feedback system.

The particle momentum, on the other hand, is defined by the RF set points of the accelerating modules. These can be adjusted on very short time scales, from pulse to pulse and even within the same macropulse. For a fast feedback system, this is therefore the actuator of choice. The same argument applies to the bunch compression.

Figure 2.12 shows an example of a combined feedback system. This particular scheme is implemented in the low-level radio frequency (LLRF) controllers at FLASH and the European XFEL. It is part of the regulation for the amplitude and phase of the electromagnetic field inside the accelerating cavities.

The plant $\mathbf{G}(z)$, given for example as transfer function in discrete time domain (z), comprises all components of the RF signal chain except for the controller. Those comprise the vector modulator, pre-amplifier, klystron, RF waveguides, power couplers, accelerating cavities, pick-ups and RF cabling. Its input u is determined by the sum of the output of the controller $\mathbf{C}(z)$ and the feedforward signal u_{FF}. The plant outputs are

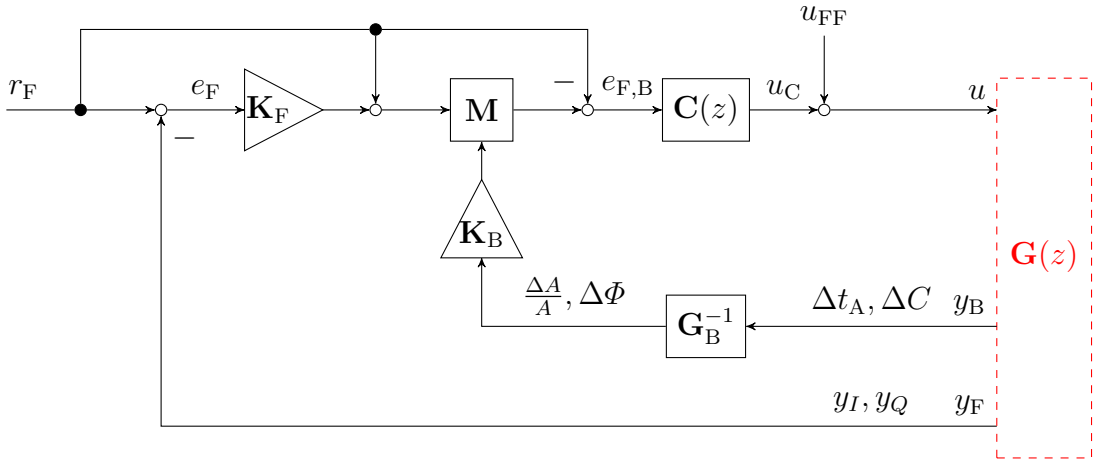

Figure 2.12: Cascaded feedback structure for merging field and beam error. Reproduced from [Pfe14, p. 86].

RF field measurements using pick-ups (y_F) and beam-based signals (y_B), such as deviations of the bunch arrival time (Δt_A) and bunch compression (ΔC) from the chosen accelerator operating point.

A beam-based feedback matrix $\mathbf{G}_\mathrm{B}^{-1}$ transforms the measured diagnostics deviations into relative amplitude and absolute phase errors, which are scaled proportionally using a diagonal weighting matrix $\mathbf{K}_\mathrm{B}$. The field measurement is subtracted from a reference value r_F and the resulting field error e_F likewise scaled proportionally with a weighting matrix $\mathbf{K}_\mathrm{F}$. The matrices $\mathbf{K}_\mathrm{B}$ and $\mathbf{K}_\mathrm{F}$ can be chosen independently. After adding again the reference value to the scaled field error signal, it is combined with the beam-based error signal using a modulation matrix $\mathbf{M}$.

By merging the field and beam errors, a regulation taking both sources into account is realised [Pfe14]. The scaling matrices $\mathbf{K}_\mathrm{F}$ and $\mathbf{K}_\mathrm{B}$ allow for a different weighting of the field and beam-based components in the combined error signal $e_\mathrm{F,B}$. From the resulting value, the total error with respect to the reference r_F is computed and used as input of the controller $\mathbf{C}(z)$.

By lifting up the scaled field error to the working point, modulating it with the beam-based error signal and transferring back the result to the error scale, the working point dependency of the control parameters is eliminated. A measurement demonstrating the effect of independently varying $\mathbf{K}_\mathrm{F}$ and $\mathbf{K}_\mathrm{B}$ on the feedback performance is shown in section 6.3.1.

In order to achieve a high regulation speed, the feedback algorithm is implemented in the LLRF controller firmware running on a field-programmable gate array (FPGA). The data transfer from the beam diagnostics to the controller is realised using optical high-speed low-latency links.

All signals are subject to disturbance. For the purpose of readability, signal errors are not incorporated in Figure 2.12. A more detailed schematic including sources of signal disturbance is given in Figure 5.13 on page 87.

3 Electro-Optical Unit for the New Bunch Arrival Time Monitor for FLASH and the European XFEL

The signal acquisition and processing scheme of the bunch arrival time monitor (BAM) system – as described in section 2.1.2 – is realised in a structured manner [Boc12] which is shown diagrammatically in Figure 3.1. Pick-ups in the beamline detecting the electric field of the passing electron bunches and the associated radio frequency components for signal combination and transport are referred to as *RF unit*. In the *electro-optical unit*, the electric signals are used for modulating time-stabilised reference laser pulses provided by the optical synchronisation system. The modulated laser signals are then digitised by *electronics for readout and control*, where further data processing in firmware and high-level software as well as the integration into the accelerator control system takes place.

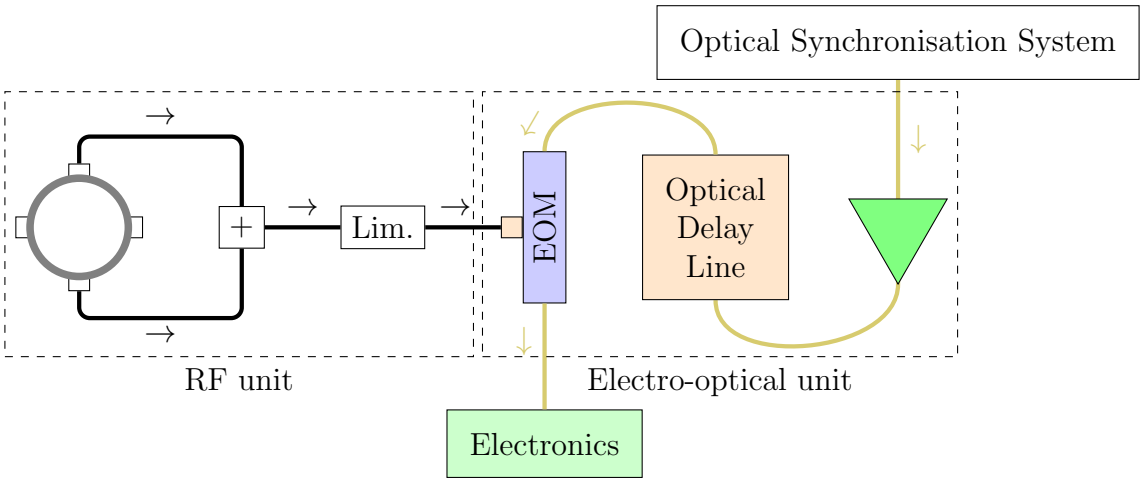

Figure 3.1: Structuring of the BAM signal acquisition and processing chain. The arrows indicate the signal flow. Cabling scheme adapted from [DCG+15, p. 478].

3.1 Optical Signal Flow

From the optical signal processing point of view, the purpose of this system is to distribute the time-stabilised laser pulses – which are provided by the optical synchronisation system – to the different data acquisition channels of the readout electronics. This is realised according to the scheme depicted in Figure 3.2. All components and connections are carried out using polarisation-maintaining fibre optics with the exception of the motorised delay stages, which comprise both fibre and free-space parts.

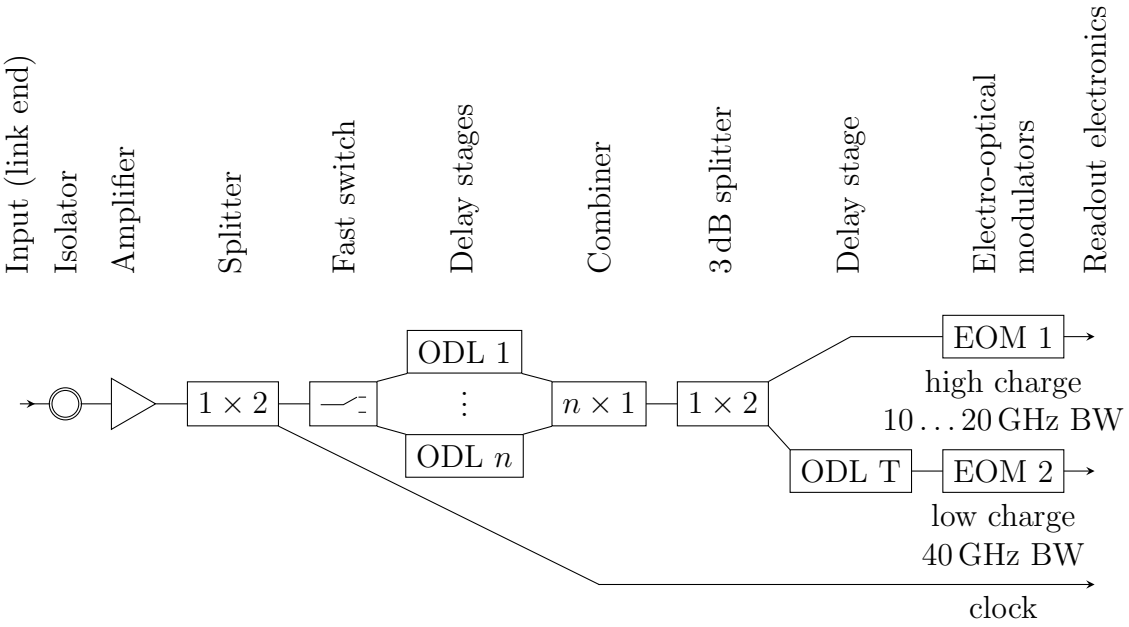

Figure 3.2: Optical signal flow inside the new BAM electro-optical unit.

The input of the signal chain is the end of the stabilised fibre link coming from the laser-based synchronisation system. An optical isolator serves as a boundary preventing light from travelling back upwards the link. The following amplification section raises the signal level to make use of the full dynamic range of the digitising electronics components. Subsequently, part of the light is split off for the generation of a reference clock signal for the analogue-to-digital converters.

As shown in section 2.1.2, an optical delay line (ODL) is needed for adjusting the timing between the electric pick-up signals generated by the electron bunches and the optical reference pulses coming from the master laser oscillator. However, at FLASH and the European XFEL, bunches destined for different SASE beamlines are combined into one single train in the common part of the accelerator (see section 1.2 and section 1.3 for details). These sub-macropulses can be generated by separate injector lasers and transported with different accelerating settings leading to individual timing character-

istics of the respective bunches. This implies that the delay stage position would need to be updated for every sub-train within a macropulse.

The transition times between the sub-macropulses are in the order of 40 µs, which is the duration needed by the low-level RF system to accordingly update the field gradients and phases inside the accelerating cavities. A mechanical motor stage is not able to change its position reliably and with the needed precision in such a short time.[1] Furthermore, constantly driving a stage with the macropulse repetition rate of 10 Hz would lead to increased wear and rapid mechanical failure. It is therefore not feasible to use one common optical delay stage to adjust the timing for all sub-macropulses.

Rather than that, up to three stages – labelled 'ODL 1' through 'ODL n' in Figure 3.2 – are used for timing adjustment, one per individual SASE beamline. A fast optical switch (see section 3.4) selects the respective delay stage for each sub-macropulse. Consequently, the actual number of stages installed inside a particular electro-optical unit depends on the location of the device along the accelerator. In the common part of the linac, bunches for all SASE beamlines are transported, whereas in the single beamlines at the end of the machine only certain sub-macropulses are present, reducing the number of required motor stages. Table 3.1 lists the numbers for the individual stations at FLASH and the European XFEL as planned for the final installation state.

After traversing the delay stages, the signals are merged again for further processing.[2] The signal is then split up one more time and fed into the two electro-optical modulators (EOMs) for the two channels per BAM (high charge and low charge). An additional small optical delay stage with an adjustment range of 100 ps – labelled 'ODL T' in Figure 3.2 – is used for setting the relative timing between the two EOMs. In a final step, the optical signals are passed on to the readout electronics, sampled with fast photodiodes and further processed in digital form.

[1] The employed model *OWIS LIMES 60*, which has been chosen for its high positioning accuracy, supports a maximum driving velocity of $v_{\max} = 30\,\mathrm{mm/s}$ [OWI]. Using the delay stage in single-pass configuration as defined on page 53, this corresponds to a timing adjustment rate of $2 \times v_{\max}/c \approx 2 \times 10^{-10} = 200\,\mathrm{ps/s}$. In the 40 µs time frame available for switching between succeeding sub-macropulses, this would allow for a delay adjustment of only 8 fs, which is smaller than the timing change typically expected between subsequent sub-macropulses. When taking the time needed for acceleration and deceleration of the stage into account, this amount is even further reduced.

[2] Mapping of the laser pulses corresponding to bunches for different SASE beamlines is done later in the readout electronics using the bunch pattern information provided by the timing system.

Station	n
1UBC2	3
3DBC2	3
4DBC3	3
15ACC7	3
1SFELC	1
21FL2EXTR	1
8FL2BURN	1
FLASHFWD	1
Overall	16

(a) FLASH

Station	n
47.I1	3
181.B1	3
203.B1	3
392.B2	3
414.B2	3
1932M.TL	3
1932S.TL	3
SASE1	2
SASE2	1
SASE3	2
Overall	26

(b) European XFEL

Table 3.1: Number of optical delay stages needed for the individual bunch arrival time monitor stations at FLASH and the European XFEL (final installation state, without 'ODL T'). For details on the installation locations see Figure 2.3 on page 25 and Figure 2.5 on page 27.

3.2 Physical Composition

The BAM electro-optical unit is implemented as a 19-inch module. It is divided horizontally into two compartments [DCG+15, p. 481] which are separated by a thermally insulating base plate. An overview of the components installed in the system and the cabling scheme illustrating their interconnections is given in Figure 3.3.

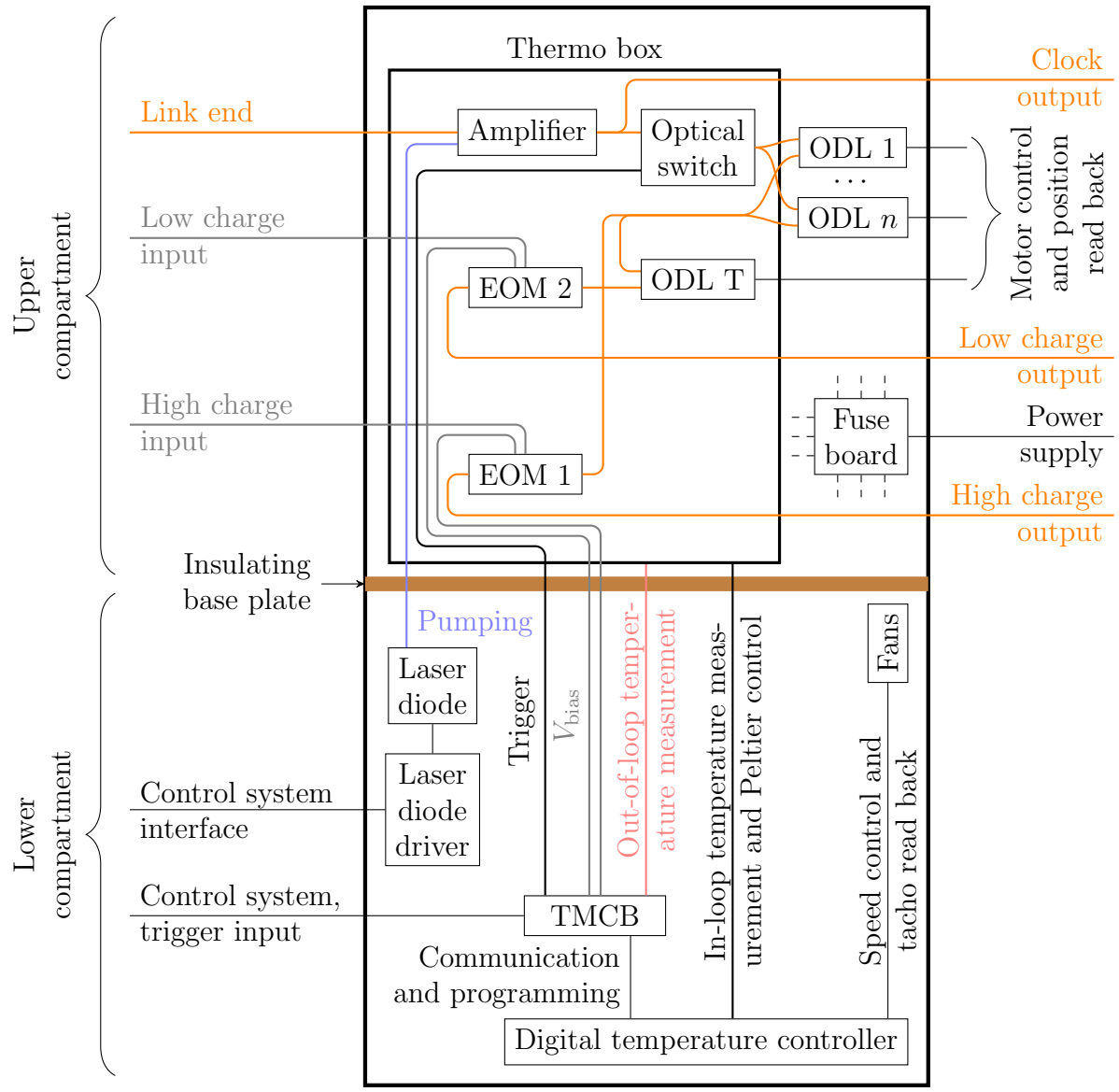

Figure 3.3: Cabling scheme of the new BAM electro-optical unit. For reasons of readability, the power distribution lines from the fuse board to the other components are not shown.

Figure 3.4 shows a photograph of the upper compartment. It houses the components involved in the optical signal flow as described in section 3.1 and parts of the RF unit (limiter and coupler). Elements susceptible to temperature-induced drift – such as fibre-optical and RF components – are installed in a separate area (labelled 'thermo box' in Figure 3.4). This partition is actively temperature stabilised with the help of a digital controller acting on Peltier elements which are attached to a metallic base plate (q.v. section 3.5.2). For thermal insulation, the thermo box has plastic walls and is encased in

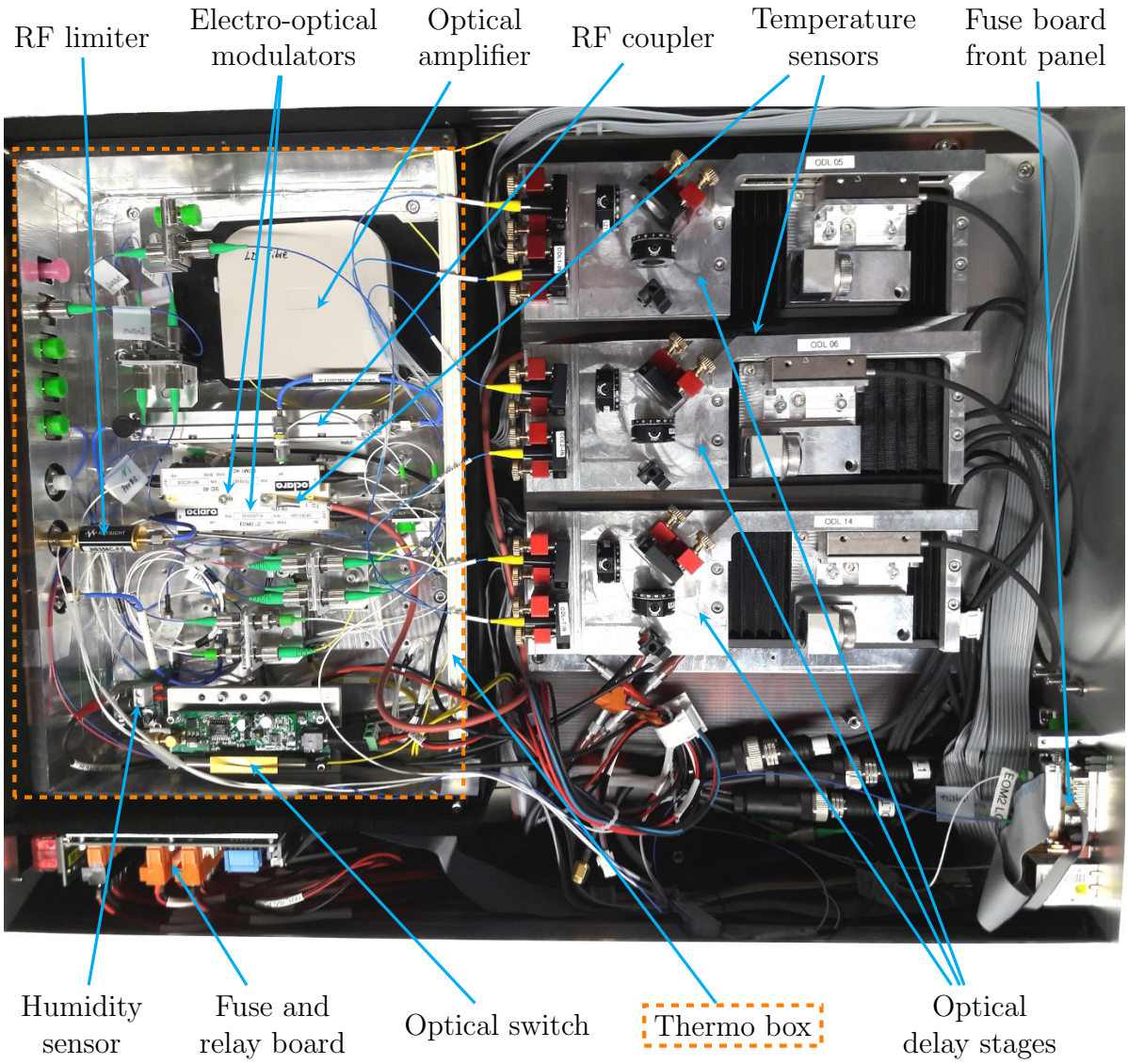

Figure 3.4: Photograph of the upper compartment of the new BAM electro-optical unit. Photograph courtesy of [Czw].

foam rubber. The inner surface is lined with metal foil. This containment additionally serves as a passive humidity stabilisation.

Outside of the thermo box, a holder plate is installed on which the optical delay stages are mounted (see section 3.3). A multichannel fuse and relay board allows for the remote switching and monitoring of the various electronic subsystems. It is interfaced and programmed via a connector board mounted on the front panel of the 19-inch module. Sensors for temperature and humidity monitoring are installed at various locations.

Figure 3.5 shows a photograph of the electro-optical unit's lower compartment. It houses components which introduce heat load and are therefore physically separated from the temperature-sensitive elements in the upper partition. A laser diode powered by a dedicated driver board generates the pumping light for the optical amplifier. The general purpose temperature monitoring and controls board (TMCB) features several analogue and digital input-output ports as well as a field-programmable gate array (FPGA) for

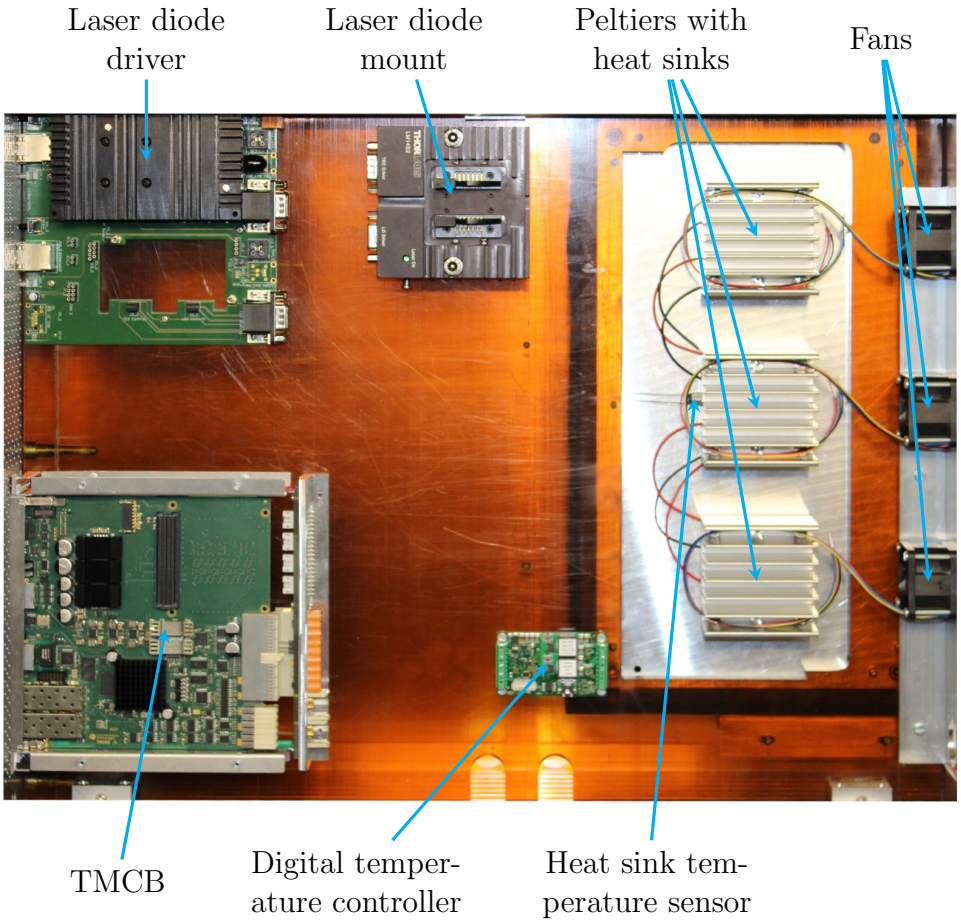

Figure 3.5: Photograph of the lower compartment of the new BAM electro-optical unit (before cabling). Photograph adapted from [DCG+15, p. 481].

logic applications. It is used for the communication with the machine control system, triggering the optical switch and setting the bias voltages of the electro-optical modulators. In addition, it performs the communication with the digital temperature controller and the readout of the out-of-loop temperature sensors installed at various locations in the unit.

A cut-out in the insulating base plate enables access to the metallic bottom side of the thermo box. Three Peltier elements driven by a digital controller are used for temperature stabilisation. Attached heat sinks ensure stable operating conditions of the Peltier elements by leading away excessive heat from their bottom sides and preventing thermal runaway.

Fans mounted on the back side of the 19-inch module suck air through the lower compartment for ventilation. For this purpose, the front panel has vent holes in the lower part (see Figure 3.6). The fan speed is regulated depending on the temperature of the heat sinks. This task is also performed by the digital temperature controller.

Figure 3.6: Front view photograph of the new BAM electro-optical unit.

Interconnections to other systems are established via connectors on the front and back sides. Figure 3.6 shows a photograph of the module's front panel featuring connectors for the optical outputs (clock and data), motor control and the interface to the laser diode driver. The connector board of the fuse and relay module with the main power switch is accessible here as well. A slot holds the TMCB. Further connectors allow access to diagnostic signals tapped at various points of the signal processing chain.

Figure 3.7 shows a photograph of the module's back side. It provides connectors for the stabilised fibre-link from the laser-based synchronisation system, the RF cables carrying the electric pick-up signals and the power cable. The fuse box is located behind a detachable cover. The fans are mounted on a separate holder plate for ease of maintenance. Additional connectors are available for diagnostics and expandability purposes.

At every BAM station, the electro-optical unit is installed in a rack close to the electron beamline in order to minimise the length of the thermally unstabilised signal cables.

Figure 3.7: Rear view photograph of the new BAM electro-optical unit.

A power supply module provides different operating voltages needed by the various electronic components. Sampling of the modulated laser pulses and further processing in digital form is carried out by the readout electronics located in a MicroTCA chassis. Figure 3.8 shows a photograph of the BAM rack at the injector beamline of the European XFEL with all subsystems installed.

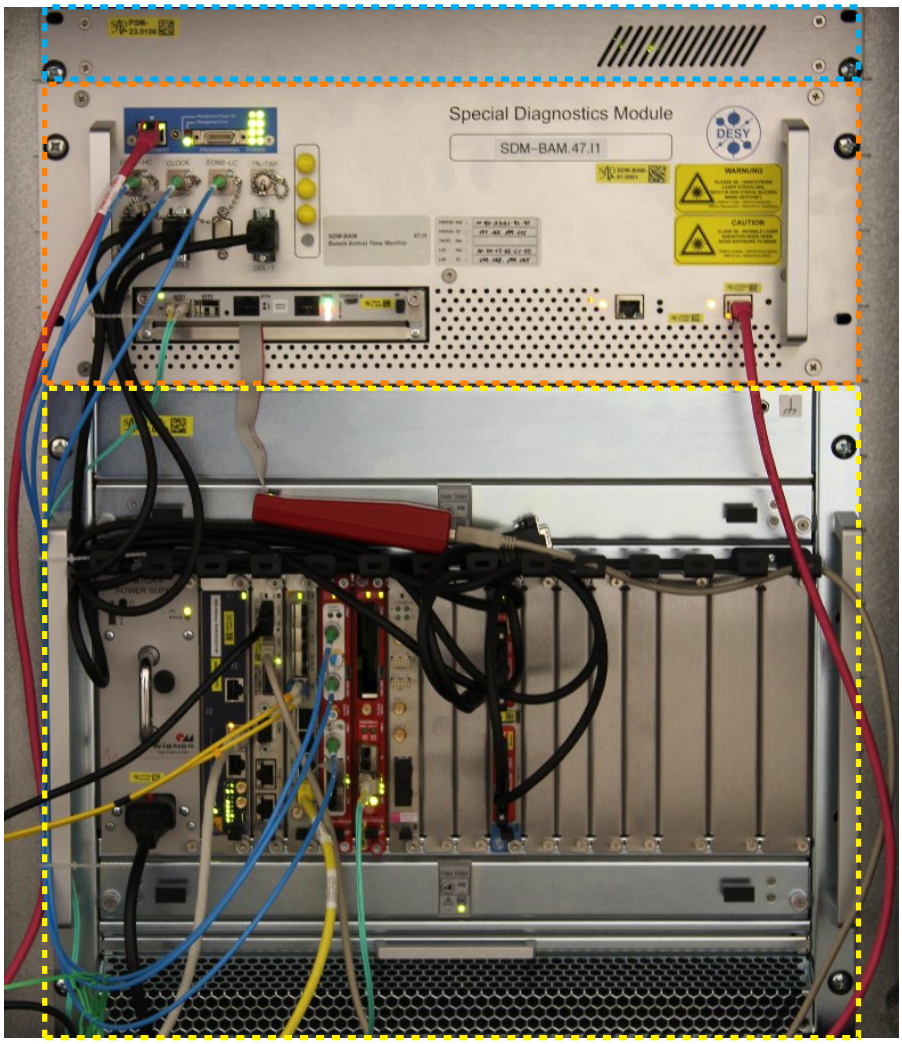

Figure 3.8: Photograph of an electronics rack housing the new BAM electro-optical unit as well as associated components.

3.3 Optical Delay Stage

As shown in section 3.1, each electro-optical unit contains up to three motorised delay stages for adjusting the timing between the reference laser pulses from the optical synchronisation system and the RF signals from the electron bunches of the different sub-macropulses. The actual number of stages installed inside a unit depends on its location along the accelerator. In order to facilitate the setup and pre-alignment of the optical components, the delay stages are mounted on a dedicated holder plate which is then installed in the BAM electro-optical unit. Figure 3.9 shows an example equipped with two devices.

The adjustable time delay is realised by providing a means to change the optical path length of the system. For this purpose, the stage is built using free-space optics with a retro-reflecting prism mounted on a motorised movable slide, as shown in Figure 3.10.

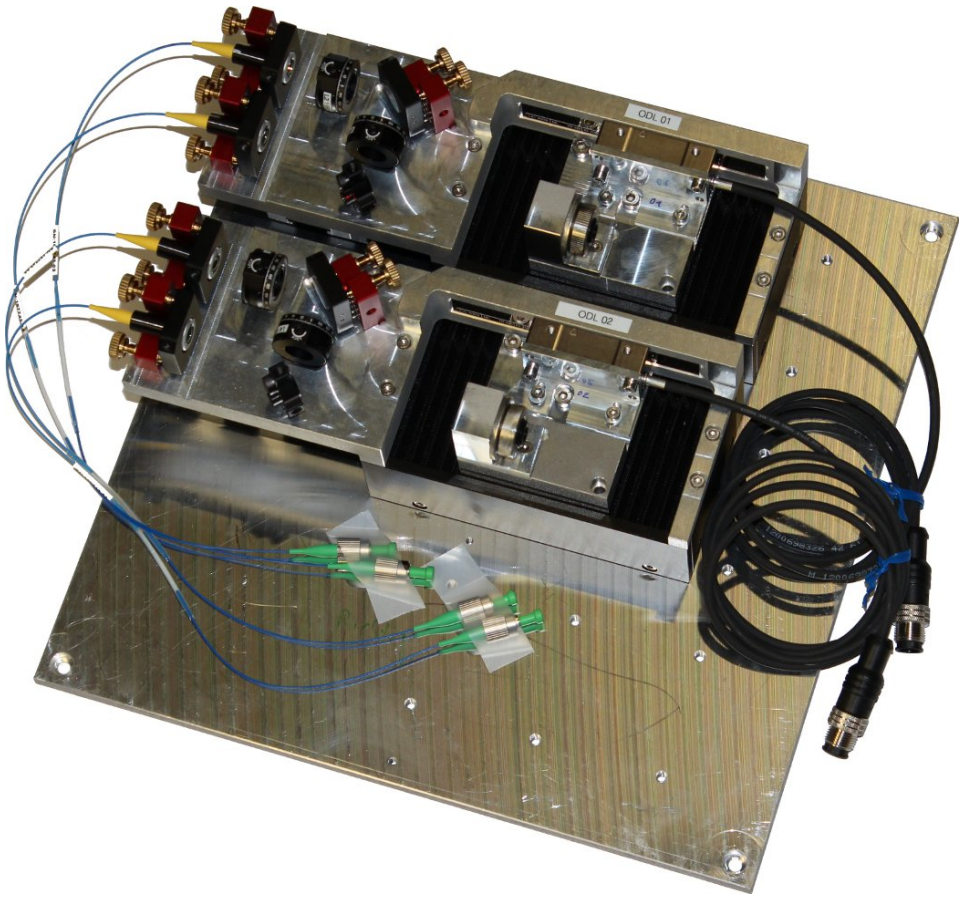

Figure 3.9: Photograph of two optical delay stages, mounted on a common holder plate and pre-aligned before installation in the new BAM electro-optical unit. The holder plate supports up to three delay stages.

Due to the constancy of the speed of light[3], a variation of the retroreflector's position results in a timing change of the laser pulses. When driving the motor by an amount Δx the optical path length of the system changes by $2\Delta x$, as the light passes the travelling distance of the stage twice. Consequently the transition time of the laser pulses is shifted by $\Delta t = 2\Delta x/c$.

The type of the motorised stages[4] has been chosen for its high positioning accuracy and suitability for precision applications. It is eligible for continuous operation, also in industrial environments. A stepper motor drives a spindle that then moves the slide on which the retro-reflecting prism is mounted. A high precision optical position encoder[5] attached to the movable motor slide in combination with a measurement tape fixed to the stage frame is used for gauging the current absolute delay setting.

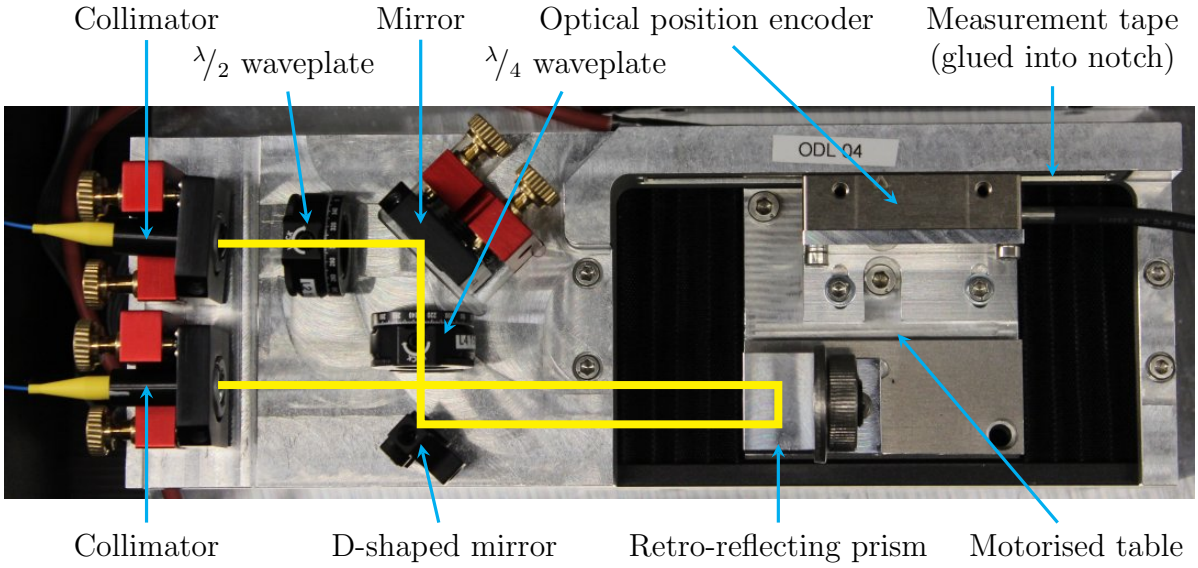

Figure 3.10: Optical path through the delay stage (single-pass configuration).

Figure 3.10 shows the path of the laser pulses through the device. The transition between fibre and free-space optics is realised using two collimators with 2.1 mm beam diameter. All optical components have half-inch size in order to keep the system dimensions compact.

[3]This is of course a simplification. In a medium like air, the refractive index and thus the speed of light depends on external factors such as temperature, humidity and barometric pressure. Additionally, the metallic delay stage body experiences thermal expansion or contraction in case of temperature variations, changing the optical path length. However, the corresponding coefficients are small and the optical delay is corrected periodically using a feedback loop, as the electron bunch timing in the accelerator changes as well. Hence, these effects don't imply a limitation of the working principle itself. For a more detailed analysis of the timing changes caused by environmental fluctuations see section 3.5.

[4]OWIS LIMES 60

[5]Heidenhain LIC 4019

Guiding of the laser through the stage is done by two mirrors with anti-reflective coating, one of which having full size and the other being D-shaped in order not to block the beam path between the retro-reflecting prism and the opposed collimator. Two waveplates – one $\lambda/2$ and one $\lambda/4$ – allow for polarisation adjustments. This is necessary due to the use of polarisation dependent components further downstream the signal processing chain, like the fibre-optic switch (see for example the curve labelled 'wrong polarisation' in Figure 3.15 on page 59).

During the course of this work, an alignment and testing routine for the optical delay stages has been developed, which was then further refined during the assembly process.[6] Two operation options are available, both having been evaluated and proven working:

Single-pass configuration using two separate collimators for optical input and output. The delay stage is passed only once as shown in Figure 3.10. For a travelling range of 40 mm, the adjustable time delay is $2 \times 40\,\mathrm{mm}/c \approx 267\,\mathrm{ps}$. The factor of 2 originates from the use of the retro-reflecting prism, which causes the laser light to pass the distance of the stage twice.

Double-pass configuration using one collimator for both optical input and output. The signals are then split outside the stage using an optical circulator. A flat mirror is installed in place of the second collimator, sending back the laser pulses the same way as they come. The maximum time delay is $4 \times 40\,\mathrm{mm}/c \approx 534\,\mathrm{ps}$ with the light passing the travelling distance of the stage four times.

The alignment precision and overall performance have been measured and optimised. During motor stage movements, the displacement of the laser beam on the retroreflector is smaller than 50 µm over the whole travelling range. In the same time, the optical power at the output varies less than 2 % peak-to-peak in single-pass configuration, as verified for 12 separate delay stages.

3.3.1 Beam Profiler Camera Tool

In order to keep the transmission of the laser through the delay stage constant when driving the motor, the pointing of the beam between the retro-reflecting prism and the opposing collimator must be independent of the actual position of the motorised slide. This is achieved by tuning the angular orientation of the collimator in such way that the beam runs parallel to the driving direction of the stage. The corresponding procedure involves moving the motor back and forth multiple times, iteratively correcting the horizontal and vertical alignment of the collimator as appropriate.

By using a camera in place of the retro-reflecting prism, this scheme can be simplified such that the correct alignment of the opposing collimator is obtained in one step. For this purpose, a computer software with a graphical user interface displaying and

[6] The complete procedure is described in detail in Appendix A.

analysing the captured image has been developed during the course of this work. The location of the laser spot on the camera is recorded at both end positions of the motor stage and the optimal target is calculated with help of a lever mechanism (for details see section A.7.2). When the correct lever ratio is used, steering the beam to this position aligns the collimator in a single step.

The camera software has been used in the alignment procedure of the delay stages for all new electro-optical units and has in the meantime become a standard tool in other laboratories as well. A detailed description of the graphical user interface and the program functionality can be found in section A.3.

3.4 Fibre-Optic Switch

A fast switch is used for the distribution of optical signals from different sub-macropulses to the respective motorised delay stages. The transition time for shifting from one output to another must be shorter than the 40 µs long gap between the consecutive sub-trains (see section 3.1 for details). With a macropulse repetition rate of 10 Hz at both FLASH and European XFEL, the switch must support an operating speed of at least this amount.

Figure 3.11: Photograph of the Agiltron NanoSpeed^{TM} 1×2 fibre-optic switch [Agid].

The device employed for this purpose is a 1×2 fibre-optic switch, shown in Figure 3.11.[7] It is a solid state component without moving mechanical parts, facilitating bidirectional multiplexing between a single fibre on one side and either of two fibres on the other side. Triggering is done with a TTL signal via an external electronic driver board.

[7] Other devices are commercially available, however they do not fulfil the requirements needed for fast switching or long-term operation: Electro-optical (crystal-based) products have switching times of up to 200 µs [Agia]. Opto-micro-electro-mechanical systems (MEMS) based devices have moving parts, resulting in even longer switching times in the order of 10 ms and a limited durability of 10^6 to 10^9 cycles [Agib][Agic][OZ][DiC]. At a macropulse repetition rate of 10 Hz this corresponds to a lifetime of only a day to a few years, which would considerably limit the possible period of application of the bunch arrival time monitor or require frequent maintenance access to replace worn out components.

Property	Unit	Specified [Agid]	Required
Central wavelength	nm	780 . . . 1650	1550
Response time (rise, fall)	µs	≤ 0.3	< 40
Repetition rate	kHz	0 . . . 500	0.01
Operating temperature	°C	−5 . . . 70	25
Optical power handling	mW	≤ 300	10

Table 3.2: Operating properties of the Agiltron NanoSpeed™ 1×2 fibre-optic switch compared to the requirements for the intended use. All demands are met by the specifications.

Table 3.2 lists the relevant operating parameters according to the device's data sheet [Agid] compared with the requirements for the intended application. From this comparison, it turns out that all demands are fulfilled and the component appears to be suitable for use in the system. In order to verify the performance of the chosen device in practice, the fibre-optic switch has been characterised in a laboratory setup and its suitability for the intended use has been analysed.

Connector name	Fibre colour	Purpose
Common	Yellow	Common input/output
①	Red	Active when switch is in Off-state
②	Blue	Active when switch is in On-state

Table 3.3: Optical connectors of the Agiltron NanoSpeed™ 1×2 fibre-optic switch.

The tested device has a single fibre on one side and two fibres on the other side between which the multiplexing is performed. Table 3.3 lists the nomenclature for the connectors of this component – identifiable by the coating colour of the respective optical fibres – which is used in the following. For applications in which switching capabilities with more than two fibres on one side are needed, this can be achieved by stacking multiple 1×2 devices as indicated in Figure 3.12.

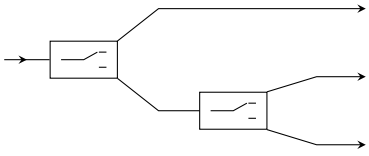

Figure 3.12: Stacking of multiple 1×2 switches in order to support more than two signal paths.

3.4.1 Switching Operation

The switching performance of the device has been tested with a continuous wave laser source. For this measurement, light is fed into the *Common* connector and a photodiode attached to one of the switchable ports is used for measuring the optical intensity over time with an oscilloscope. A pulse generator delivers the TTL signal for controlling the switching state and rate and provides the trigger source for the oscilloscope. The overall cabling scheme used for this measurement is shown in Figure 3.13.

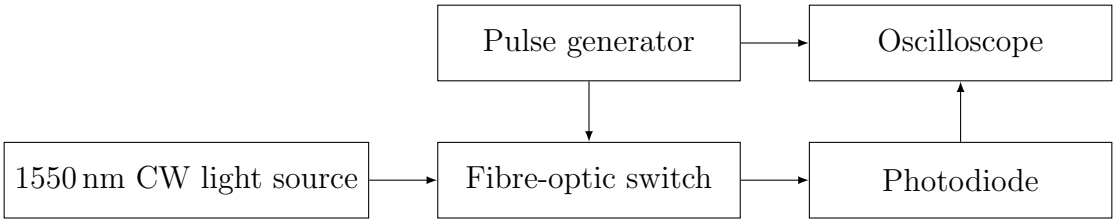

Figure 3.13: Switching test of the fibre-optic switch: principle of measurement.

The tested device is equipped with a driver circuit board permitting 100 kHz operation, which is well above the required value of 10 Hz. Driver units supporting up to 500 kHz are available, but not needed for the intended use. In Figure 3.14, an oscilloscope trace of the optical output signal recorded at one of the switchable ports is shown. Some flat top disturbances can be observed, however they are small (less than 10 %) compared to the absolute switched signal level. The 100 kHz repetition rate is reached.

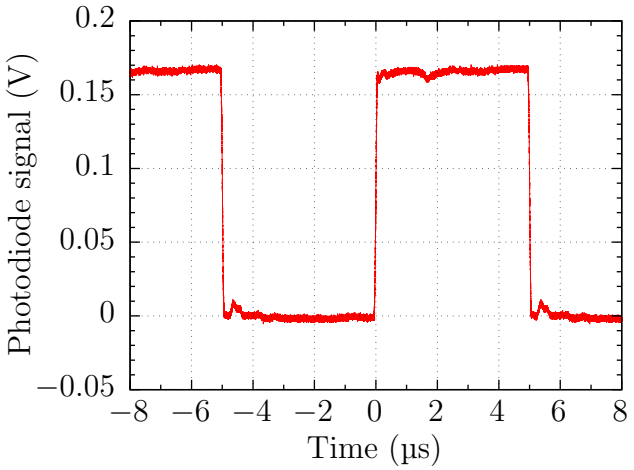

Figure 3.14: 100 kHz operation of the fibre-optic switch. Output signal measured at connector (1).

3.4.2 Transition Times

As described, the switching duration must be below 40 µs in order to be able to separate the individual bunch sub-trains. Table 3.4 lists the rise and fall times measured for light passing through individual ports of the device in different directions. In all possible configurations, the timing requirements are fulfilled.

Input	Output	Rise time (ns)	Fall time (ns)
Common	①	65	65
	②	70	104
②	*Common*	67	95
①		70	95

Table 3.4: Transition times of the measured fibre-optic switch, defined between the 10 % and 90 % levels of the output amplitude.

3.4.3 Transmission

The transmission of the optical signal through different ports of the switch has been measured for a single pass in both directions. Additionally, the signal level at the respective inactive port has been recorded in order to estimate the separation performance and detect possible crosstalk issues. The results are presented in Table 3.5.

For the respective active channel, the signal attenuation is always less than 1 dB (see also Table 3.6 with data for only the active channels included). In all configurations the laser intensity at the inactive port is at least 27 dB smaller than the input level, providing a sufficient separation between the two channels of better than $10^{-2.7} \approx 0.002$, corresponding to a crosstalk extinction ratio of 1 : 500.

3.4.4 Bidirectionality

The laser light can traverse the optical switch in both directions, as the multiplexing of the active signal path is done in a bidirectional way. In order to verify this property, the data sets of the active channels in Table 3.5 can be reused as a bidirectionality test. As can be seen from the consolidated values in Table 3.6, the transmission is slightly higher when using the *Common* fibre as output. For connector ① the optical insertion loss is marginally smaller than for connector ② in both directions.

Input	Level (mW)	Switch state	Output	Level (mW)	Ratio	Attenuation (dB)
Common	4.2	Off	①	3.6	0.86	0.67
			②	0.0	0.00	—
	5.1	Off	①	4.2	0.82	0.84
		On	②	4.1	0.80	0.95
	4.08	Off	①	3.46	0.85	0.72
		On	②	3.38	0.83	0.82
①	4.08	Off	*Common*	3.67	0.90	0.46
			②	0.4×10^{-6}	0.00	70.1
		On	*Common*	7.7×10^{-3}	0.00	27.2
			②	2.4×10^{-6}	0.00	62.3
②	4.08	Off	*Common*	5.8×10^{-3}	0.00	28.5
			①	2.5×10^{-6}	0.00	62.1
		On	*Common*	3.47	0.85	0.70
			①	0.8×10^{-6}	0.00	67.1

Table 3.5: Optical insertion loss and crosstalk suppression of the measured fibre-optic switch (one-way).

Input	Level (mW)	Output	Level (mW)	Ratio	Attenuation (dB)
Common	4.2	①	3.6	0.86	0.67
	5.1		4.2	0.82	0.84
	4.08		3.46	0.85	0.72
①	4.08	*Common*	3.67	0.90	0.46

(a) Off-state.

Input	Level (mW)	Output	Level (mW)	Ratio	Attenuation (dB)
Common	5.1	②	4.1	0.80	0.95
	4.08		3.38	0.83	0.82
②	4.08	*Common*	3.47	0.85	0.70

(b) On-state.

Table 3.6: Bidirectionality test of the fibre-optic switch. Subset of data from Table 3.5 with only active channels shown.

3.4.5 Spectral Characteristics

The optical reference pulses provided by the laser-based synchronisation system have a central wavelength of $\lambda = 1550\,\text{nm}$. Accordingly, the employed fibre-optic switch has been chosen to operate at the same wavelength. Using a pulsed laser, the influence of the device on the spectrum of traversing light has been measured. In Figure 3.15, the results are plotted for laser pulses travelling through different ports of the switch in both directions in comparison with the spectrum of the incoming light.

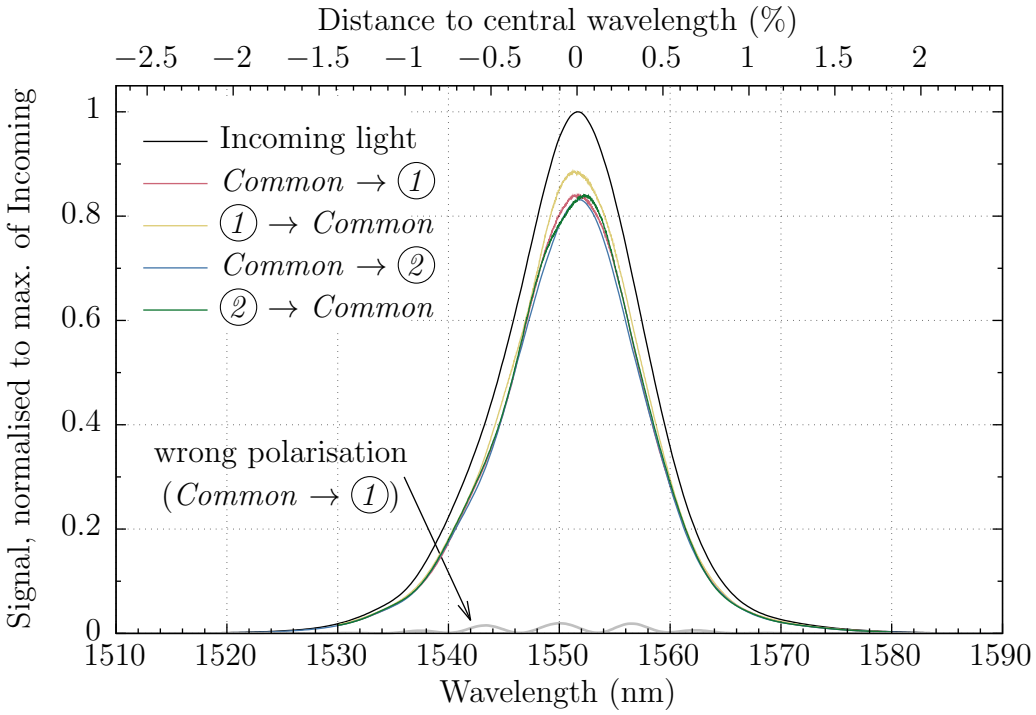

Figure 3.15: Influence of the fibre-optic switch on the spectrum of traversing laser pulses. Adapted from [DCG+15, p. 480].

The spectral shape including the line width is maintained while the signal amplitude is reduced by 10 % to 20 %. This is consistent with the measurements presented in Table 3.6. The observation that the direction ① → *Common* exhibits the least attenuation is reproduced as well. As can be seen from the trace at the very bottom of Figure 3.15 (marked with arrow 'wrong polarisation'), it is essential to use the device with the correct polarisation direction. If the incoming light is polarised along the wrong axis, the transmission drops drastically and the spectral shape is distorted.

3.5 Stability Estimations

For the measurement of bunch arrival times with femtosecond precision it is essential to prevent – or monitor and correct – any drifts of the detector system occurring at and above this time scale. In order to provide the necessary measurement stability and obtain consistent detector readings over longer periods of time, external environmental characteristics must be taken into account as well. Variables such as temperature and humidity can influence the physical properties of the employed materials, leading to behavioural changes of the respective subsystems. Table 3.7 lists the susceptibility of several components and materials used in signal transmission to timing changes caused by environmental influences.

Component	Dependency		References
	Temperature ($\mathrm{fs}/(\mathrm{K}\cdot\mathrm{m})$)	Humidity ($\mathrm{fs}/(\%_{\mathrm{RH}}\cdot\mathrm{m})$)	
RF cables			
Standard coaxial cable	$120\ldots220$	≈ 10	[Lam17, pp. 90–92]
Phase stable RF cable	$5\ldots50$	$2\ldots5$	
Optical fibres			
Standard optical fibre	$30\ldots130$	≈ 2.5	[BBF+12], [Bou11]
Phase stabilised optical fibre	$3\ldots5$	≈ 0.4	
Air at 25 °C and 100 kPa	-3	-0.04	[Pol17], [Cid96]

Table 3.7: Signal timing dependencies of RF cables, optical fibres and air on temperature and humidity changes.

As shown in section 3.2, two regions of the BAM electro-optical unit need to be distinguished regarding the stability of environmental properties: the 19-inch module housing the whole system and the actively temperature stabilised compartment ('thermo box') for sensitive components.

3.5.1 19-Inch Module

Table 3.8 lists the materials involved in the optical signal transport outside of the thermo box and their respective contribution to temperature-induced timing drifts. The total length of optical fibre between the thermo box and the collimators of the delay stages is approximately 5 cm per channel.[8] The free-space optical path on the ODL has a length

[8] The optical fibres transporting the clock and data output signals to the connectors on the front panel of the 19-inch module also run outside of the thermo box. However, they experience identical environmental drifts with the same resulting timing changes. In the readout electronics, the clock

Component	Length (m)	Sensitivity (fs/(K · m))	Contribution (fs/K)	Note
Optical fibre	0.05	40	2	^{i}
Free-space optical path (air)	0.3	−3	−1	^{d}
Free-space opt. path, projected on…				
…optics holder plate	0.2	77	15	^{i}
…ODL spindle	0.1	40	4	^{d}
Overall	—	—	20	^{d}

^{i}independent of motor position.
^{d}dependent on motor position.

Table 3.8: Contributions of materials outside of the thermo box to temperature-induced timing drifts (single-pass configuration, motor slide in central position).

of 30 cm if the single-pass configuration as defined on page 53 is used and the motor slide is in its centre position.

In addition to the change of the speed of light in air caused by temperature variations, the delay stage spindle and the optics holder plate experience thermal expansion. As a consequence, the distances between the components and therefore the optical path length change with temperature. The spindle is made of steel with a linear expansion coefficient of $\alpha_\mathrm{L} \approx 1.2 \times 10^{-5}/\mathrm{K}$, corresponding to a signal timing dependency of $\alpha_\mathrm{L}/c \approx 40\,\mathrm{fs}/(\mathrm{K}\cdot\mathrm{m})$. For the aluminium optics holder plate, the corresponding values are $\alpha_\mathrm{L} \approx 2.3 \times 10^{-5}/\mathrm{K}$ and $\alpha_\mathrm{L}/c \approx 77\,\mathrm{fs}/(\mathrm{K}\cdot\mathrm{m})$. Hence, the total systematic timing error caused by temperature changes is approximately 20 fs/K, dominated by the thermal expansion of the optics holder plate.

The electro-optical unit is installed in a 19-inch rack together with associated electronic components. The racks are actively temperature stabilised with a specified regulation precision of better than ±1 K [NLSH12, p. 4], resulting in a maximum expected temperature caused systematic error of ±20 fs. The casing of the 19-inch module acts as a low-pass filter reducing the speed of external changes. An additional potential source of timing drifts is the air pressure with a sensitivity of approximately $1\,\mathrm{fs}/(\mathrm{hPa}\cdot\mathrm{m})$ [Pol17][Cid96].

Given the known sensitivities of the individual materials, it would in principle be possible to take timing drifts caused by environmental changes into account in the subsequent data processing chain. This could be done with the help of real-time measurements of the respective quantities by the readout electronics or by the device server

signal is used as a trigger for the digitisation of the data channels and the timing changes cancel each other out.

processing the data for the accelerator control system. However, such a correction is currently not implemented.

3.5.2 Thermo Box

For increased protection and shielding from external disturbances, timing critical components which are sensitive to environmental effects are accommodated inside a separate compartment of the electro-optical unit (see section 3.2). This area is self-contained with active thermal and passive humidity stabilisation in order to reduce the influence of environmental changes. The temperature of this compartment is monitored and regulated with a digital controller acting on Peltier elements which are attached to the metallic base plate. The inner surface is lined with metal foil for humidity shielding. A sachet filled with silica gel is placed in the thermo box with the purpose of attenuating moisture fluctuations.

For the electro-optical unit of the existing BAMs at FLASH, the achieved temperature stability in the thermo box is approximately 10 mK (root mean square) over one hour [Boc12, p. 94]. This value is aimed for with the new design as well. During the course of this work, different temperature controllers have been set up and tested with respect to their suitability for this application. The response of the temperature stabilisation to external thermal changes has been measured in a climate chamber using the experimental setup shown in Figure 3.16. A step of $\Delta T_{\text{ext}} = 2\,\text{K}$ has been applied and the response of the temperature inside the actively stabilised casing has been recorded.

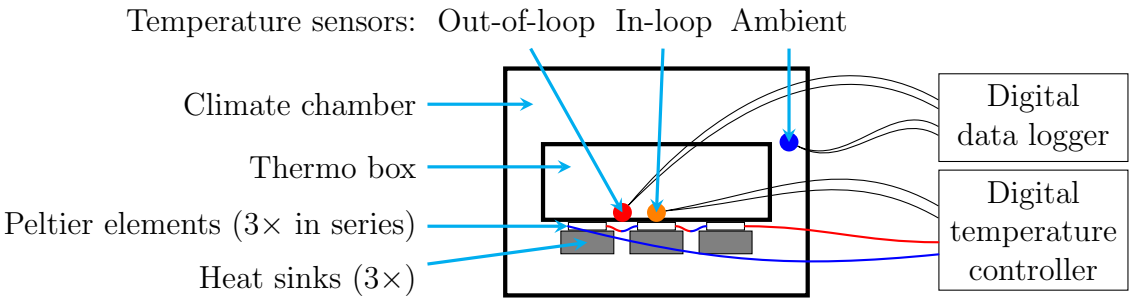

Figure 3.16: Climate chamber measurement setup.

The measurement results are presented in Figure 3.17. The shaded area indicates the time span needed by the climate chamber to reach the new target temperature. The standard deviations of both channels – ambient temperature and out-of-loop signal – have been computed from the data points before respectively after this adaptation time and are given in the plot as well. For better visibility, the secondary y axis indicating the temperature inside the thermo box uses a ten times finer resolution than the ambient temperature axis.

The external fluctuations are attenuated by a factor of more than 25 and the temperature step is compensated to a large extent. The residual change of the mean temperature

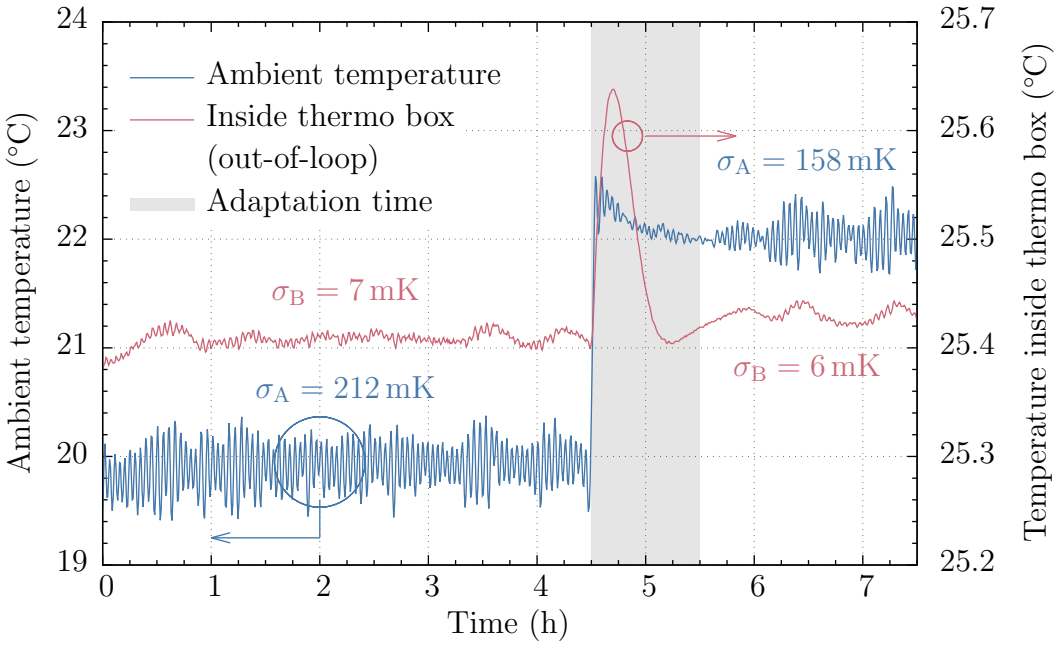

Figure 3.17: Temperature stability measurement in a climate chamber, applying a step to the ambient temperature. Temperature controller parameters not yet optimised.

inside the thermo box of about 0.01 K might be explained by the fact that the plot shows out-of-loop data. In addition, it must be noted that this measurement served as a very first test with the controller parameters not yet optimised, which explains the relatively large overshoot of 0.25 K during the step response. Using optimised settings, it is expected to achieve comparable or better results with a reduced overshoot behaviour in the final setup.

The employed digital temperature controller[9] has a specified regulation precision of better than 0.01 K [Mee]. This value is consistent with the achieved out-of-loop stability of 7 mK during the measurement shown in Figure 3.17. Therefore, the presented setup fulfils the requirement of limiting short-term temperature fluctuations inside the thermo box to below 10 mK (see page 62). The combination of an insulated chamber, Peltier elements and the chosen digital temperature controller is an eligible solution. The total length of optical fibre installed in the thermo box is approximately 2.5 m. Hence, the maximum expected timing drift contributed by this part is less than 1 fs.

Regarding humidity fluctuations, the dependencies of the employed polarisation-maintaining optical fibres and other components involved in signal processing are unknown and would need to be measured for a quantitative assessment. In standard optical fibre 1 $\%_{RH}$ change of the relative humidity causes a timing drift of approximately 2.5 fs/m

[9] Meerstetter TEC-1091

[Bou11]. For a total length of 2.5 m installed in the thermo box, this corresponds to a contribution of 6 fs/$\%_{\mathrm{RH}}$.

4 Bunch Compression Monitor for the European XFEL

At the European XFEL, bunch compression monitors (BCMs) are installed at four different locations along the accelerator (see page 31). Figure 4.1 shows a photograph of the station named '416.B2' located downstream the magnetic chicane of the third bunch compressor. The travel direction of the electron beam in this picture is from the bottom right to the top left.

The coherent diffraction radiation (CDR) is generated by a diffraction screen with a hole allowing for the electron beam to pass through. Screens with hole diameters of 5 mm and 7 mm (projected into the beam direction – see section 2.2.1) are mounted on a movable holder. It can be shifted in the vertical direction with the help of a motor

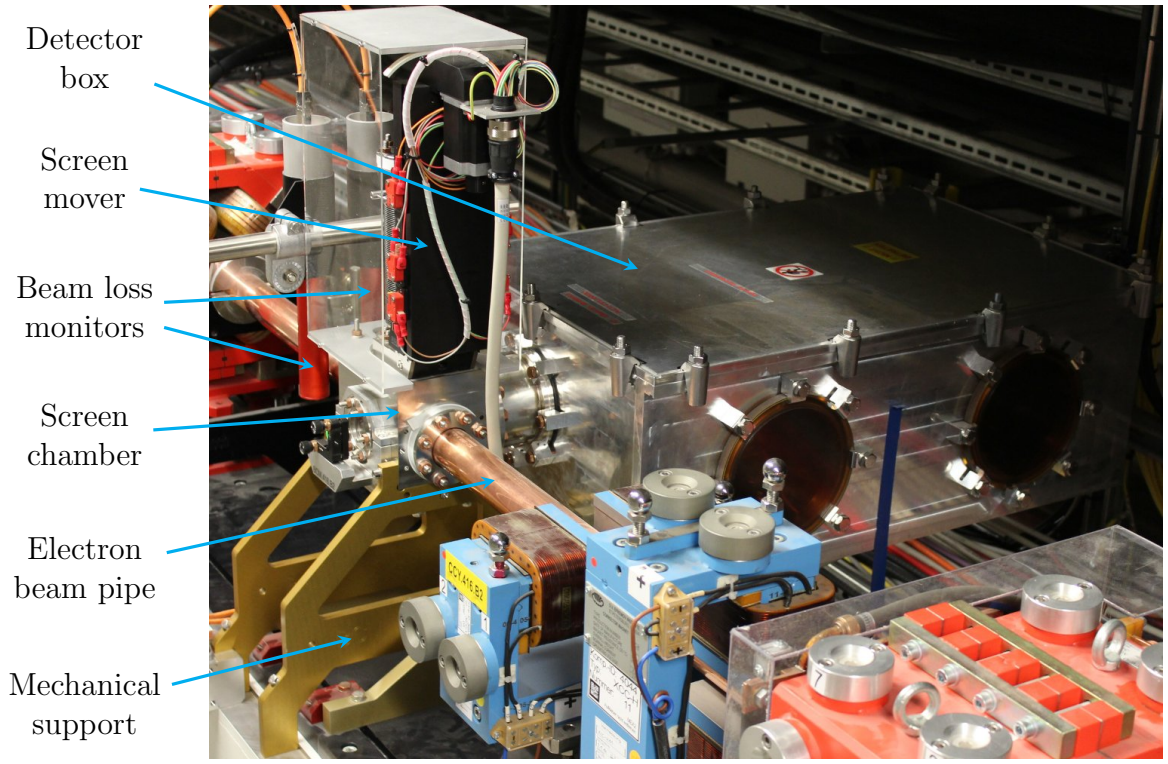

Figure 4.1: Photograph of a bunch compression monitor station installed at the European XFEL. Electron beam travel direction from bottom right to top left.

stage installed on top of the screen chamber.

The emitted diffraction radiation is guided through a vacuum window to the detector box located next to the electron beamline. On the opposite side of the screen chamber, a laser mount is available for the alignment of the CDR beam path. In order to detect particle losses and radiation emitted when electrons hit the diffraction screen, beam loss monitors are installed downstream the screen chamber on both sides of the vacuum pipe.

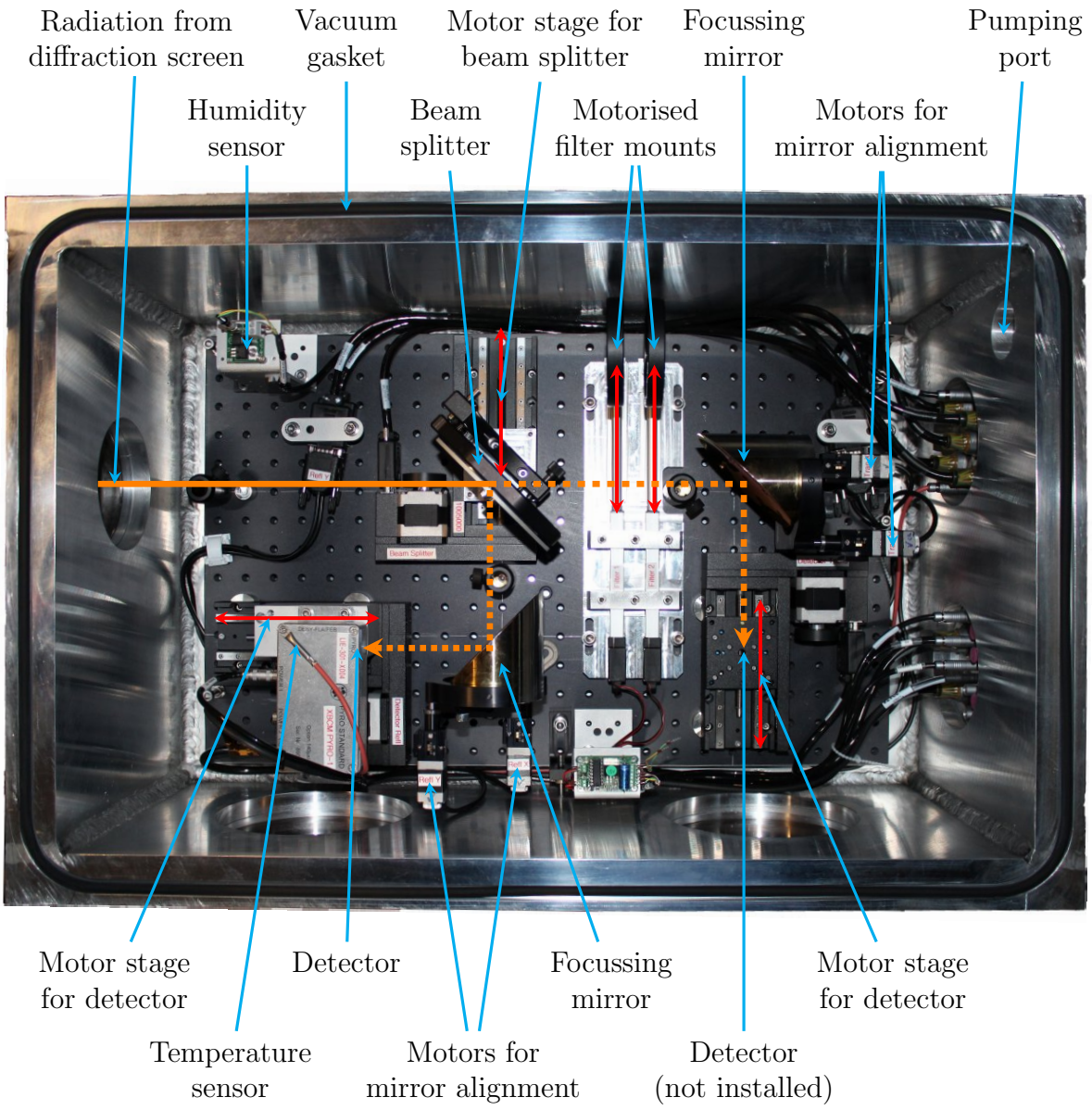

Figure 4.2: Components and signal path inside the BCM detector box. In this case, the second detector is not installed. Photograph courtesy of [Ger].

4.1 Radiation Transport to the Detector

Figure 4.2 shows a photograph of the components installed in the detector box with the CDR propagation path highlighted. In order to increase the sensitivity, two different detectors can be used depending on the signal intensity. A beam splitter mounted on a linear motor stage distributes the radiation to the detector locations. Two parabolic mirrors focus the beam to the active sensor area of each detector.

The detectors are mounted on linear motor stages allowing to change their distance to the CDR focal point. In this way, the signal level can be adjusted by varying the spot size on the sensor in order to prevent saturation. The focussing mirror mounts are motorised horizontally and vertically for steering the beam to the active sensor area. Optional wavelength-dependent filters can be inserted in one of the detector arms with the help of linear motor stages. They enable spectral shaping of the CDR in order to influence the sensitivity in certain wavelength ranges.

The detector box installed at the farthest downstream BCM station (named '416.B2', see Figure 2.7 on page 31) is operated under vacuum in order to prevent absorption of short CDR wavelengths by air. For this reason the upper edge of the detector box provides a notch for a vacuum gasket. At all other BCM stations, the detector boxes are operated under atmospheric pressure. However, they are likewise closed airtight in order to mechanically protect the components and avoid contaminations. Digital temperature and humidity sensors in the enclosed volume allow monitoring of the operating environment.

4.2 Spectral Intensity

As shown in section 2.2.1, the BCM signal is determined by

- the longitudinal form factor of the electron bunch (given by the bunch length, charge and current profile),
- the radiation generation at the CDR screen, including the hole size,
- the radiation transport (CDR beamline) and
- the detector response.

At the European XFEL, the bunch length varies significantly between the individual BCM stations due to the employed compression scheme. In addition, the charge choice affects the achievable final bunch length: lower-charge bunches can be compressed more due to smaller space charge forces. In Table 4.1, the design bunch lengths of the European XFEL are shown at all compression stages for different bunch charges. The CDR boundary frequencies and wavelengths are determined by the bunch lengths and thus span an equally wide range of values, as shown in Table 4.2.

Charge (pC)	Gun	BC0	BC1	BC2
	(fs rms)			
20	4500	1500	180	5
100	4800	1600	200	12
1000	6800	2200	300	84

Table 4.1: Design bunch lengths at the European XFEL [PDG14]. The values are given downstream the respective sections.

Charge (pC)	Gun	BC0	BC1	BC2
	(THz)			
20	0.22	0.67	5.6	200
100	0.21	0.63	5.0	83
1000	0.15	0.46	3.3	12

(a) CDR boundary frequencies.

Gun	BC0	BC1	BC2
(µm)			
1300	450	54	1.5
1400	480	60	3.6
2000	660	90	25

(b) CDR boundary wavelengths.

Table 4.2: Coherent diffraction radiation boundary frequencies and wavelengths for the BCM stations at the European XFEL. Computed from the values in Table 4.1.

As explained in [CSS05] and [Löh09], the spectrum of the emitted diffraction radiation is affected by the dimensions of the diffraction screen and the electron beam energy: the hole allowing for the electron beam to pass through leads to a strong suppression of short wavelengths. The boundary below which a significant reduction occurs decreases with increasing electron beam energy.

The influence of the beam energy and the diffraction screen hole diameter on the spectral intensity at the detector has been studied with the `THzTransport` software [CSS+09] for the first bunch compression monitor at the European XFEL. For this BCM, two installation locations are possible (see Figure 1.5 on page 16):

- in the diagnostics section between the magnetic chicane of the first bunch compressor (BC0) and the first main accelerating section (L1) or
- in the diagnostics section between L1 and the magnetic chicane of the second bunch compressor (BC1).

At both locations, the longitudinal bunch profile is identical: the acceleration in L1 only changes the particles' momentum, but not their longitudinal position in the bunch, as their velocity is already very close to the speed of light ($v \approx c$). L1 increases the beam energy from 130 MeV to 700 MeV.

The simulation results are shown in Figure 4.3. As expected, the spectral intensity is strongly increased for the higher beam energy. In addition, the spectrum extends

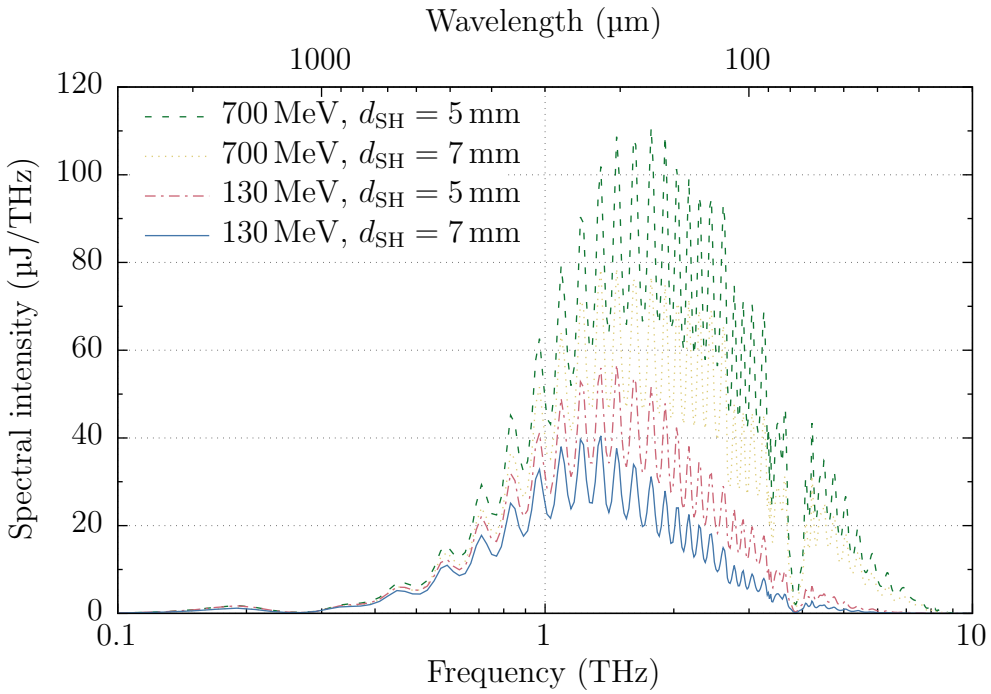

Figure 4.3: Simulation of the influence of the beam energy and the diffraction screen hole diameter (projected into the electron beam direction) on the spectral intensity at the detector for the first bunch compression monitor at the European XFEL.

farther towards short wavelengths. This is especially beneficial for the use in a bunch compression monitor as it increases the sensitivity of the detection system on coherent diffraction radiation whose boundary wavelength strongly depends on the bunch length and structure (see section 2.2.1). In this way, the measurement resolution for shorter bunches is improved. For this reason, the BCM for the first bunch compressor at the European XFEL is installed downstream L1.

For a fixed beam energy, a smaller diffraction screen hole size results in a higher spectral intensity. This however comes at the cost of an increased risk of hitting the screen with the electron beam, requiring careful steering and stable beam conditions. The smaller hole size can be beneficial for improving the measurement resolution when the BCM is used as a monitor in a beam-based feedback system during user runs. For setup and tuning of the accelerator, the use of a diffraction screen with a larger hole or its complete retraction from the electron beam path might be necessary. For this reason, the BCM stations at the European XFEL are equipped with motorised screen holders for remotely changing the used diffraction screen and adjusting its vertical position to the electron beam axis.

Due to spatial constraints, the lengths of the CDR transport lines at the European XFEL are slightly different among the individual stations. Furthermore, the farthest

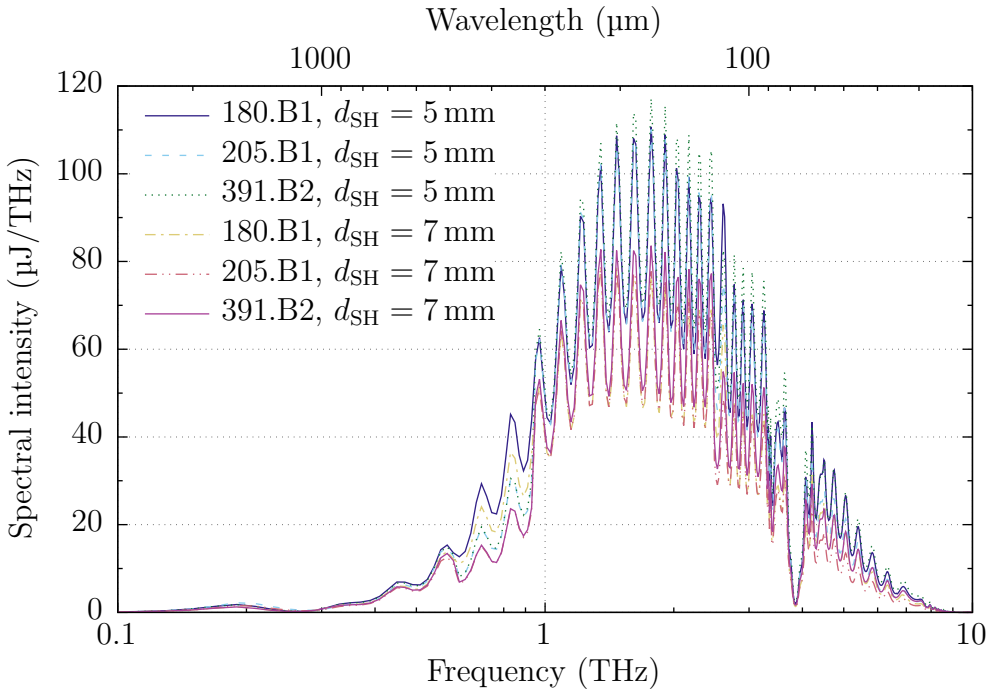

(a) First three stations.

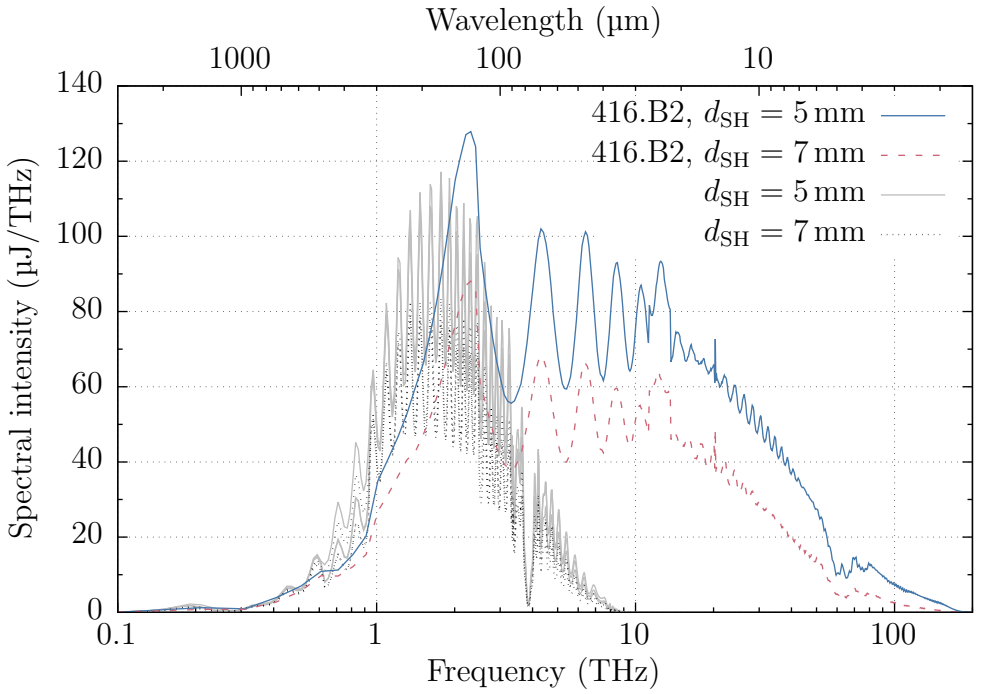

(b) Fourth station. First three stations in grey ($d_{SH} = 5\,mm$) and dotted black ($d_{SH} = 7\,mm$).

Figure 4.4: Simulation of the spectral intensity at the detector for the bunch compression monitors at the European XFEL with a bunch charge of 1 nC.

downstream BCM is equipped with a diamond window for coupling out the CDR from the accelerator vacuum (see section 4.1) as opposed to crystal quartz windows used at all other stations. It is thus necessary to simulate the spectral intensity at the detector separately for each station. This has been done with `THzTransport`, the results are shown in Figure 4.4.

The curves for the first three stations are very similar, both in spectral shape and intensity. The signal at the fourth station extends farther towards short wavelengths for the measurement of shorter bunches at the final compression stage. Again, the spectral intensity is higher for a smaller diffraction screen hole size. The data for all stations, including the different hole sizes, has been integrated into the BCM diagnostics module of `RF Tweak 5 GUI` for beam-based feedback simulations (see section 2.2 and section 5.1.1).

4.3 Detector Response

The single electron spectrum at the detector obtained from the `THzTransport` simulations comprises the second and third items in the list of constituents determining the BCM signal (see page 67): the radiation generation at the diffraction screen and the radiation transport to the detector (CDR beamline). For the description of the whole measurement chain, the spectral responsivity of the detector needs to be known as well. For the pyroelectric elements installed in the BCMs at FLASH and in one channel of each BCM at the European XFEL, the data available in [Wes12, p. 149] has been integrated into the BCM diagnostics module of `RF Tweak 5 GUI`.

4.4 Start-to-End Simulations

With all constituents determining the BCM signal (see page 67) known and available in the BCM diagnostics module of `RF Tweak 5 GUI`, start-to-end simulations for different detector locations are possible. This has been done for all three compression stages of the European XFEL. The used BCM locations are indicated by green dots in Figure 4.5. Additional studies on the influence of the accelerator working point on the BCM signal are presented in section 6.2 and section 7.3.

Figure 4.6 shows the phase space distribution of the electron bunch at the detector locations for the nominal accelerator working point with a bunch charge of 500 pC. The corresponding screenshots of the `RF Tweak 5` expert window display the signal constituents and the computed detector value at the respective station. The integrated detector signal in volts[1] is displayed on the top right of the panel. The shortening of the

[1]The BCM voltage readings have a negative polarity with a growing absolute value for increasing signal strength. This behaviour is emulated by the BCM diagnostics module of `RF Tweak 5 GUI`.

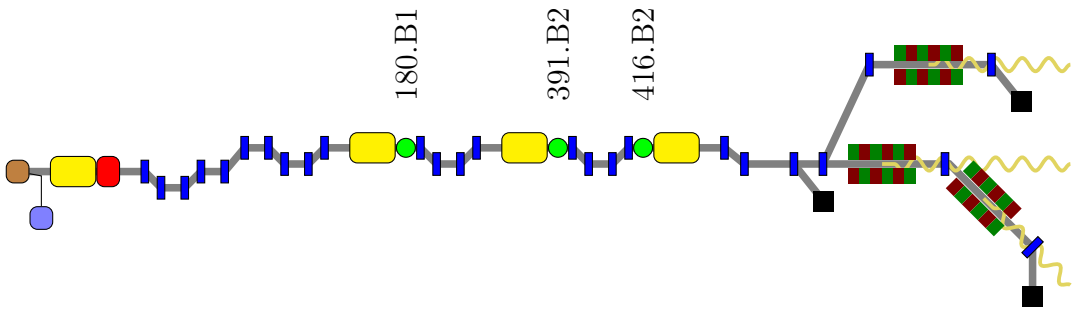

Figure 4.5: Locations and names of the BCM stations used for the start-to-end simulations at all three compression stages of the European XFEL.

bunch and the increase of the peak current and the BCM signal along the accelerator is clearly visible.

The dynamic range of the employed analogue-to-digital converter is 1.2 V. In Figure 4.6b and Figure 4.6c the displayed voltage reading exceeds this value, indicating that the signal would be clipped. For this reason, the detectors are mounted on linear motor stages allowing to change their distance to the CDR focal point (see section 4.1). In this way, the signal level can be adjusted by varying the spot size on the sensor in order to prevent saturation. The `RF Tweak 5 GUI` BCM expert window allows for multiplying the signal with a user-defined scaling factor[2] to emulate this functionality.

[2] referred to as 'fudge factor' in the panel.

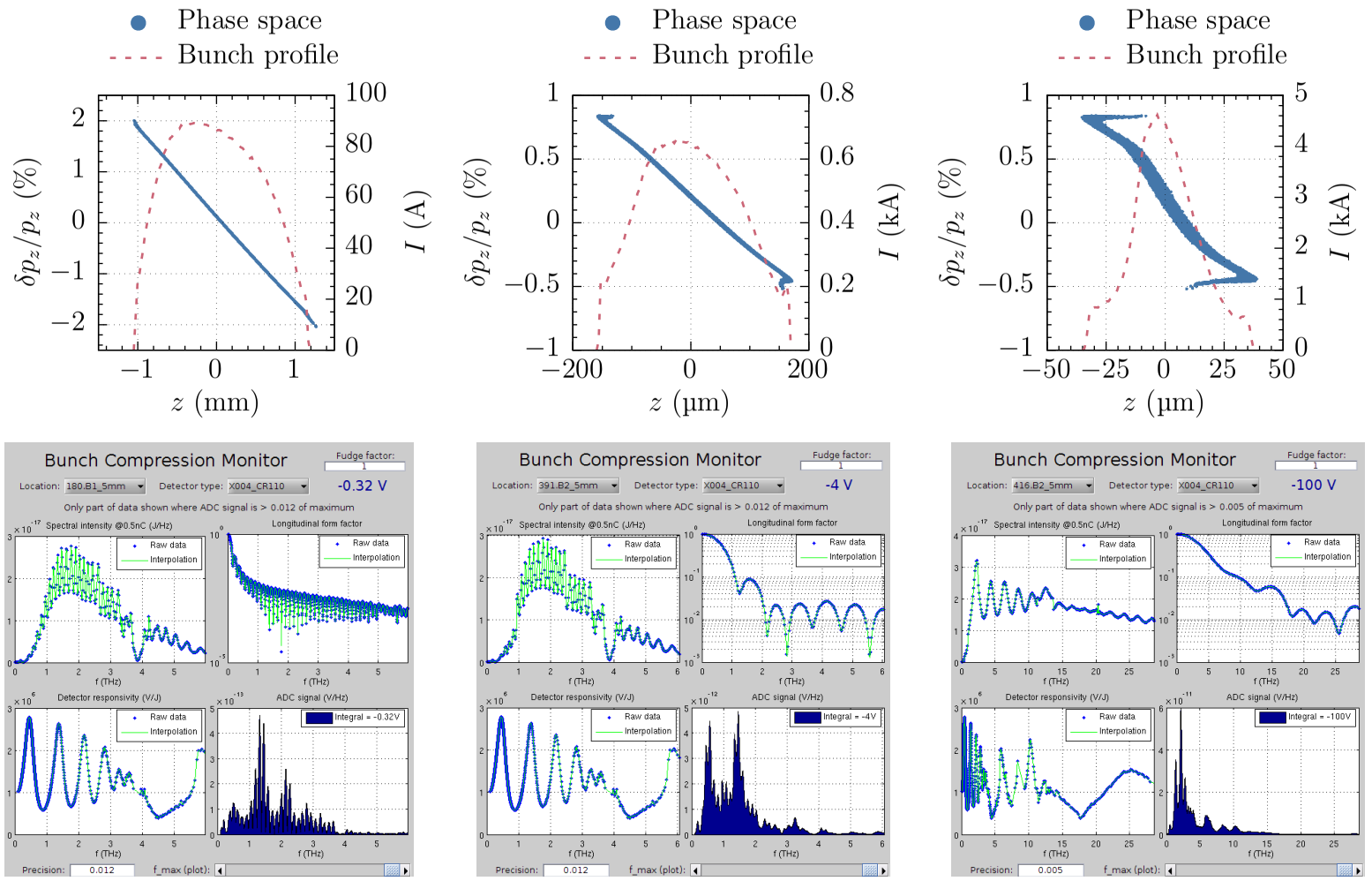

(a) 180.B1 (b) 391.B2 (c) 416.B2

Figure 4.6: Start-to-end simulation of the BCM signals for all compression stages at the European XFEL. Top row: phase space and bunch profile at the detector location. Bottom row: screenshot of the `RF Tweak 5` expert window displaying the signal constituents and the computed detector value for the respective station.

5 Beam-Based Feedback Simulations

Beam-based feedback (BBF) systems – as introduced in section 2.4 – make use of beam diagnostics and control elements along the accelerator in order to stabilise the machine working point over time by compensating drifts and reducing fast bunch-to-bunch jitter. For the evaluation and implementation of a feedback scheme which takes the not analytically describable electron beam dynamics into account, integration of beam transport simulations into the feedback considerations is necessary. In this chapter, the development of a simulation framework for the longitudinal beam-based intra bunch-train feedback at FLASH and the European XFEL, including beam dynamics simulations, is presented.

Within the scope of this work, only the longitudinal phase space is considered. It describes the correlation between

- the particle position, or timing, within the bunch and
- the particle energy, or relative energy deviation, with respect to a reference energy at the given longitudinal position of the accelerator lattice.

For measuring these values, different types of beam diagnostics can be used at FLASH and the European XFEL, which are located upstream of, in and downstream of the bunch compressor chicanes (see chapter 2):

- Bunch Arrival Time Monitors (BAMs),
- Bunch Compression Monitors (BCMs) and
- Synchrotron Radiation Monitors (SRMs).

With the presented beam-based feedback simulations framework, a means of evaluating the regulation scheme for the longitudinal beam-based intra bunch-train feedback at FLASH and the European XFEL, taking the not analytically describable electron beam dynamics into account, is provided. Elements considered in the simulations include

- a model for the low-level radio frequency (LLRF) controllers and plants,
- a timing scheme based on discrete time steps describing the bunch train pattern with respect to the LLRF control loop execution time and
- the possibility to introduce individual delays caused by the feedback execution time as well as the physical distances between the LLRF stations and the beam diagnostics monitors.

The BBF simulations framework has been developed for the purpose of studying fast intra bunch-train feedback. It is nonetheless equally well suited for the description of slower feedback schemes acting for example from macropulse to macropulse. The time structure and bunch pattern can be defined by choosing an appropriate timing scheme for the simulations (see section 5.3.2).

5.1 Simulations Framework

The BBF simulations framework is constructed on the basis of the longitudinal particle tracking software `RF Tweak 5` described in section 1.4.1. Making use of an existing tracking code allows for the framework development to focus on the implementation of the feedback part of the system. The `RF Tweak 5` core is used for the accelerator lattice set-up and particle tracking. Its graphical user interface (GUI) is not needed, yet undisturbing, for this task.

As a link to the BBF simulations framework, an interstage compatibility layer has been attached to the `RF Tweak 5` core. It provides a clearly defined application programming interface (API) for accessing the relevant data fields (e.g. RF settings and tracking results), without needing to know the internal structures of the `RF Tweak 5` core. This implementation allows for the integration of the genuine `RF Tweak 5` code, which is developed and maintained independently. When the internal structure of `RF Tweak 5` changes, only the compatibility layer must be adjusted accordingly. Code using the framework does not need to be changed, because the provided API stays fixed.

For compatibility with `RF Tweak 5`, the BBF framework is implemented in the MATLAB programming language. In order to facilitate the maintainability and expandability, the extension of the existing `RF Tweak 5` code is done in a modular way. The individual components and their relations are shown in Figure 5.1.

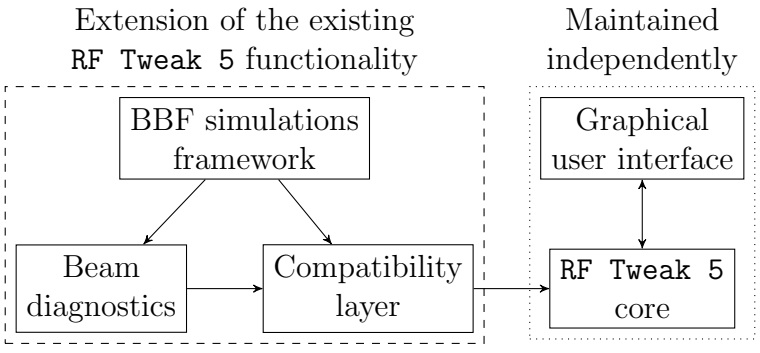

Figure 5.1: Structuring principle of the BBF simulations subcomponents and integration with the existing `RF Tweak 5` software. The arrows indicate the direction of access.

The compatibility layer provides access to the `RF Tweak 5` internal data structures and handles the communication between the `RF Tweak 5` core and the BBF simulations framework. Its tasks comprise

- preparation of the internal workspace of `RF Tweak 5` and initialisation of the API,
- storing and updating the RF settings in `RF Tweak 5` and
- triggering the particle tracking and retrieving the tracking results, i.e. the particle distributions and longitudinal beam current profiles at the individual accelerator sections.

The BBF simulations framework utilises the compatibility layer for changing the RF settings and initiating the particle tracking. It then resorts to the beam diagnostics elements for updating the detector readings. The beam diagnostics in turn query the compatibility layer for the tracking results from which the measurement values are computed.

5.1.1 Beam Diagnostics Elements

In accordance with the motivation given on page 75, beam diagnostics elements which are suited for longitudinal intra bunch-train feedback have been implemented. Due to the modular design of the framework, additional types can be added easily. Currently, the following components are available:

Ideal BAM

This module implements a bunch arrival time monitor (see section 2.1) with perfect resolution. The bunch arrival time is obtained from the centre of gravity of the longitudinal particle distribution at the detector location. The computed measurement value exhibits no jitter, drift or charge dependence. If desired, those contributions can be added to the signal later in the processing chain.

Ideal BCM

This module implements a bunch compression monitor (see section 2.2) with perfect resolution. The measurement signal is obtained by calculating the longitudinal form factor from the beam current profile at the detector location. This value is then squared, multiplied by the transverse form factor and radiation transport beamline characteristics (stored in combined single electron spectrum data files calculated with `THzTransport`) and multiplied by the detector responsivity obtained from the data sheet or dedicated measurements.

Single electron spectrum data files are available for FLASH (locations 4DBC3.1, 4DBC3.2, 9DBC2.1 and 9DBC2.2, see Figure 2.8) and the European XFEL (locations 180.B1, 205.B1, 391.B2 and 416.B2, see Figure 2.7; for 7 mm and 5 mm diffraction screen hole diameter, each). The computed measurement value exhibits no jitter or drift. If desired, those contributions can be added to the signal later in the processing chain.

Infinite Resolution SRM Camera

This module implements a synchrotron radiation monitor (see section 2.3) with infinite resolution. *Infinite resolution* refers to a hypothetical device with infinite size (no boundaries) and an infinite number of infinitesimally small pixels. The measured value is the transverse particle displacement in the centre of a C-type bunch compressor. It is obtained by multiplying the energy deviation by the R_{16} of the first half of the magnetic chicane. The computed measurement value exhibits no jitter or drift. If desired, those contributions can be added to the signal later in the processing chain.

Finite Resolution SRM Camera

This module implements a realistic synchrotron radiation monitor. The measurement signal is obtained by using the output of an infinite resolution SRM camera and binning the data according to the sensor geometry and size. Like for the infinite resolution SRM camera, the computed measurement value exhibits no jitter or drift. If desired, those contributions can be added to the signal later in the processing chain.

5.1.2 Auxiliary Components

In addition to the beam diagnostics elements, further modules are included for the implementation and evaluation of the BBF scheme. Currently, the following components are available:

RF Tweak 5 Wrapper

This is the compatibility layer built around an internal script of `RF Tweak 5` for setting up the tracking simulation and preparing the API access. The initialisation steps include the creation of a default energy profile and loading the input particle distribution for the selected bunch charge and energy profile from a file. In addition, the internal data structures and variables needed for further calls to `RF Tweak 5` – for changing the RF settings, initiating particle tracking and reading the tracking results – are prepared and managed by this module.

Transfer Function

This is a container class used for storing a transfer function G defined by the numerator and denominator coefficients (roots and poles), including plausibility checks. The output signal y is computed from the input signal u via $y = G \times u$.

Transfer Function Import Wrapper

This function provides the conversion of LLRF system measurements or model data into a `TransferFunction` class instance for use by the Transfer Function building block (see section 5.2).

ACC1 Cavity Model

This data set provides a multiple input, multiple output (MIMO) system describing a measured cavity model for the first accelerating module at FLASH. It enables taking the realistic behaviour of the accelerating cavities into account in the simulations.

5.2 Building Blocks

The BBF simulations system is constructed in a modular way based on discrete building blocks and signals. Building blocks transform input signals to output signals. In turn, signals interconnect building blocks. Thus a network is constructed. The building blocks and signals are implemented as MATLAB classes, using an object-oriented structure with focus on functionality encapsulation and data exchange via defined interfaces.

The modular and flexible structure makes the system easily extendible, for instance in order to implement new building block types or more complex signals. Furthermore, it enables reusing individual components for other purposes, such as the `RF Tweak 5 GUI` beam diagnostics expert windows described in section 5.5. Additionally, it facilitates the automated generation of block diagrams as a visual representation of the defined system (see section 5.4). The figures included in this section have been created using this functionality.

The following components are available for constructing the system:

Signal

Signals transfer information between building blocks. This module is a wrapper for handling data exchange by providing a shared, pointer-like access to a variable. State changes are communicated between multiple building blocks by reading from or writing to the same signal. Scalar, vector (bus-like) and structured data types are supported.

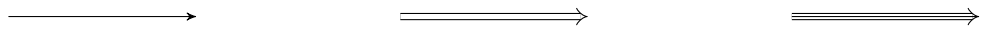

(a) Scalar. (b) Pair (e.g. A, Φ or I, Q). (c) Vector or structured data.

Figure 5.2: Signal widths implemented in the BBF framework and corresponding graphical representations.

The data values are stored in a history buffer of configurable length, which is shifted by one field with each clock cycle (first in, first out). This scheme provides implicit zero-order hold functionality: the new field is initialised with the value of the field which was the newest one before shifting. If no new data is provided, the signal value stays unchanged. Alternatively, a signal can be initialised with pre-filled history values. In this case, a circular buffer is used instead of the zero-order hold functionality.

Building Block

In order to ensure the compatibility of all building blocks with the *signals and building blocks* scheme described in the beginning of this section, all components must exhibit the same interface. This is achieved by defining an abstract base class which describes the infrastructure every building block must provide: input signals, output signals and a method for the transformation calculation. All building blocks are derived from this base class and share this interface.

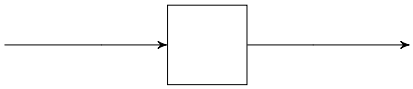

Figure 5.3: Symbol for a generic building block (in this case with one input signal and one output signal).

Constant Signal Source (Step Function)

This building block outputs a constant value. It has zero input signals and one output signal. By combining this block with a signal whose initial value is different from the seed of the constant output, a step function is implemented.

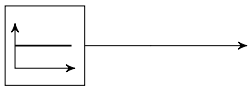

Figure 5.4: Symbol for a constant source block.

Combination (Subtraction, Amplifier, Attenuator, Bus Manipulation)

This building block sums multiple input signals without latency. It works with an arbitrary number (at least one) of input signals and combines them to one output signal, without time delay. The inputs can be given individual weighting factors in the summation.

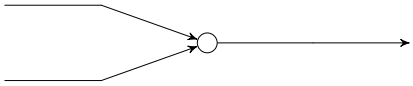

Figure 5.5: Symbol for a combination block (in this case with two input signals).

By choosing suitable values for the weighting factors of the individual input signals, further functionalities can be realised. With negative coefficient(s), subtraction is achieved. By using this block with one input and one output, an amplifier (coefficient greater than 1) or attenuator (coefficient less than 1) is realised.

An additional application of this building block is the manipulation of signal widths. Vector signals can be constructed from multiple inputs by using specific weighting matrices. In the same way, vector inputs can be decomposed into multiple output signals.

Summation (Subtraction, Amplifier, Attenuator, Bus Manipulation)

This building block performs a combination with an additional delay of one discrete time step. It is derived from the combination class and therefore offers the same use cases and possibilities. Like the combination, it supports individual weighting factors for the input signals, which allows for realising subtractions, amplifiers, attenuators and signal width manipulations.

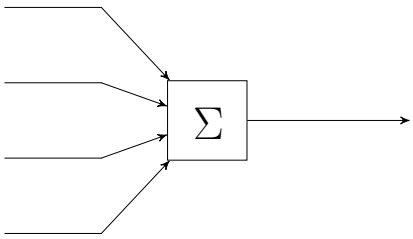

Figure 5.6: Symbol for a summation block (in this case with four input signals).

Delay

This building block introduces a time delay in a signal. It has one input and one output. The output signal is delayed with respect to the input signal by a configurable number of discrete time steps (default value: 1).

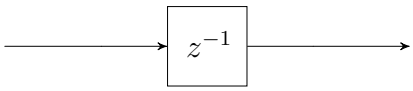

Figure 5.7: Symbol for a delay block (in this case of one time step).

Multiplexer

This abstract class adds a functionality to building blocks to access single columns of vector signals (inputs and outputs) as individual signals. In this way, the inputs and outputs either can be provided as single signals or as bus-like vector signals. The multiplexing capability is enabled for a building block by deriving it from this helper class.

Transfer Function

This building block implements a multiple input, multiple output (MIMO) system defined by a matrix of transfer functions. For each pair of input and output signals, one specific entry in the transfer functions matrix is used. Multiplexing is supported for input and output signals.

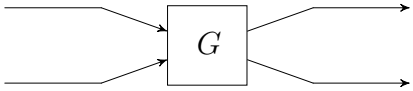

Figure 5.8: Symbol for a transfer function block (in this case a MIMO system with two inputs and two outputs).

Conversion $(A, \Phi) \leftrightarrow (I, Q)$

These building blocks perform conversions of signals between the (Amplitude, Phase) and $(I,\ Q)$ representations according to $I = A\cos(\Phi)$ and $Q = A\sin(\Phi)$. The two conversion directions are implemented as separate building blocks. The vector components are defined as scalar signals, therefore these building blocks have two inputs and two outputs each.

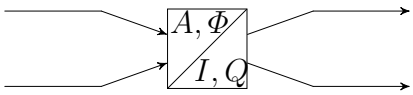

(a) $(A, \Phi) \rightarrow (I, Q)$ conversion.

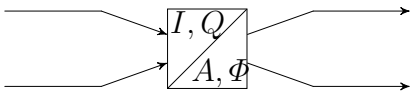

(b) $(I, Q) \rightarrow (A, \Phi)$ conversion.

Figure 5.9: Vector conversion blocks implemented in the BBF framework and corresponding graphical representations.

RF Tweak

This building block encapsulates the `RF Tweak 5` compatibility layer described in section 5.1. It marks the interface between the BBF simulations code and the `RF Tweak 5` core. The input signals are the set points of the accelerating modules in units of amplitude and phase, with multiplexer capability. Their number depends on the simulated accelerator (4 for FLASH, 5 for the European XFEL). Due to validity limitations of the employed 2D tracking model in the non-ultrarelativistic regime, the RF gun set point is not available as an input (see section 1.4.1). The output signals are obtained by particle tracking with `RF Tweak 5`. This building block has two outputs corresponding to two `RF Tweak 5` data structures, named `trackout` and `wakedata`, which contain the tracking results.

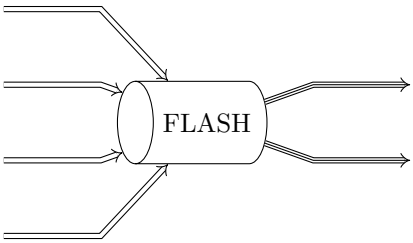

Figure 5.10: Symbol for an accelerator interface function block (in this case FLASH; the four input vectors correspond to the RF set points of the four accelerating stations: ACC1, ACC39, ACC23 and ACC4567; cf. section 1.2).

RF Tweak BAM

This building block implements a bunch arrival time monitor. It is a wrapper class providing an interface from the `RF Tweak 5` API to the 'Ideal BAM' detector type described on page 77. Its single input signal is the `RF Tweak 5` data structure `trackout`, its single output signal is the bunch arrival time in seconds[1]. The calculations are performed in the corresponding detector class.

[1] If the desired output unit is pico- or femtoseconds, a Combination block configured as an amplifier with a scaling factor of 10^{12} or 10^{15} can be connected to the BAM output.

5.3 Control Loops

A BBF system is defined by a network of building blocks and signals, as described in section 5.2. State updates of individual components are triggered by calling the `DoStep` method of the respective class. This function executes the transformation calculations of building blocks in order to compute the output signals from the input signals. For signals, it performs the history buffer shifting.

During the simulation of a BBF network, the states of all elements need to be updated synchronously, conforming to a common clock. In order to facilitate the correct timing and synchronisation of all components, the BBF simulations framework provides a global `Simulation` wrapper class. It maintains a list of all signals and building blocks present in the system and triggers the state updates of the simulation components in the correct order. By this means, a common clock for all elements is established. In addition, multiple clocks with different repetition rates for more differentiated timing schemes (see section 5.3.2) are supported.

5.3.1 Bunch Train

In order to simulate beam-based intra bunch-train feedback, a method for handling multiple bunches is needed. The employed principle is shown in Figure 5.11. For each clock cycle, the LLRF block is executed. Its output signals define the RF settings for the particle tracking with `RF Tweak`. From the tracking results, the detector readings are computed and fed to the BBF subsystem. Its output signal is then used to adjust the LLRF settings for the next clock cycle. When no bunch is present, the particle tracking and beam diagnostics path is bypassed (dashed line, see section 5.3.2).

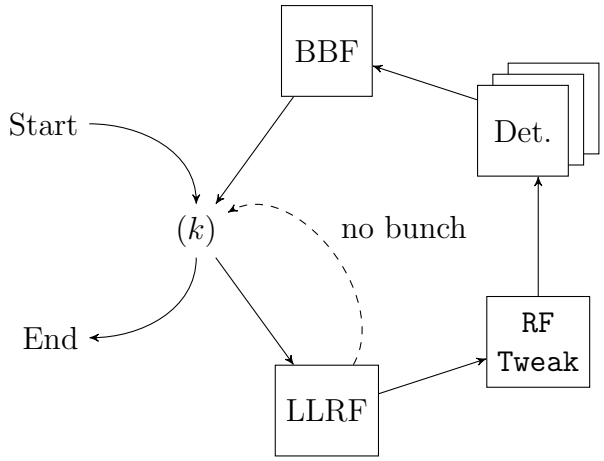

Figure 5.11: Beam-based intra bunch-train feedback processing cycle. The LLRF block is always executed, the feedback chain only when a bunch is present.

5.3.2 Timing Scheme

At FLASH and the European XFEL, the LLRF controller operates at a rate of $f_{\mathrm{LLRF}} = 9\,\mathrm{MHz}$. The bunches within a bunch train however have a lower repetition frequency of

- $f_{\mathrm{B}} = f_{\mathrm{LLRF}}/(9n)$ with $n \in \mathbb{N}$, hence $f_{\mathrm{B}} \leq 1\,\mathrm{MHz}$, at FLASH (see section 1.2) and
- $f_{\mathrm{B}} = f_{\mathrm{LLRF}}/n$ with $n \in \mathbb{N}, n \geq 2$, hence $f_{\mathrm{B}} \leq 4.5\,\mathrm{MHz}$, at the European XFEL (see section 1.3).

Consequently, electron bunches are present only for some LLRF execution cycles.

The computing time for one `RF Tweak 5` tracking run lies in the range of a few seconds.[2] This value exceeds the execution time of the other BBF simulation components by more than an order of magnitude. It is therefore desirable to only perform the full tracking and beam diagnostics chain if a bunch is present, in order to minimise the overall simulation time. For this reason, one of the objectives for the development of the BBF simulations framework was the support of a timing scheme describing the bunch train pattern with respect to the LLRF control loop execution time (see page 75).

In order to enable differentiated timing schemes, the `Simulation` wrapper class supports multiple clocks by enabling individual clock divisors for building blocks. Each block is only executed when the current clock cycle matches its clock divisor. Figure 5.12 illustrates the clock distribution scheme for the BBF simulations using this functionality. The employed principle is as follows:

- run the LLRF controller at $f_{\mathrm{LLRF}} = 9\,\mathrm{MHz}$,
- run `RF Tweak` and the beam diagnostics only when a bunch is present,
- hold the detector readings between bunches: zero-order hold (ZOH) functionality included in the `Signal` class and
- delay (z^{-n}) the detector signals by multiples of f_{LLRF}^{-1} ($\approx 111\,\mathrm{ns}$, $\approx 33\,\mathrm{m}$ in vacuum, $\approx 22\,\mathrm{m}$ in RF cables and optical fibre) to simulate
  - the physical distances between the LLRF stations and the beam diagnostics monitors as well as
  - the feedback execution time,
  - using individual delay settings for different beam diagnostics and LLRF stations depending on their location.

[2] For this reason bunch-resolved live tracking with `RF Tweak` is not feasible. This does however not conflict with the intended use of the BBF simulations framework for the design and study of fast intra bunch-train feedback systems operating on a microsecond time scale: the stages of development involving `RF Tweak` can be done offline and are therefore not time-critical. Once the feedback design is finalised, it can be integrated into the LLRF controller firmware for fast intra bunch-train regulation.

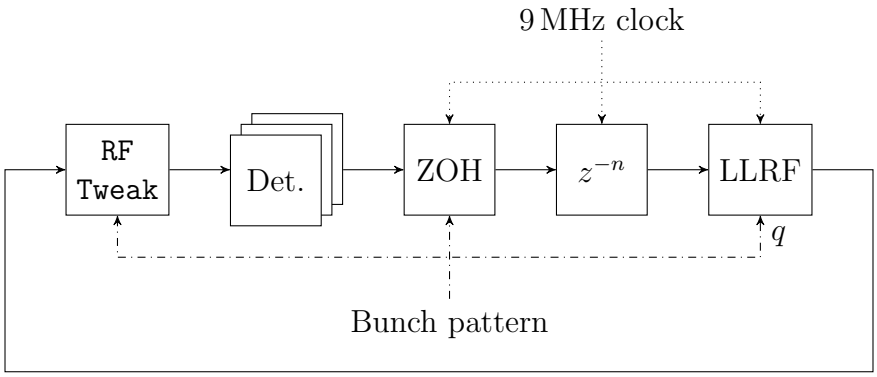

Figure 5.12: Signal processing chain and clock distribution scheme for the BBF simulations. q denotes an optional single-bunch charge measurement which can be used by the beam loading compensation algorithm integrated in the LLRF controller (see section 5.3.3).

By choosing appropriate clock divisors this timing scheme also allows for the description of slower feedback schemes acting for example from macropulse to macropulse.

5.3.3 LLRF and BBF Model of a Single RF Station

Figure 5.13 illustrates the implementation of an RF station with the complete BBF chain using this framework. It is based on Figure 2.12 with the addition of signal disturbance sources. The building blocks and signals describing the LLRF system are drawn in black, the BBF components in blue.

The LLRF controller is implemented using a small signal model (SSM) operating around a reference value of zero. The actual set point as well as an optional slope over the bunch train are added to the SSM output via combination blocks. This scheme eliminates the working point dependency of the LLRF control parameters.

The SSM loop contains the matrix $\mathbf{M}$ for combining the field and beam errors (c.f. section 2.4), the controller $\mathbf{C}$ and the plant $\mathbf{G}$. Signal disturbance sources – describing transmission, measurement and conversion noise – are located at the input and output ports of the plant building block as well as in the return branch feeding back the field measurements to the SSM input. A delay block represents the loop latency.

Inside the LLRF controller, the signals are represented in in-phase/quadrature (I, Q) form. The user interface and the `RF Tweak` simulations however use the amplitude/phase (A, Φ) notation. Interposed building blocks carry out the necessary conversions between the different data representations.

An `RF Tweak` instance computes the longitudinal particle phase space at the different detector locations from the LLRF signals. Subsequently, the detector readings – such as the bunch arrival time, compression and beam energy – are calculated with the help of

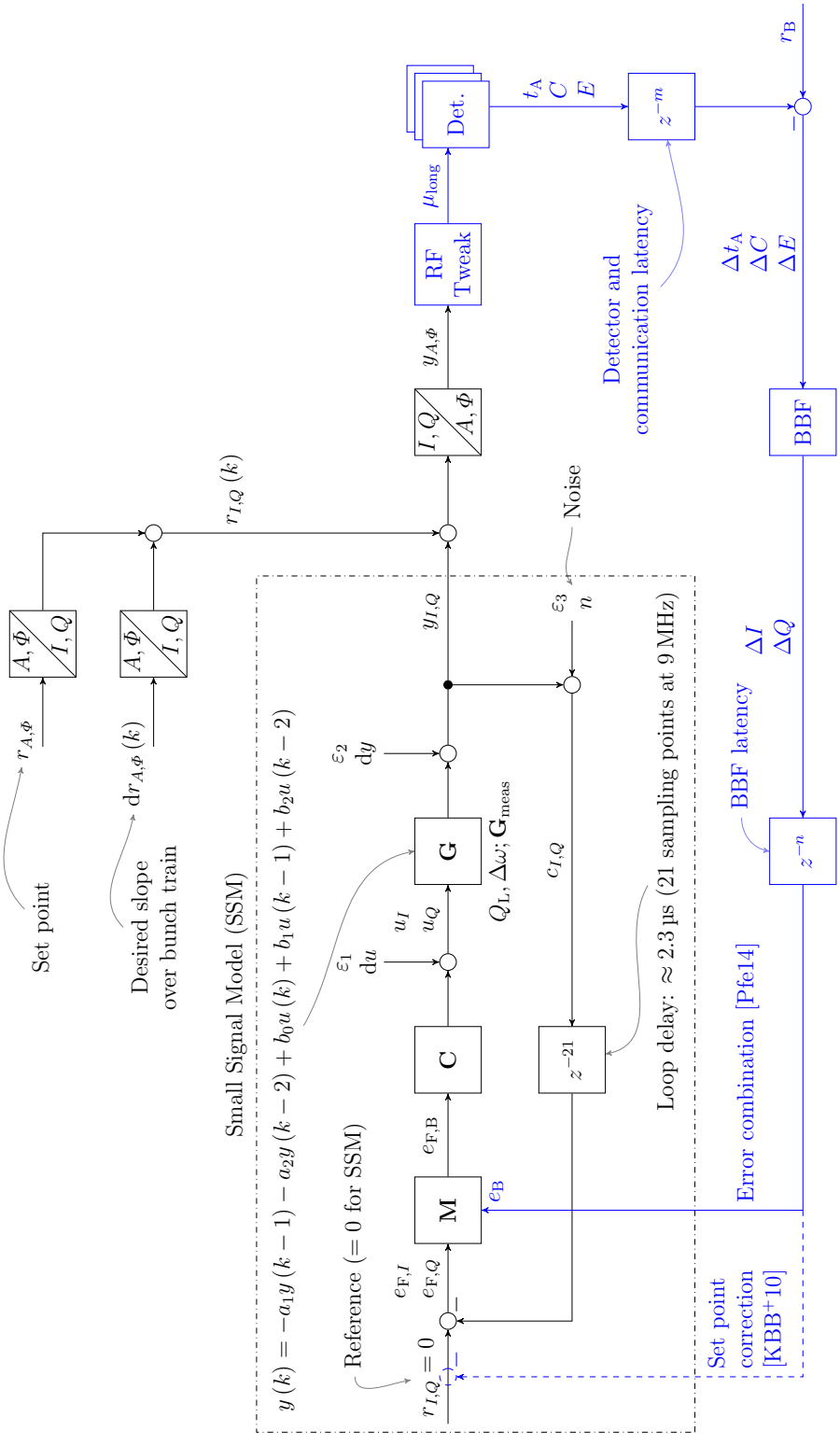

Figure 5.13: LLRF system structure with BBF. BBF components are drawn in blue. The path labelled 'Error combination' is used as opposed to 'Set point correction', because it has shown better performance [Pfe14].

the respective building blocks. The detection and communication latency is described by a delay block connected to the detector outputs.

The measured quantities are compared to user-specified reference values and the difference signals transferred to the BBF building block. Here, the deviations are translated into the necessary corrections of the LLRF signals. After passing a delay block representing the latency of the BBF computations, the data is fed back to the LLRF controller.

Figure 5.14 shows a summary of the LLRF controller's interface. Its input signals are the amplitude and phase reference $r_{A,\Phi}$ – optionally with a time-dependent slope $\mathrm{d}r_{A,\Phi}(k)$ over the bunch train – as well as the signal disturbance sources $\mathrm{d}u(k)$, $\mathrm{d}y(k)$ and $n(k)$. In addition, the global simulation clock and the beam error $e_{\mathrm{B}}(k)$ from the BBF are fed to the system. An optional time-dependent charge measurement $q(k)$ can be used by the beam loading compensation (BLC) algorithm integrated in the LLRF controller.

The single output signal describes the amplitude and phase values of the governed accelerating section. By using multiple LLRF stations in parallel as `RF Tweak` input (corresponding to the physical layout of the facility), the complete accelerator can be simulated with BBF.

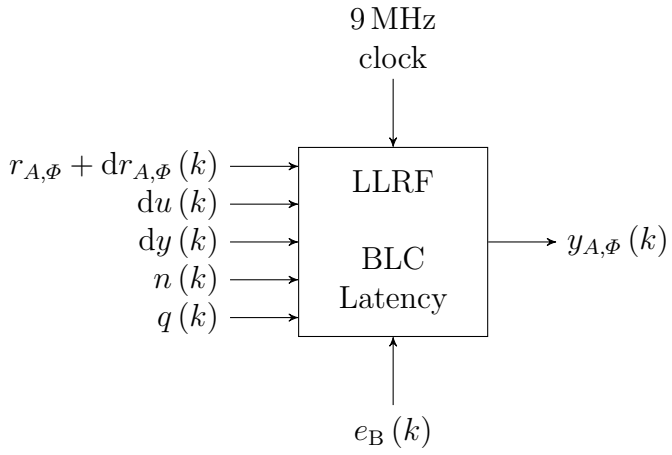

Figure 5.14: LLRF building block.

5.4 Automated Block Diagram Generation

From the building blocks and signals used for a BBF simulation within the scope of this framework, a block diagram displaying the relations between the individual components can be created automatically. This option allows for the verification and debugging of the system under investigation by visual inspection. The figures in section 5.2 have been generated with this functionality.

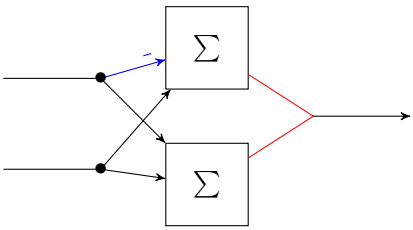

Figure 5.15: Subtraction and collision detection (outputs of both summation blocks writing to the same signal).

A block diagram is created by parsing the list of components as a directed graph: building blocks correspond to nodes, signals to edges. The list of signals is automatically generated from the list of building blocks to use. Signals not connected to any building block are hidden in the diagram for increased clarity.

Non-scalar signals are indicated via bus-like double (for vectors with width 2) or triple (for vectors with width > 2 and structured data types) arrows as shown in Figure 5.2. Collisions – meaning multiple building blocks writing to the same signal – are detected and indicated via red edges. Subtractions (weighting factor -1 in combinations or summations) are indicated via blue edges and a minus sign placed next to the end of the subtrahend edge. An example of the latter two cases is shown in Figure 5.15. Optionally, building blocks and signals can be annotated with node and edge labels.

Automated collision-free positioning of the nodes is achieved with the help of the *TikZ graph drawing* library [Tan13]. Currently the output formats Ti*k*Z, LaTeX and PDF are supported. Due to the modular design of the block diagram generation functionality, the system is easily extendible to support additional output formats.

5.5 Diagnostics Monitors Expert Windows for RF Tweak 5 GUI

In section 2.2.3 and section 2.3.2, the `RF Tweak 5 GUI` beam diagnostics expert windows for the bunch compression and synchrotron radiation monitors have been introduced. For the sake of maintainability and expandability, a proper encapsulation and separation of the associated program logic blocks has been a major design goal during their development which took place in the course of this work. The detector classes carrying out the beam-based measurements and the expert windows displaying the signals as well as controlling the detector properties are implemented as separate components, independent of the particle tracking code. Well-defined interfaces govern the data exchange and event notifications.

The employed partitioning scheme is illustrated in Figure 5.16. Updates of the diagnostics panels are not handled by the `RF Tweak 5 GUI` itself, but by an interstage supervisor class managing a list of currently open expert windows. It is informed by

the main program about particle tracking events or other state changes and schedules the re-computation of measurement values as well as display updates of the according quantities. For the calculation of the detector readings, the expert panels make use of the beam diagnostics classes described in section 5.1.1 included in the BBF simulations framework. By this separation principle, all expert GUIs and their internal data structures are independent of the main `RF Tweak 5 GUI` window and of any other expert windows, even ones of the same type. Thus, as many instances of each diagnostics panel as desired can be opened and operated independently at the same time.

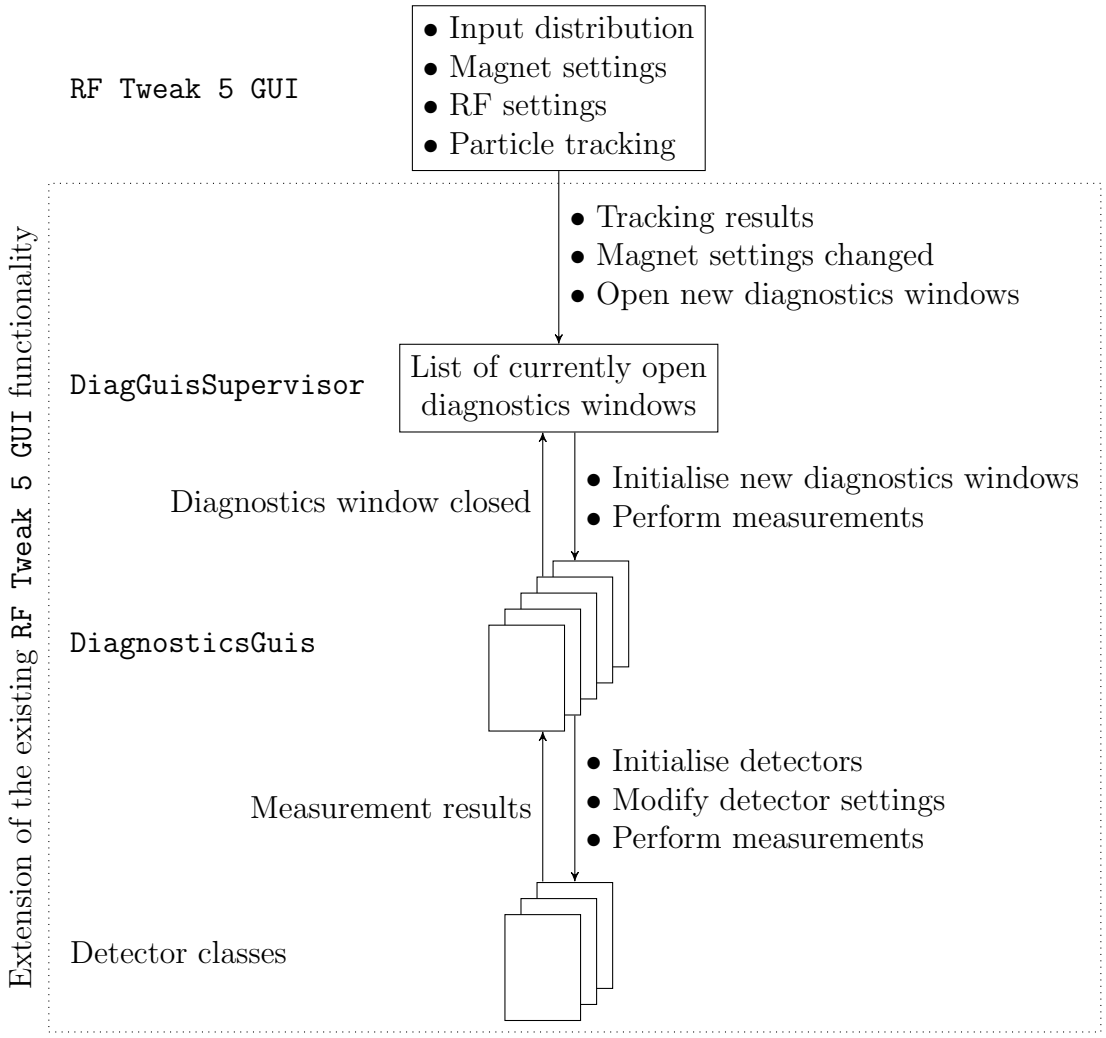

Figure 5.16: Separation of the diagnostics windows program logic from the existing `RF Tweak 5 GUI` code. The arrows indicate the direction of event notifications and data flow.

6 Performance Studies at FLASH

6.1 Influence of Single Cavity Phases on Time-of-Flight in ACC1

As per Equation 1.3, the longitudinal momentum gain of a particle traversing an accelerating module is given by

$$\Delta p_z = \frac{|q|}{c} A \cos(\phi)\,. \tag{6.1}$$

A and ϕ denote the amplitude and phase set point in volts and radians with respect to the reference phase $\phi = 0$. $|q|$ is the absolute charge of the particle, corresponding to the elementary charge in case of electrons.

Changes in the arrival time of the bunches at the accelerating module result in the particles experiencing the electromagnetic field at a different RF phase ϕ. For FLASH and the European XFEL, the fundamental module operating frequency is $f_{\mathrm{RF}} = 1.3\,\mathrm{GHz}$. In this case, a timing change of $\delta t = 1\,\mathrm{ps}$ corresponds to a phase shift of $\psi = \delta\phi = 2\pi f_{\mathrm{RF}} \delta t$ or $\delta\Phi \approx 0.47°$, with $\Phi = \frac{180°}{\pi}\phi$ denoting the phase in degrees.

The accelerating field has a sinusoidal course in time, expressed by the cosine term in Equation 6.1 with $\phi = 2\pi f_{\mathrm{RF}} t = \omega_{\mathrm{RF}} t$. Hence, a phase shift results in a changed momentum gain of the particles

$$\left(\frac{\mathrm{d}}{\mathrm{d}t}\cos(\phi)\right)\delta t = \left(-\sin(\phi)\frac{\mathrm{d}}{\mathrm{d}t}\phi\right)\delta t = -2\pi f_{\mathrm{RF}}\sin(\phi)\delta t$$

in first order. The typical operating point of the first accelerating module at FLASH is $\Phi_{\mathrm{ACC1}} = 5°$. For this setting, a timing change of $\delta t = 1\,\mathrm{ps}$ causes a relative effective field gradient change of $-0.07\,\%$.

This effect exists at all RF stations. For ultrarelativistic particles ($\gamma \gg 1$), it does not change the time-of-flight through the module, as their velocity is already very close to the speed of light ($v \approx c$). It does however influence the energy gain and energy distribution in the bunch. This in turn can cause arrival time and bunch compression changes downstream a dispersive section, such as the magnetic chicane of a bunch compressor.

In the section between the RF gun and the entrance of the first accelerating module (named 'ACC1' at FLASH, see Figure 1.3 on page 14), the beam is not yet ultrarelativ-

istic. The electrons leaving the RF gun have a momentum of $p_{\mathrm{Gun}} \approx 4.5\,\mathrm{MeV/c}$ – compared to their rest mass $m_{\mathrm{e}} \approx 0.511\,\mathrm{MeV/c^2}$ – corresponding to a Lorentz factor of

$$\gamma_{\mathrm{Gun}} = \frac{p_{\mathrm{Gun}} c}{m_{\mathrm{e}} c^2} + 1 \approx 9.8\,, \quad \beta_{\mathrm{Gun}} = \sqrt{1 - \gamma_{\mathrm{Gun}}^{-2}} \approx 0.995 = 1 - 5 \times 10^{-3}\,.$$

Because the beam is not yet ultrarelativistic at the entrance of ACC1, an RF phase variation results in a changed time-of-flight through the module. Thus the bunch arrival time downstream of ACC1 can vary, even without any dispersive beam optics elements in between.

Further downstream in the accelerator, this effect decreases. In the magnetic chicane of the first bunch compressor (named 'BC2' at FLASH), the beam typically has a momentum of $p_{\mathrm{BC2}} = 145\,\mathrm{MeV/c}$, corresponding to $\gamma_{\mathrm{BC2}} \approx 285$ and $\beta_{\mathrm{Gun}} \approx 0.999994 = 1 - 6 \times 10^{-6}$, and can thus be considered ultrarelativistic.

First Cavity

ACC1 comprises eight identical cavities. The forward phase of each cavity can be adjusted individually with the help of motorised phase shifters installed in the waveguide distribution system between the klystron and the accelerating module. This setup can be used for investigating the influence of the single cavity phases on the arrival time of the electron bunches downstream of ACC1.

The change in time-of-flight experienced by the bunches traversing ACC1 has been simulated and verified with measurements during machine studies at FLASH. For the simulations the particle tracking code ASTRA presented in section 1.4.2 has been used. The computation was stopped at the entrance of the third harmonic accelerating module (named 'ACC39'). During the measurements, this module was switched off. As detector, the bunch arrival time monitor (BAM)[1] installed downstream the first accelerating section is used.

Figure 6.1 shows the results for the first cavity. In the measurement data, the actual cavity phase read back values provided by the low-level radio frequency (LLRF) controller are used. At every measurement point, 100 macropulses – each comprising a single bunch – have been recorded and averaged for plotting. The error bars indicate the standard deviation of the measurements. The actuator value (waveguide phase shifter motor steps) is not shown.

The measurement is in good agreement with the particle tracking results. The observed displacement of the arrival time minimum with respect to $\delta\Phi = 0°$ is caused by the off-crest operating point of the module. For large negative phase changes, the measurement shows a slightly steeper dependency than the simulation. The position of the arrival time minimum differs between the two curves by 5°. Possible reasons for the

[1] named '1UBC2': one metre upstream the magnetic chicane of the first bunch compressor, see Figure 2.3 on page 25.

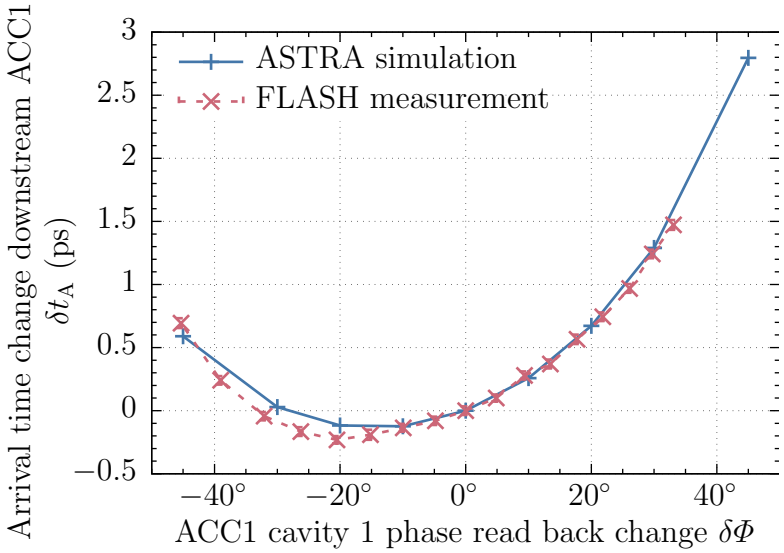

Figure 6.1: Simulation and measurement of the influence of a phase change in the first cavity of ACC1 on the arrival time downstream of ACC1.

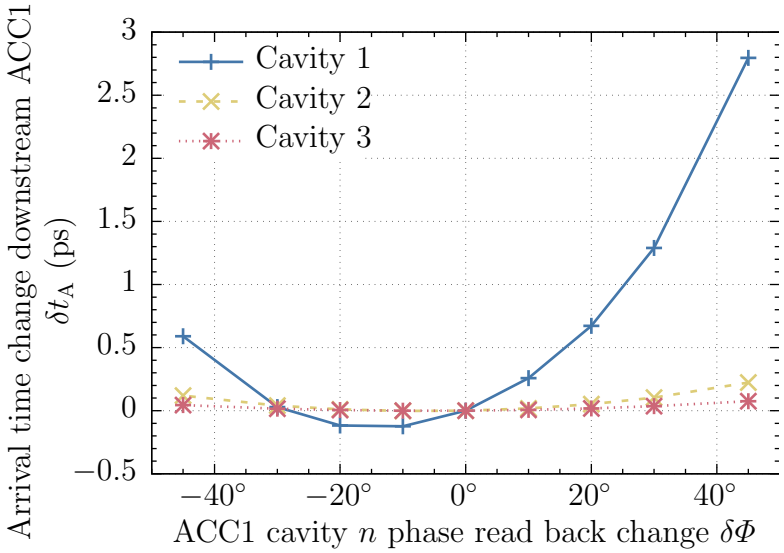

Figure 6.2: Simulation of the influence of a phase change in the first three cavities of ACC1 on the arrival time downstream of ACC1. The curve for cavity 1 is the same as in Figure 6.1.

discrepancy might be an uncertainty of the exact on-crest phase setting of the accelerating module, the particle distribution in the bunch as well as the timing between the injector laser and the phases of the RF gun and ACC1.

Subsequent Cavities

As mentioned above, ACC1 comprises eight identical cavities. The mean momentum gain per individual cavity is

$$\overline{\Delta p}_{\mathrm{Cav}} = \frac{\Delta p_{\mathrm{ACC1}}}{8} \approx 20\,\mathrm{MeV}/c\,.$$

It is thus expected that the effect is strongly reduced for cavities further downstream in the module due to the increased Lorentz factor. This is confirmed by according ASTRA simulations shown in Figure 6.2. The influence of phase changes on the arrival time downstream ACC1 is largely reduced for the subsequent cavities.

6.2 Feedback Response Matrix

In order to determine the regulation parameters for the beam-based feedback controller, the behaviour of the monitor quantities with respect to changes of the actuator values must be known. This dependency is described by the feedback response matrix at a given working point of the system. It describes the reaction of the individual monitors to small variations of the different actuators in linear order around the working point

$$\begin{pmatrix} \delta M_1 \\ \vdots \\ \delta M_m \end{pmatrix} = \mathbf{R} \begin{pmatrix} \delta A_1 \\ \vdots \\ \delta A_n \end{pmatrix} . \tag{6.2}$$

M_i denote the individual monitor values, A_j the individual actuator values and $\mathbf{R}$ the $m \times n$ response matrix at the given working point.

For the scope of this section, the actuators are the amplitude and phase set points of the accelerating modules (see Figure 1.3 on page 14). The monitors are beam diagnostics measurements such as bunch arrival time and bunch compression at various locations along the machine (see Figure 2.3 on page 25 and Figure 2.8 on page 31). In the following, analytical calculations, measurements and simulations using the beam-based feedback framework introduced in chapter 5 are presented.

6.2.1 Bunch Arrival Time

Equation 1.6 on page 10 describes the change of the particle arrival time downstream a magnetic chicane for small variations around the nominal momentum

$$\delta t_{\mathrm{A}} = -\frac{R_{56}}{c}\frac{\delta p_z}{p_z}\,. \tag{6.3}$$

In the presented studies, the values $R_{56,\mathrm{BC2}} = 181.3\,\mathrm{mm}$ and $R_{56,\mathrm{BC3}} = 69.5\,\mathrm{mm}$ are used for the first and second bunch compressor at FLASH respectively.

First Bunch Compressor

Based on Equation 1.3 on page 8, the nominal particle momentum at the magnetic chicane of the first bunch compressor[2] is defined by the momentum of the electron emitted by the RF gun plus the momentum gain in the accelerating modules

$$\begin{aligned} p_{\mathrm{BC2}} &= p_{\mathrm{Gun}} + \Delta p_{\mathrm{ACC1}} + \Delta p_{\mathrm{ACC39}} \\ &= p_{\mathrm{Gun}} + \frac{|q|}{c}\left[A_{\mathrm{ACC1}}\cos(\phi_{\mathrm{ACC1}}) + A_{\mathrm{ACC39}}\cos(\pi + \phi_{\mathrm{ACC39}})\right]. \end{aligned} \tag{6.4}$$

A and ϕ denote the amplitude and phase set point of the particular accelerating module in volts and radians with respect to the reference phase $\phi = 0$. The reference phase is defined such that particles traversing the module experience the maximum momentum transfer. This usually means maximum momentum gain, with the exception of ACC39 where it means maximum momentum loss, as ACC39 decelerates the beam. This feature is described by a phase shift of π in Equation 6.4. $|q| = e$ is the absolute charge of a single particle.

A momentum change δp_{BC2} is introduced by varying the amplitude or phase set points of the first fundamental and the third harmonic accelerating modules around the working point. The set point of the gun is kept constant. In linear approximation, the resulting momentum change of the particles in the magnetic chicane of the first bunch compressor reads

$$\begin{aligned} \delta p_{\mathrm{BC2}} &= \frac{\mathrm{d}p_{\mathrm{BC2}}}{\mathrm{d}A_{\mathrm{ACC1}}}\delta A_{\mathrm{ACC1}} + \frac{\mathrm{d}p_{\mathrm{BC2}}}{\mathrm{d}\phi_{\mathrm{ACC1}}}\delta\phi_{\mathrm{ACC1}} + \frac{\mathrm{d}p_{\mathrm{BC2}}}{\mathrm{d}A_{\mathrm{ACC39}}}\delta A_{\mathrm{ACC39}} + \frac{\mathrm{d}p_{\mathrm{BC2}}}{\mathrm{d}\phi_{\mathrm{ACC39}}}\delta\phi_{\mathrm{ACC39}} \\ &= \frac{|q|}{c}\big[\cos(\phi_{\mathrm{ACC1}})\delta A_{\mathrm{ACC1}} - A_{\mathrm{ACC1}}\sin(\phi_{\mathrm{ACC1}})\delta\phi_{\mathrm{ACC1}} \\ &\quad + \cos(\pi + \phi_{\mathrm{ACC39}})\delta A_{\mathrm{ACC39}} - A_{\mathrm{ACC39}}\sin(\pi + \phi_{\mathrm{ACC39}})\delta\phi_{\mathrm{ACC39}}\big]. \end{aligned} \tag{6.5}$$

In order to describe the effects of a change of the *relative amplitude* and the *phase in degrees*, the substitutions $\tilde{A} = \frac{A}{A_{\mathrm{WP}}}$ and $\Phi = \frac{180^\circ}{\pi}\phi$ are made. Here, A denotes the actual amplitude and A_{WP} the value at the working point, both in volts. $\tilde{A}$ then describes the relative amplitude: $A = \tilde{A}A_{\mathrm{WP}}$. Φ is the phase in degrees and $\phi = \frac{\pi}{180^\circ}\Phi$ in radians.

This formalism allows for an analytical calculation of the linear arrival time response matrix coefficients downstream the first bunch compressor (DBC2)

$$\mathbf{R}(t_{\mathrm{A}})_{\mathrm{BC2}} = \left(\frac{\mathrm{d}}{\mathrm{d}\tilde{A}_{\mathrm{ACC1}}}, \frac{\mathrm{d}}{\mathrm{d}\Phi_{\mathrm{ACC1}}}, \frac{\mathrm{d}}{\mathrm{d}\tilde{A}_{\mathrm{ACC39}}}, \frac{\mathrm{d}}{\mathrm{d}\Phi_{\mathrm{ACC39}}}\right)\delta t_{\mathrm{A}}\,\Big|_{\mathrm{DBC2}}$$

[2] named 'BC2' at FLASH, see Figure 1.3 on page 14.

$$
\begin{aligned}
&= -\frac{R_{56,\mathrm{BC2}}}{p_{\mathrm{BC2}}c}\left(\frac{\mathrm{d}}{\mathrm{d}\tilde{A}_{\mathrm{ACC1}}}, \frac{\mathrm{d}}{\mathrm{d}\Phi_{\mathrm{ACC1}}}, \frac{\mathrm{d}}{\mathrm{d}\tilde{A}_{\mathrm{ACC39}}}, \frac{\mathrm{d}}{\mathrm{d}\Phi_{\mathrm{ACC39}}}\right) p_{\mathrm{BC2}} \\
&= -\frac{|q|}{c^2}\frac{R_{56,\mathrm{BC2}}}{p_{\mathrm{BC2}}}\Big(A_{\mathrm{ACC1}}\cos(\Phi_{\mathrm{ACC1}}), \\
&\qquad\qquad -\frac{\pi}{180^\circ}A_{\mathrm{ACC1}}\sin(\Phi_{\mathrm{ACC1}}), \\
&\qquad\qquad A_{\mathrm{ACC39}}\cos(180^\circ+\Phi_{\mathrm{ACC39}}), \\
&\qquad\qquad -\frac{\pi}{180^\circ}A_{\mathrm{ACC39}}\sin(180^\circ+\Phi_{\mathrm{ACC39}})\Big)\,.
\end{aligned}
\tag{6.6}
$$

The term $\frac{\pi}{180^\circ}$ in the derivatives with respect to the phase results from the representation of the phase in degrees instead of radians. For the accelerator working point

$$
\begin{aligned}
A_{\mathrm{ACC1}} &= 162.4\,\mathrm{MV}\,, \quad \Phi_{\mathrm{ACC1}} = 4.81^\circ\,, \\
A_{\mathrm{ACC39}} &= 20.1\,\mathrm{MV}\,, \quad \Phi_{\mathrm{ACC39}} = -11.05^\circ\,,
\end{aligned}
\tag{6.7}
$$

the resulting values are given in Table 6.1. The particle momentum in the magnetic chicane of the first bunch compressor at the working point is $p_{\mathrm{BC2}} = 146.6\,\mathrm{MeV/c}$. Figure 6.3 shows the phase space distribution of the bunch downstream BC2 at the nominal working point.

Module	Amplitude $\left(\frac{\mathrm{ps}}{\%}\right)$	Phase $\left(\frac{\mathrm{ps}}{^\circ}\right)$
ACC1	−6.68	0.98
ACC39	0.81	0.28

Table 6.1: Analytical values of the linear arrival time response matrix coefficients for the first bunch compressor at FLASH.

The analytical, simulated and measured results are presented in Figure 6.4 together with the bunch compression monitor (BCM) signals[3]. For each sub-plot, all but one component of Equation 6.6 have been set to zero. Both the arrival time simulations and measurements follow the analytical curves very closely, with small deviations of the measurement data towards large actuator variations. The slope of the analytical curves at the working point ($\delta = 0$) corresponds to the values presented in Table 6.1.

A possible reason for the observed deviations might be the effect shown in section 6.1. The time-of-flight dependency on the phase at which the particles traverse ACC1 is not taken into account in the analytical description nor in `RF Tweak`. In addition,

[3]The BCM voltage readings have a negative polarity with a growing absolute value for increasing signal strength. In order to improve the readability, the corresponding axis is reversed in all plots.

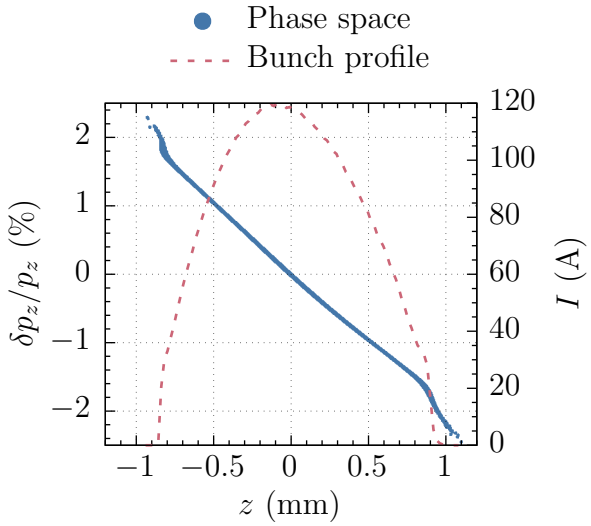

Figure 6.3: `RF Tweak` simulation of the phase space distribution of the electron bunch downstream the magnetic chicane of the first bunch compressor at FLASH at the nominal working point.

uncertainties of the exact on-crest phase setting[4] of the accelerating modules and the particle distribution in the bunch affect the accuracy of the experiment.

For the bunch compression monitor (BCM) readings, the signal amplitude is found to be lower in the measurements than in the simulations. A possible reason is attenuation of the coherent diffraction radiation on its way from the screen to the detector (see Figure 2.6 on page 28), which is approximately 1.3 m long at FLASH [Wes12, p. 42]. Alternatively, a limited detector efficiency or misalignment can reduce the sensitivity. In addition, a motor stage allows moving the detector out of the diffraction radiation focus, which also influences the signal intensity and is not included in the simulations. For better comparability, the simulation signal has been scaled for plotting.

Aside from the small systematic offset, the shapes of the simulation and measurement curves are in good agreement. The bunch compression signal is more sensitive to the module phase than to the amplitude, as the phase dominantly affects the energy chirp over the bunch and thus the compression. In contrast to the arrival time, the BCM signal is not nearly linear over the scan range, but strongly depends on the actual working point. This has consequences for a beam-based feedback system using the BCM data: before closing the feedback loop, the response around the working point needs to be measured instead of simply using a fixed, constant gain.

[4]Before and after the measurement shift, the on-crest phases of the accelerating modules have been measured. This is done by successively varying the phase set point of each station and recording the arrival time change downstream the subsequent magnetic chicane. The setting at which the minimum (for ACC1) respectively maximum (for ACC39) timing occurs is defined as the on-crest phase. The resulting value typically has an uncertainty of 0.1°.

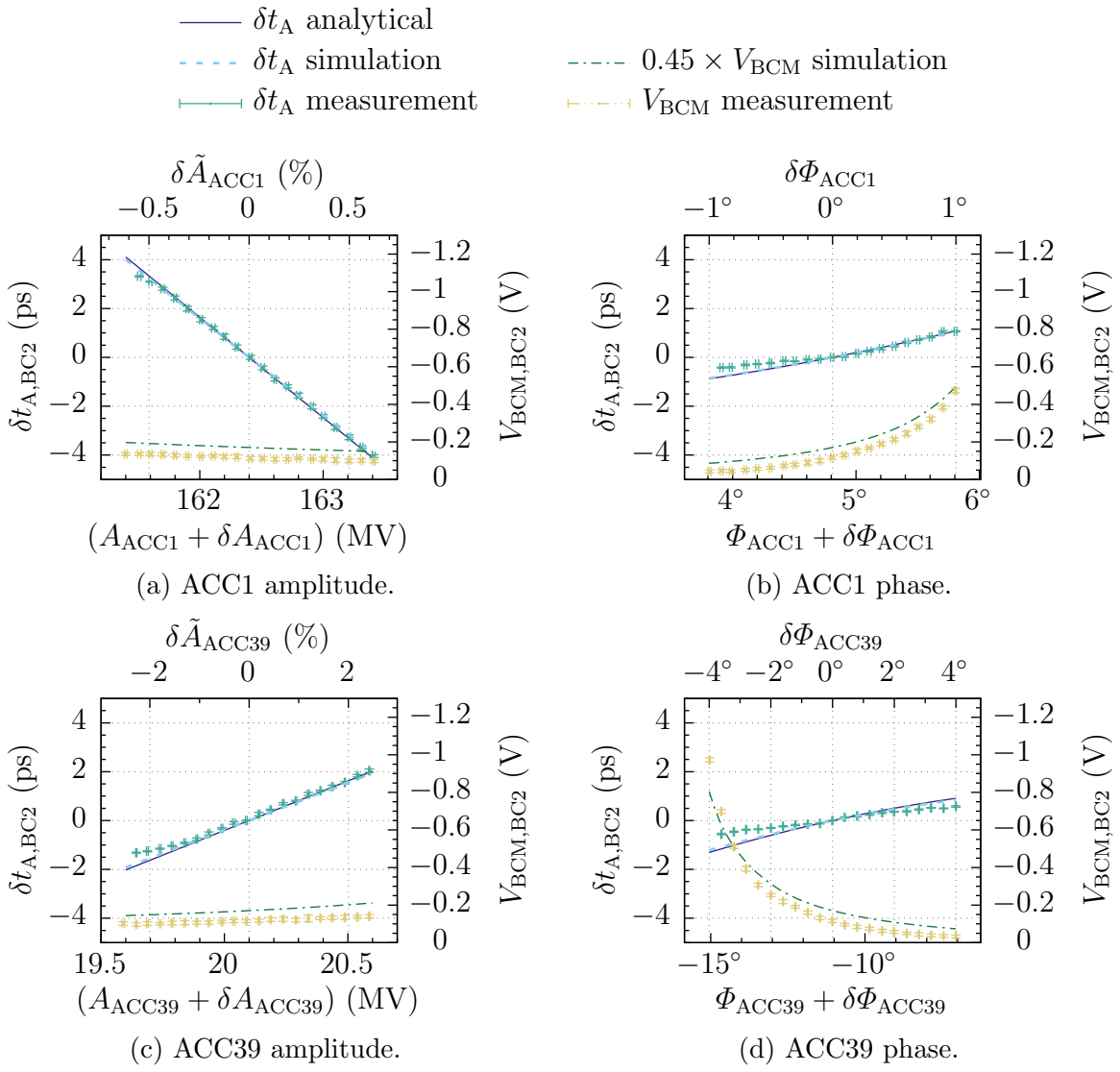

(a) ACC1 amplitude.

(b) ACC1 phase.

(c) ACC39 amplitude.

(d) ACC39 phase.

Figure 6.4: Analytical results, simulation and measurement of the bunch arrival time and bunch compression monitor signals downstream the first bunch compressor at FLASH as a function of the set point of ACC1 and ACC39 for a bunch charge of 0.6 nC. The V_{BCM} axis is reversed for better readability.

Second Bunch Compressor

Similarly to Equation 6.4, the nominal particle momentum at the magnetic chicane of the second bunch compressor[5] is defined by the momentum of the electrons in the first bunch compression chicane plus the momentum gain in the subsequent accelerating section

$$p_{\mathrm{BC3}} = p_{\mathrm{BC2}} + \Delta p_{\mathrm{ACC23}} = p_{\mathrm{BC2}} + \frac{|q|}{c} A_{\mathrm{ACC23}} \cos(\varphi_{\mathrm{ACC23}}) \,, \tag{6.8}$$

with $|q| = e$. Arrival time changes downstream the first bunch compressor cause the electrons to traverse the subsequent accelerating modules at a different RF phase. As shown in section 6.1, a timing difference δt corresponds to a phase shift of $\psi = 2\pi f_{\mathrm{RF}} \delta t$, amounting to $0.47\,^\circ$/ps for the fundamental frequency of $f_{\mathrm{RF}} = 1.3\,\mathrm{GHz}$. This leads to a changed momentum gain of the particles in the subsequent accelerating section, which in turn affects the bunch arrival time and compression state downstream the next magnetic chicane.

In Equation 6.8, this effect is accounted for by using

$$\varphi_{\mathrm{ACC23}} \coloneqq \phi_{\mathrm{ACC23}} + \psi_{\mathrm{ACC23}} = \phi_{\mathrm{ACC23}} + 2\pi f_{\mathrm{RF}} \delta t_{\mathrm{BC2}} \,. \tag{6.9}$$

φ_{ACC23} describes the effective phase at which the bunch gets accelerated in ACC23, considering the nominal phase set point ϕ_{ACC23} and the timing change contribution δt_{BC2} caused by a changed momentum in the first bunch compressor. δt_{BC2} can be obtained from Equation 6.3 yielding

$$\varphi_{\mathrm{ACC23}} = \phi_{\mathrm{ACC23}} - 2\pi f_{\mathrm{RF}} \frac{R_{56,\mathrm{BC2}}}{c} \frac{\delta p_{\mathrm{BC2}}}{p_{\mathrm{BC2}}} \,, \tag{6.10}$$

with δp_{BC2} given by Equation 6.5. For bunches with nominal momentum in the magnetic chicane of the first bunch compressor ($\delta p_{\mathrm{BC2}} = 0$), no phase adjustment occurs and $\varphi_{\mathrm{ACC23}} = \phi_{\mathrm{ACC23}}$.

A momentum change δp_{BC3} is introduced by varying the amplitude and phase set points of the first two fundamental and the third harmonic accelerating stations around the working point. The resulting momentum deviation of the particles in the magnetic chicane of the second bunch compressor at the design momentum ($\varphi_{\mathrm{ACC23}} = \phi_{\mathrm{ACC23}}$) has a similar structure to Equation 6.5, but with additional terms originating from Equation 6.10. In linear approximation, it reads

$$\delta p_{\mathrm{BC3}} = \sum_{\substack{X \in \{A,\phi\} \\ i \in \{1,39,23\}}} \frac{\mathrm{d}p_{\mathrm{BC3}}}{\mathrm{d}X_{\mathrm{ACC}i}} \delta X_{\mathrm{ACC}i} = \delta p_{\mathrm{BC2}} + \sum_{\substack{X \in \{A,\phi\} \\ i \in \{1,39,23\}}} \frac{\mathrm{d}\Delta p_{\mathrm{ACC23}}}{\mathrm{d}X_{\mathrm{ACC}i}} \delta X_{\mathrm{ACC}i}$$

[5] named 'BC3' at FLASH, see Figure 1.3 on page 14.

$$
\begin{aligned}
&= \frac{|q|}{c}\big[\,(1+C_{\phi_{\mathrm{ACC23}}})\cos(\phi_{\mathrm{ACC1}})\delta A_{\mathrm{ACC1}} \\
&\quad -\,(1+C_{\phi_{\mathrm{ACC23}}})\,A_{\mathrm{ACC1}}\sin(\phi_{\mathrm{ACC1}})\delta\phi_{\mathrm{ACC1}} \\
&\quad +\,(1+C_{\phi_{\mathrm{ACC23}}})\cos(\pi+\phi_{\mathrm{ACC39}})\delta A_{\mathrm{ACC39}} \\
&\quad -\,(1+C_{\phi_{\mathrm{ACC23}}})\,A_{\mathrm{ACC39}}\sin(\pi+\phi_{\mathrm{ACC39}})\delta\phi_{\mathrm{ACC39}} \\
&\quad +\,\cos(\phi_{\mathrm{ACC23}})\delta A_{\mathrm{ACC23}} \\
&\quad -\,A_{\mathrm{ACC23}}\sin(\phi_{\mathrm{ACC23}})\delta\phi_{\mathrm{ACC23}}\big]\,.
\end{aligned}
\tag{6.11}
$$

The coefficient

$$
C_{\phi_{\mathrm{ACC23}}} = 2\pi f_{\mathrm{RF}}\frac{|q|}{c^2}\frac{R_{56,\mathrm{BC2}}}{p_{\mathrm{BC2}}}A_{\mathrm{ACC23}}\sin(\phi_{\mathrm{ACC23}})
$$

is a measure of the influence of the changed ACC23 phase operating point due to a different transit time through the magnetic chicane of the first bunch compressor. With $R_{56,\mathrm{BC2}} = 181.3\,\mathrm{mm} > 0\,\mathrm{mm}$ and $0 < \phi_{\mathrm{ACC23}} < \pi$ (see Equation 6.13), $C_{\phi_{\mathrm{ACC23}}}$ is positive. This means it increases the slope of the derivative of the particular component of δp_{BC3} with respect to the operating point of the accelerating modules upstream the magnetic chicane of the first bunch compressor. Data sets illustrating this effect are included in Figure 6.6. At the machine working point as given by Equation 6.7 and Equation 6.13, the coefficient value is $C_{\phi_{\mathrm{ACC23}}} = 3.17$.

The linear arrival time response matrix coefficients downstream the second bunch compressor (DBC3) – with respect to the *relative amplitude* and *phase in degrees* – read, similar to Equation 6.6,

$$
\begin{aligned}
\mathbf{R}(t_{\mathrm{A}})_{\mathrm{BC3}} &= \left(\frac{\mathrm{d}}{\mathrm{d}\tilde{A}_{\mathrm{ACC1}}},\frac{\mathrm{d}}{\mathrm{d}\Phi_{\mathrm{ACC1}}},\frac{\mathrm{d}}{\mathrm{d}\tilde{A}_{\mathrm{ACC39}}},\frac{\mathrm{d}}{\mathrm{d}\Phi_{\mathrm{ACC39}}},\frac{\mathrm{d}}{\mathrm{d}\tilde{A}_{\mathrm{ACC23}}},\frac{\mathrm{d}}{\mathrm{d}\Phi_{\mathrm{ACC23}}}\right)\delta t_{\mathrm{A}}\,\Big|_{\mathrm{DBC3}} \\
&= -\frac{R_{56,\mathrm{BC3}}}{p_{\mathrm{BC3}}c}\left(\frac{\mathrm{d}p_{\mathrm{BC3}}}{\mathrm{d}\tilde{A}_{\mathrm{ACC1}}},\frac{\mathrm{d}p_{\mathrm{BC3}}}{\mathrm{d}\Phi_{\mathrm{ACC1}}},\frac{\mathrm{d}p_{\mathrm{BC3}}}{\mathrm{d}\tilde{A}_{\mathrm{ACC39}}},\frac{\mathrm{d}p_{\mathrm{BC3}}}{\mathrm{d}\Phi_{\mathrm{ACC39}}},\frac{\mathrm{d}p_{\mathrm{BC3}}}{\mathrm{d}\tilde{A}_{\mathrm{ACC23}}},\frac{\mathrm{d}p_{\mathrm{BC3}}}{\mathrm{d}\Phi_{\mathrm{ACC23}}}\right) \\
&= -\frac{|q|}{c^2}\frac{R_{56,\mathrm{BC3}}}{p_{\mathrm{BC3}}}\Big(\,(1+C_{\phi_{\mathrm{ACC23}}})\,A_{\mathrm{ACC1}}\cos(\Phi_{\mathrm{ACC1}}), \\
&\qquad\qquad -\,(1+C_{\phi_{\mathrm{ACC23}}})\,\frac{\pi}{180^\circ}A_{\mathrm{ACC1}}\sin(\Phi_{\mathrm{ACC1}}), \\
&\qquad\qquad (1+C_{\phi_{\mathrm{ACC23}}})\,A_{\mathrm{ACC39}}\cos(180^\circ+\Phi_{\mathrm{ACC39}}), \\
&\qquad\qquad -\,(1+C_{\phi_{\mathrm{ACC23}}})\,\frac{\pi}{180^\circ}A_{\mathrm{ACC39}}\sin(180^\circ+\Phi_{\mathrm{ACC39}}), \\
&\qquad\qquad A_{\mathrm{ACC23}}\cos(\Phi_{\mathrm{ACC23}}), \\
&\qquad\qquad -\,\frac{\pi}{180^\circ}A_{\mathrm{ACC23}}\sin(\Phi_{\mathrm{ACC23}})\Big)\,.
\end{aligned}
\tag{6.12}
$$

For the accelerator working point as given in Equation 6.7, in combination with the operating point of the second fundamental station

$$
A_{\mathrm{ACC23}} = 316.1\,\mathrm{MV}\,, \quad \Phi_{\mathrm{ACC23}} = 17.3^\circ\,, \tag{6.13}
$$

Module	Amplitude $\left(\frac{\text{ps}}{\%}\right)$	Phase $\left(\frac{\text{ps}}{^\circ}\right)$
ACC1	−3.49	0.51
ACC39	0.43	0.14
ACC23	−1.56	0.85

Table 6.2: Analytical values of the linear arrival time response matrix coefficients for the second bunch compressor at FLASH.

the resulting values are presented in Table 6.2. The particle momentum in the magnetic chicane of the second bunch compressor at the working point is $p_{\text{BC3}} = 448.4\,\text{MeV}/c$. Figure 6.5 shows the phase space distribution of the bunch downstream BC3 at the nominal working point.

The analytical, simulated and measured results are presented in Figure 6.6 together with the bunch compression monitor (BCM) signals. For each sub-plot, all but one component of Equation 6.12 have been set to zero. Both the arrival time simulations and measurements closely follow the analytical curves, with small differences of the signal slope. Reason for this could be slight deviations of the accelerating modules' on-crest phases or an uncertainty of the R_{56} value of the magnetic chicane of the second bunch compressor. Unlike `RF Tweak` and the measurement, the analytical description neglects higher order dispersion terms, which might as well explain the discrepancy between the

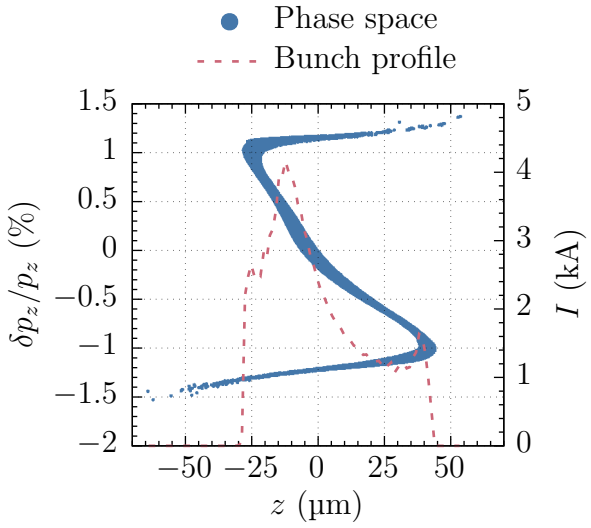

Figure 6.5: `RF Tweak` simulation of the phase space distribution of the electron bunch downstream the magnetic chicane of the second bunch compressor at FLASH at the nominal working point.

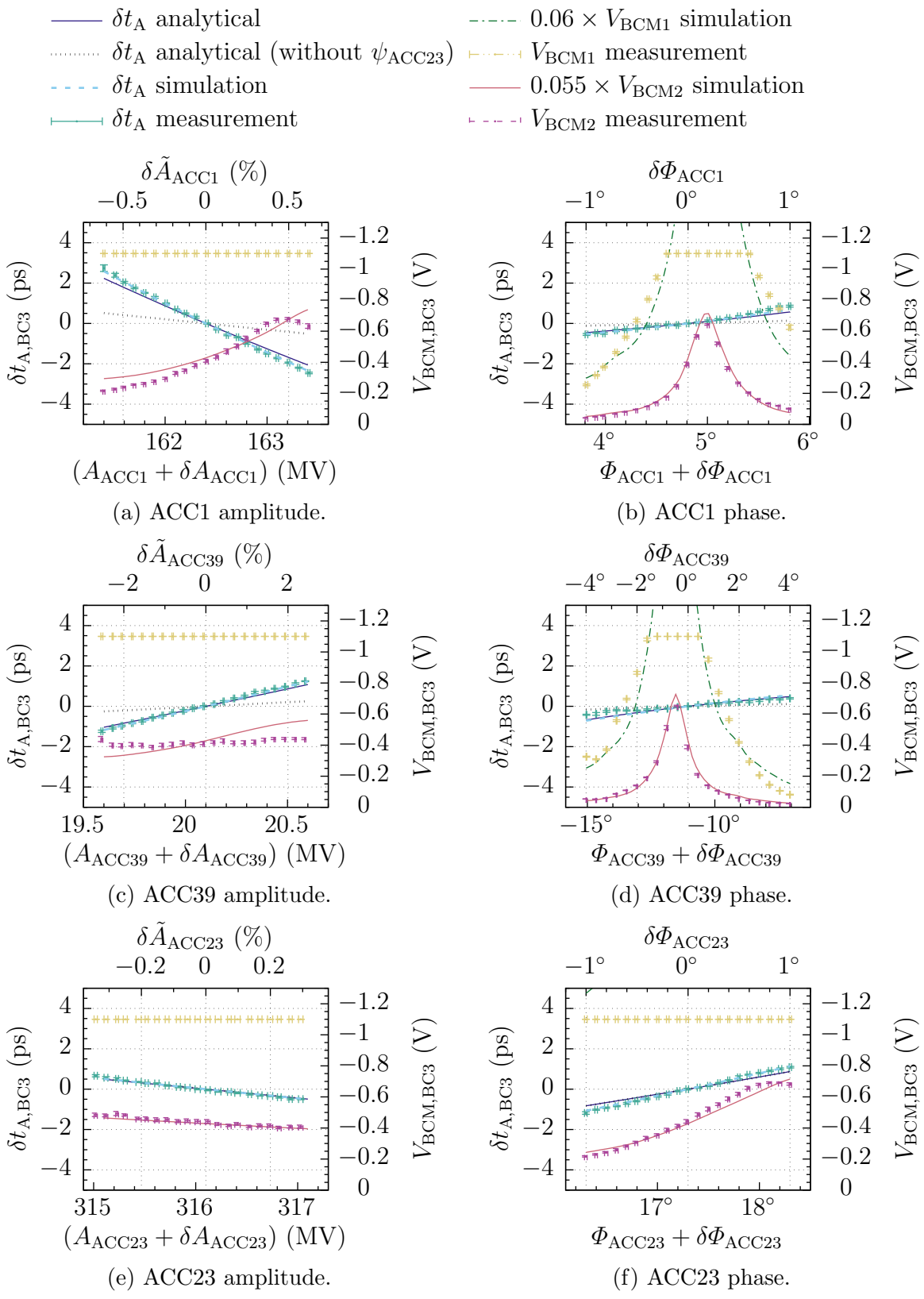

(a) ACC1 amplitude.

(b) ACC1 phase.

(c) ACC39 amplitude.

(d) ACC39 phase.

(e) ACC23 amplitude.

(f) ACC23 phase.

Figure 6.6: Analytical results, simulation and measurement of the bunch arrival time and bunch compression monitor signals downstream the second bunch compressor at FLASH as a function of the set point of ACC1, ACC39 and ACC23 for a bunch charge of 0.6 nC. The V_{BCM} axis is reversed for better readability.

corresponding data sets. The slopes of the analytical curves at the working point ($\delta = 0$) correspond to the values presented in Table 6.2.

The dotted lines in Figure 6.6a to 6.6d represent the analytical arrival time when ψ_{ACC23} is not taken into account in Equation 6.9. For these data sets, the arrival time change is only caused by the changed particle momentum. The slopes of the curves are significantly smaller than for the true case. This implies that the contribution of the changed effective phase the bunch experiences in ACC23 is larger than the effect of the momentum variation itself. The fact that $C_{\phi_{\mathrm{ACC23}}} = 3.17 > 1$ in Equation 6.12 confirms this observation.

As shown in Figure 2.2.2, a BCM station with two detectors of different sensitivities is installed downstream the second bunch compressor at FLASH, providing a fine (BCM1) and a coarse (BCM2) channel. Due to the relatively high bunch charge of 0.6 nC used in the measurements, the BCM1 signal is saturated at the working point. In the simulations, detector saturation is not implemented. For this reason, the BCM1 simulation signal lies outside of the visible data range in most of the plots. As in Figure 6.4, the BCM simulation results have been scaled for plotting in order to fit the slope (BCM1, where it is not saturated) respectively peak height (BCM2) of the measurement data in the phase scans.

6.2.2 Bunch Compression

In principle, the bunch length can be estimated analytically in a similar way as it has been demonstrated in section 6.2.1 for the arrival time, by regarding the evolution of the bunch head and tail separately. However, an analytical derivation of the final compression monitor signal is not feasible due to the frequency dependencies of the coherent diffraction radiation transmission line and the detector response, for which no analytical descriptions are available. Consequently, for this case only simulations and measurements – but no analytical curves – are presented.

6.3 Intra Bunch-Train Feedback

As shown in section 1.2, FLASH is operated at a macropulse repetition rate of 10 Hz. Each macropulse consists of a burst of several electron bunches. The maximum bunch repetition rate within the burst is 1 MHz, with a bunch train length of up to 600 µs. In this way, up to 6000 photon pulses can be generated per second.[6]

For keeping the machine operating conditions constant along the bunch train, an intra-train beam-based feedback (BBF) scheme as shown in Figure 5.13 on page 87 is employed at the first bunch compressor. The relevant beam parameters – such as bunch compression, energy and arrival time – are stabilised by correcting the amplitude and phase set points of the respective accelerating module within each macropulse. Due

[6] provided that only one beamline is operated; for details see section 1.2.

to the high bunch repetition rate, the components of the feedback system – monitors, actuators, controller(s) and information exchange paths – must be fast with characteristic times in the microsecond range. In order to achieve quick adaptation[7], the system bandwidth needs to be sufficiently high.

Figure 6.7 shows the layout of the intra bunch-train feedback at the first bunch compressor of FLASH. The controlled quantity (in-loop monitor) is the bunch arrival time downstream the first bunch compressor (BAM.3DBC2). The feedback actuator is the RF field amplitude in the first accelerating module (ACC1). In order to achieve a high regulation speed, the feedback algorithm is integrated into the firmware of the low-level radio frequency (LLRF) controller running on a field-programmable gate array (FPGA). The data transfer from the beam diagnostics to the LLRF controller is realised via optical high-speed low-latency links. A bunch arrival time monitor downstream the second bunch compressor (BAM.4DBC3) is used as an out-of-loop detector.

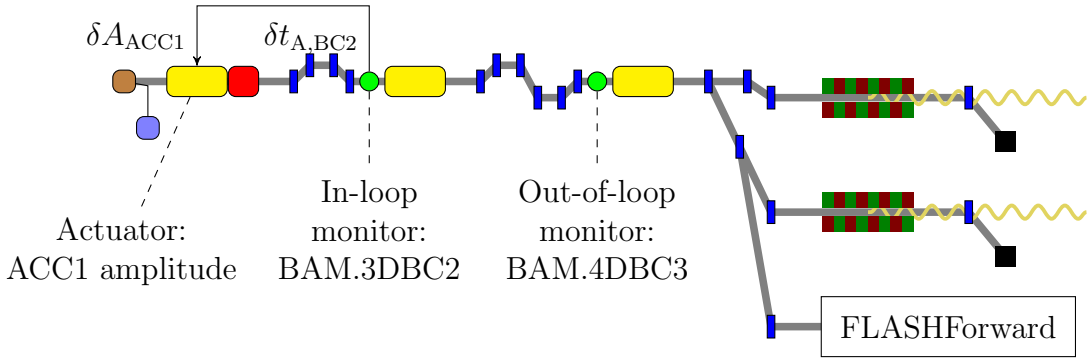

Figure 6.7: Schematic layout of the arrival time feedback at the first bunch compressor of FLASH.

For the measurements, 540 macropulses with trains of 100 bunches each and a bunch repetition rate of 500 kHz have been recorded. In Figure 6.8, the absolute arrival time for all bunches of all macropulses is plotted. The upper plots show the in-loop measurement, the lower ones the out-of-loop signal. During the measurement of the data presented in the left graphs, the BBF was switched off, for the right plots it was switched on. For details on the data analysis see Appendix B.

The BBF significantly reduces the intra bunch-train arrival time jitter. Steady state operation is reached after 16 µs or eight bunches. The necessary adaptation time is caused by the feedback system's delay and finite bandwidth.

For both measurements, BBF off and on, the out-of-loop signal exhibits a larger jitter than the in-loop measurement and in addition has a slope over the bunch train.

[7]This requirement arises from the limited bunch train length. The bunches during the adaptation time usually are discarded by the photon experiments due to their larger jitter, only the stable part of the bunch train is used. The longer the adaptation process takes, the fewer bunches remain for the user experiment.

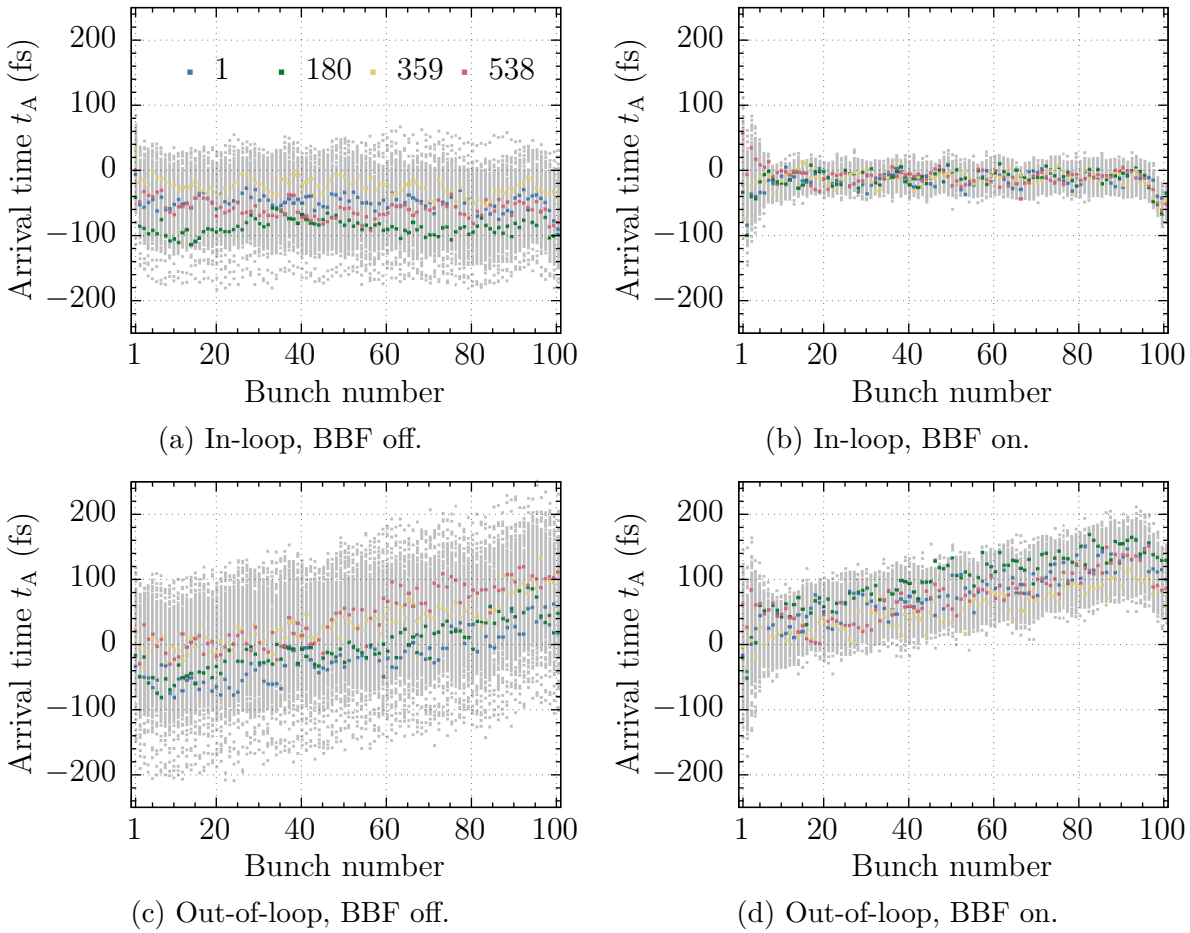

(a) In-loop, BBF off.

(b) In-loop, BBF on.

(c) Out-of-loop, BBF off.

(d) Out-of-loop, BBF on.

Figure 6.8: Measurement of the intra-train bunch arrival time for 540 macropulses with a bunch repetition rate of 500 kHz, without and with beam-based feedback. Four individual macropulses (distributed uniformly over the measured events) are highlighted by coloured data points.

These features originate from the intermediate accelerating (ACC23) and dispersion (the magnetic chicane of the second bunch compressor) section between both monitors. The positive slope of the arrival time over the bunch train indicates that earlier bunches experience a larger momentum gain in ACC23 and hence traverse the magnetic chicane of the second bunch compressor on a shorter path than later ones. This can be compensated by introducing a negative slope in the amplitude flat top of ACC23.

The residual spread of the arrival time signal with BBF on is determined by fast oscillations over the bunch train and the resolution of the in-loop monitor. In Figure 6.8, this is illustrated by four exemplary macropulses which are highlighted by coloured data points. The amplitude of the oscillations is in the same order of magnitude as the resolution of the in-loop bunch arrival time monitor $\sigma(\text{BAM.3DBC2}) \approx 10\,\text{fs}$. It is

planned to further improve the performance of the feedback system in the future by a newly installed normal conducting cavity with high bandwidth in the section between ACC1 and the magnetic chicane of the first bunch compressor. An upgrade of the electro-optical unit for the bunch arrival time monitor (see chapter 3) is currently being prepared and will be installed at FLASH in order to achieve a better arrival time measurement resolution.

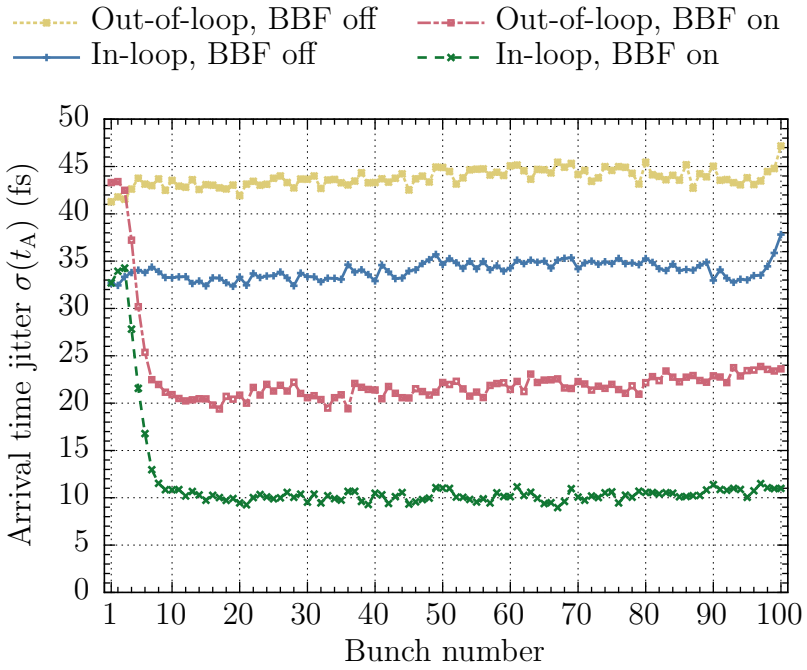

Figure 6.9: Measurement of the intra bunch-train arrival time jitter reduction by beam-based feedback for a bunch repetition rate of 500 kHz. Same data as in Figure 6.8

In Figure 6.9, the arrival time jitter over the bunch train is plotted for all four cases shown in Figure 6.8. The first bunches are not affected by the feedback due to the system delay. Subsequently the adaptation process takes place which needs another few bunches' time, given by the finite system bandwidth. From the ninth bunch on, the intra-train arrival time jitter is reduced from ≈ 35 fs to ≈ 10 fs (in-loop) and from ≈ 44 fs to ≈ 22 fs (out-of-loop). Both the in-loop and out-of loop performance are limited by the detector resolution of approximately 10 fs (in-loop) respectively 22 fs (out-of-loop).

In Figure 6.8, the measurements with BBF on show a systematic drop of the absolute arrival time at the end of the bunch train. This behaviour is present for all macropulses and is not visible in the jitter plots in Figure 6.9. The cause of the deviation is the learning feed forward algorithm trying to restore the original vector sum set point value at the end of the bunch train. It thus competes with the BBF, which tries to establish a possibly different set point given by the BBF target value.

Figure 6.10 illustrates this effect. The vector sum with BBF off and on is equal while there is no beam present, but different during the bunch train. The transition from the BBF-induced value to the original feedforward set point already starts before the end of the bunch train, causing a larger momentum gain and thus an earlier arrival time of the affected bunches.

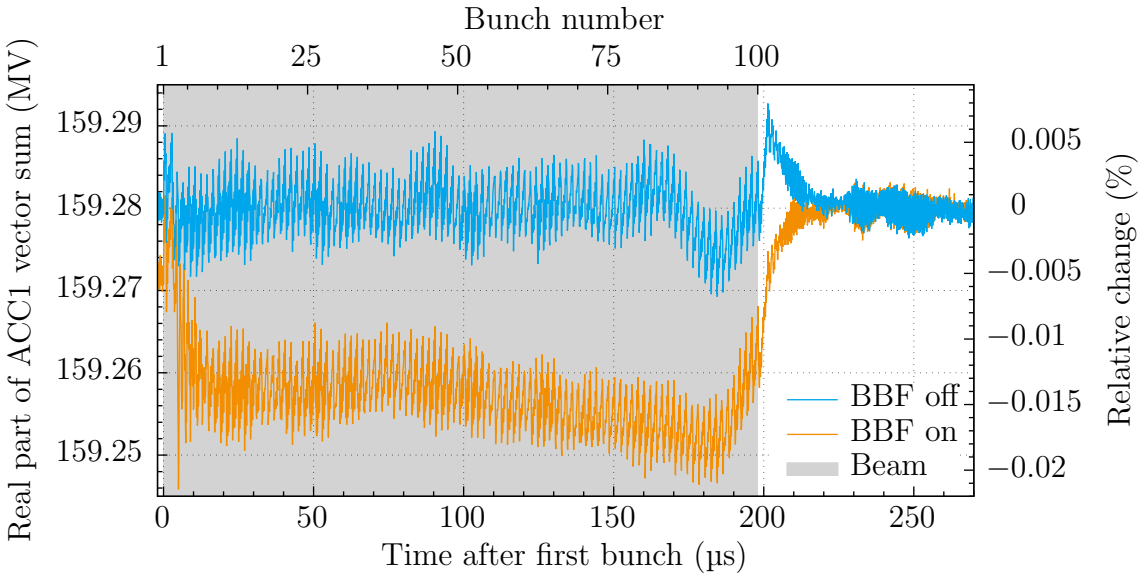

Figure 6.10: Measurement of the ACC1 vector sum along the bunch train with BBF off and on, averaged over 540 macropulses. The bunch train duration is marked by the shaded area. Overshooting after the end of the bunch train for the case 'BBF off' and transients during the bunch train are caused by beam loading. The frequency of the beam loading transients is equal to the bunch repetition rate of 500 kHz. The sampling rate of the data is $f_{\mathrm{LLRF}} = 9\,\mathrm{MHz}$.

A possible reason for the different vector sum levels with BBF off and on are slow drifts. During operation times without BBF, these are compensated by dedicated slow feedback systems. With BBF on, the correction is carried out by the BBF and consequently the slow feedback systems do not detect the drifts. By adjusting the feedforward set point to the BBF-induced vector sum level, this deviation can be removed and the bunches at the end of the train are brought to the same mean arrival time as the rest. Alternatively, the start of the transition from the BBF-induced vector sum level to the original feedforward set point could be shifted to a later point in time, after the last bunch has traversed the accelerating module.

6.3.1 Parameter Optimisation

As shown in section 2.4, the behaviour of the feedback controller can be influenced by adjusting two independent parameters: the field weighting K_F defines the gain value used for minimising the error between the field measurements in the cavities and the RF set point. The beam weighting parameter K_B defines the strength of the contribution of the beam-based diagnostics – such as bunch compression, energy and arrival time – to the combined error signal. In order to determine the optimal operating point, these two parameters have been scanned and the resulting intra bunch-train arrival time jitter reduction has been recorded.

The measurement results are shown in Figure 6.11 for a bunch repetition rate of 500 kHz. For all tested values of K_F and K_B, the arrival time jitter over 540 macropulses has been calculated for every bunch. In the plots, the mean jitter of the last 91 bunches (out of 100) in the train is shown. The first bunches have been discarded due to their larger jitter, as it is usually done by the photon experiments (q.v. footnote 7 on page 104). Between the discrete data points marked by the axis ticks, the values have been interpolated for plotting. BBF off corresponds to $K_\mathrm{F} = 1, K_\mathrm{B} = 0$. For almost all parameter values, the improvement is better than 1 (indicated by a dashed line).

With weighting values outside of the axis limits used in the plots, or if both parameters are very large (corresponding to the white cut-out area in the top right of the plots), the system becomes unstable. In these cases, oscillations build up in the RF flat top and a steady operation is not possible due to beam losses. This limits the range of usable weighting values.

As shown in Figure 6.11a, the in-loop arrival time jitter is reduced by the BBF from 35 fs to 10 fs, corresponding to a relative improvement factor of 3.5. This value is in very good agreement with the results shown in [Pfe14, p. 91] for the former VME system, although the absolute jitter is smaller by a factor of 2.4 with the MicroTCA system (BBF off: 35 fs compared to 85 fs with the VME system). The out-of-loop measurements in Figure 6.11b show an improvement up to a factor of 2.3, reducing the intra-train arrival time jitter from 51 fs to 22 fs. The same colour scale as for the in-loop plot is used for better comparability. As previously noted, both the in-loop and out-of loop performance are limited by the detector resolution of approximately 10 fs (in-loop) respectively 22 fs (out-of-loop).

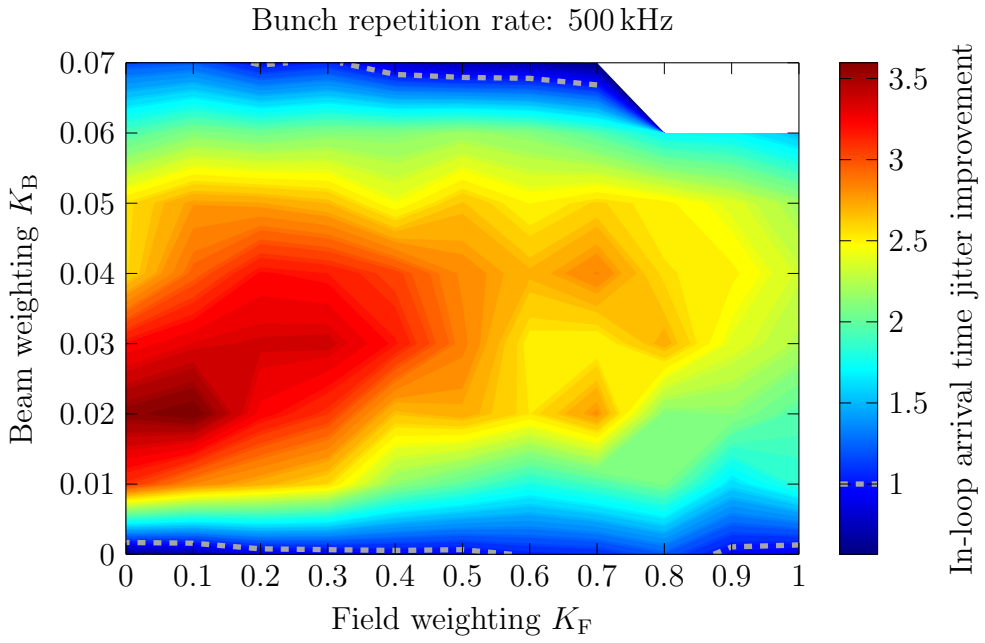

(a) In-loop. A ratio of 1 corresponds to an arrival time jitter of 35 fs (value for BBF off).

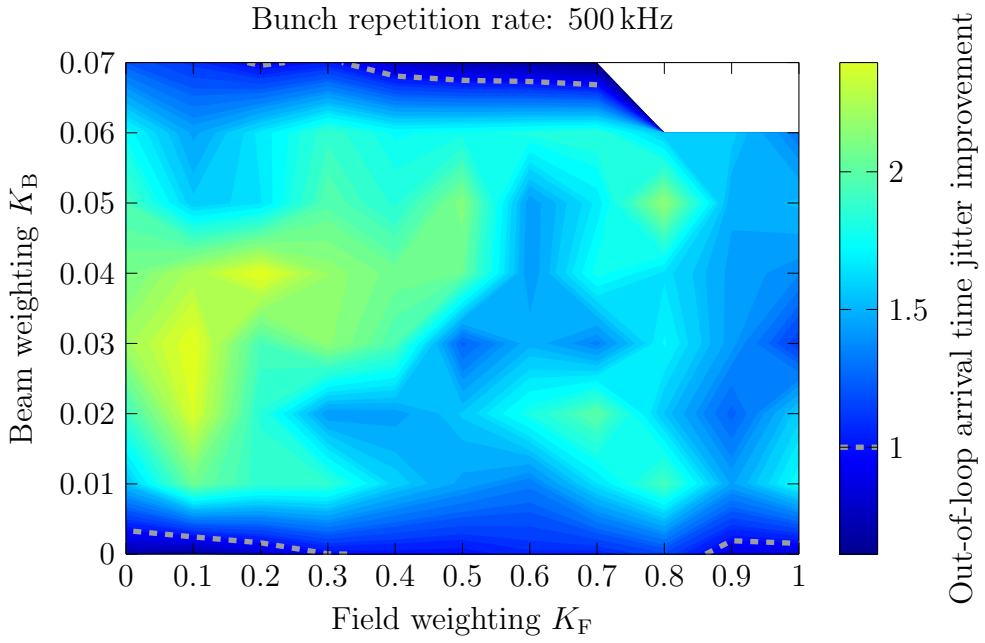

(b) Out-of-loop (same colour scale as in Figure 6.11a). A ratio of 1 corresponds to an arrival time jitter of 51 fs (value for BBF off).

Figure 6.11: Measurement of the intra bunch-train arrival time jitter reduction by beam-based feedback for a bunch repetition rate of 500 kHz. A ratio of 1 is marked with a dashed line. With both control parameters large, the system becomes unstable and a steady beam operation is not possible.

7 Case Studies for the European XFEL

7.1 Bunch Compression Operating Point

The longitudinal beam dynamics in the first bunch compressor (named BC0 at the European XFEL, see section 1.3) is determined by the acceleration scheme employed in the injector and the lattice properties up to the magnetic chicane of BC0. In the injector section, the acceleration scheme defines the amplitude and phase set points of the RF gun as well as the first fundamental and third harmonic accelerating modules (A1 and AH1). The lattice parameters relevant for the longitudinal beam dynamics comprise the dispersion properties of the respective beam transport sections. Additionally, the injector laser pulse characteristics and timing affect the electron bunch dynamics. During operation, the lattice parameters and injector laser characteristics are typically kept constant. For adjusting the longitudinal beam dynamics, the amplitude and phase set points of A1 and AH1 are used.

As shown in Figure 2.7 on page 31, the first bunch compression monitor (BCM) at the European XFEL is installed immediately upstream the magnetic chicane of the second bunch compressor (BC1). Between BC0 and this position, an accelerating section (L1) is located. The acceleration only affects the momentum of the particles, but not their relative longitudinal positions with respect to the bunch centre due to their velocity already being very close to the speed of light ($v \approx c$). Therefore, the longitudinal bunch profile does not change between BC0 and BC1 and a measurement immediately upstream BC1 yields the bunch compression downstream the first bunch compressor.

When the phase set points of A1 and AH1 are varied, the beam dynamics in the dispersive sections change and the BCM signal reacts accordingly. In order to study this effect, beam dynamics simulations have been performed using the framework presented in chapter 5. For this purpose, the A1 and AH1 phase set points have been scanned in steps of 0.05° (A1) respectively 0.15° (AH1) around the design operating point and the resulting signal of the BCM immediately upstream the magnetic chicane of the second bunch compressor has been recorded.

The simulation results are presented in Figure 7.1.[1] As expected, the BCM signal exhibits a strong dependence on both actuators. Regarding the position of the signal peak, a noticeable correlation exists between changes in both dimensions: the maximum compression locus runs parallel to the dashed line which describes a ratio of 1:3 between

[1] The BCM voltage readings have a negative polarity with a growing absolute value for increasing signal strength. In order to improve the readability, the corresponding axis is reversed in all plots.

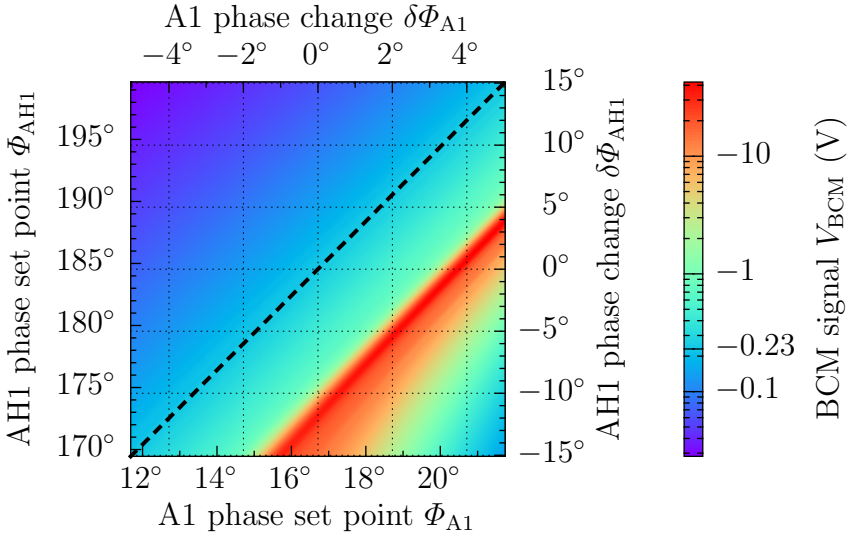

(a) As a function of the phase set points of A1 and AH1 around the design value. The dashed line marks a ratio of 1:3 between A1 and AH1 phase changes.

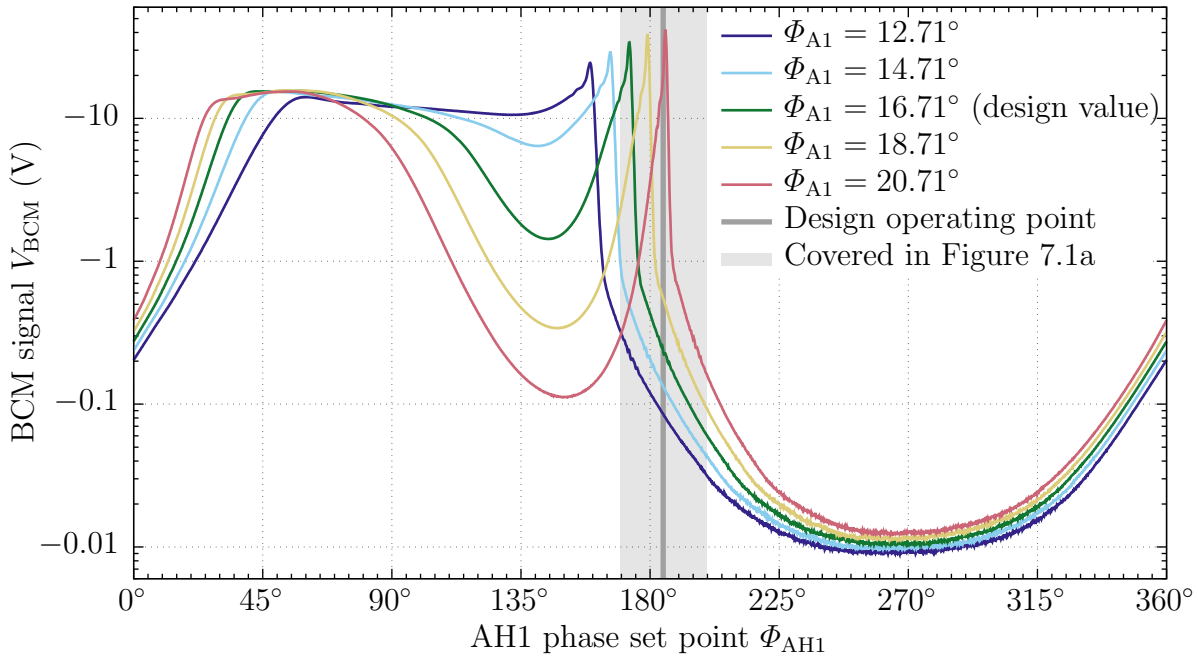

(b) As a function of the phase set point of AH1 for different values of the A1 phase.

Figure 7.1: Simulation of the signal of the bunch compression monitor located immediately upstream the magnetic chicane of the second bunch compressor for a bunch charge of 500 pC. The design operating point for this charge is $\Phi_{A1} = 16.71°$ and $\Phi_{AH1} = 184.54°$ [FZL+13, p. 8]. The V_{BCM} axis is reversed for better readability.

A1 and AH1 phase changes. This observation can be explained by the relation of the operating frequencies of the two accelerating modules: while A1 runs at $f_{\mathrm{A1}} = 1.3\,\mathrm{GHz}$, AH1 uses $f_{\mathrm{AH1}} = 3f_{\mathrm{A1}} = 3.9\,\mathrm{GHz}$ (see section 1.1).

The change of the peak position is also visible in Figure 7.1b. Here, the simulated BCM signal is plotted over the full phase range of AH1 for five discrete values of the A1 phase set point around the design value. The distance between the positions of adjacent peaks is 6°, which equals three times the A1 phase increment used for the different data lines.

Besides shifting the peak position, the A1 phase set point significantly influences the course of the BCM signal. It affects the value and slope at the design operating point as well as its behaviour in the range between 70° and the peak position. For larger values of Φ_{A1} a significant signal drop occurs in this region, which is less pronounced for smaller A1 phases.

In addition to being highly non-linear, the BCM signal spans a large dynamic range. For the bunch charge of 500 pC used in the simulations, it covers almost four orders of magnitude over the full phase range of AH1. Taking the wide charge span from 20 pC to 1 nC for the operation of the European XFEL into account, an overall dynamic range of seven orders of magnitude is estimated for the BCM signal at this station. For that reason, the BCM detector box comprises several means for attenuating and adjusting the signal amplitude, such as multiple coherent diffraction radiation (CDR) paths for detectors of different sensitivities, motor stages for changing the CDR focus spot size on the detector and motorised filters which can be inserted into the CDR beam path (see section 4.1).

7.2 Bunch Length and Compression

In addition to the overall length of the electron bunch, the longitudinal current profile significantly influences the BCM signal. At FLASH and the European XFEL, bunch profile measurements can be performed with the help of dedicated diagnostics systems. They make use of travelling-wave transversely deflecting structures (TDS), kicker magnets and off-axis scintillator screens installed at various locations of the accelerator [Yan16].

At the European XFEL, those devices are located in the diagnostics sections of the main accelerator and of the injector. In the main linac, TDS stations are installed downstream the magnetic chicanes of the final two bunch compressors (BC1 and BC2) in close vicinity to the BCMs. This arrangement allows for a comparison of the signals of both detectors.

In order to analyse the correlation between the BCM and TDS readings, simulations using the framework presented in chapter 5 and measurements during machine studies at the European XFEL have been carried out. By changing the phase set point of the first main accelerating section (L1) in steps of 1°, the bunch length downstream the magnetic chicane of the third bunch compressor (BC2) has been varied. For every L1

phase setting, a bunch length measurement using the TDS has been performed, while the BCM signal has been averaged over 50 single-bunch macropulses.

The results are shown in Figure 7.2. For the measurement data, the x error bars indicate the TDS resolution of 100 fs and the error bars in y direction represent the standard deviation of the individual BCM readings. In order to account for signal attenuation effects which are not included in the simulations, the respective curves have been scaled for plotting (q.v. page 97).

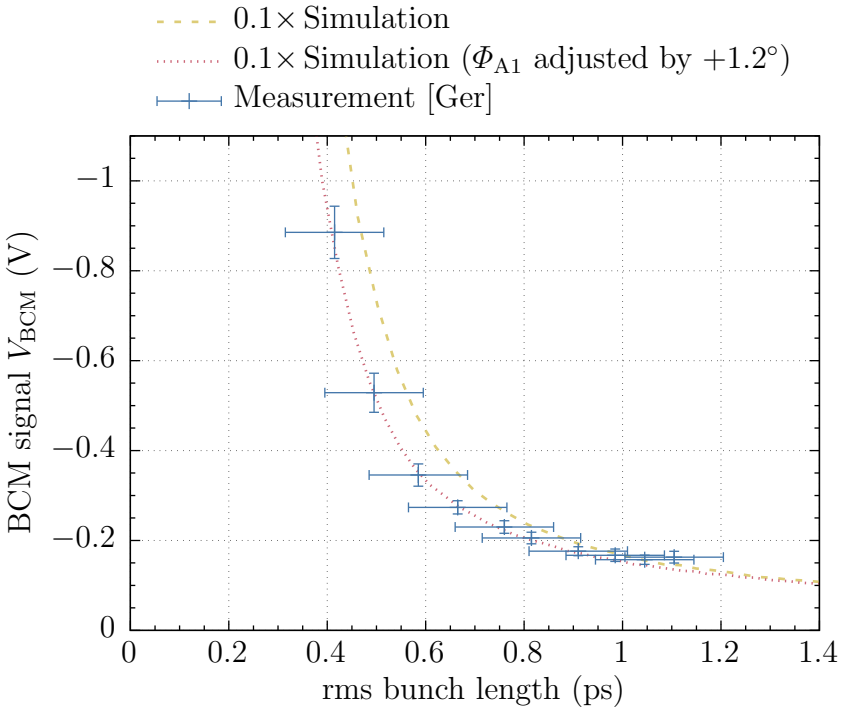

Figure 7.2: Simulation and measurement of the rms bunch length and the BCM signal downstream the magnetic chicane of the third bunch compressor at the European XFEL with a bunch charge of 500 pC when varying the phase set point of the first main accelerating section in steps of 1°. The V_{BCM} axis is reversed for better readability.

The simulation and measurement results are in good agreement: for shorter bunches, the absolute value of the BCM signal increases due to the reduced boundary wavelength of the coherent diffraction radiation. However, a systematic horizontal offset is visible between both data sets (although still within the error bars), with the simulation overestimating the bunch length compared to the measurement results. The discrepancy vanishes when the A1 phase is adjusted by 1.2° in the simulations. This correction is a realistic assumption as the experiment has been performed in the commissioning phase of the European XFEL, during which the absolute phase of the accelerating modules was only known with a precision of up to a few degrees.

For long bunches, the measured BCM signal appears to be bounded, while the simulations indicate it getting weaker with increasing bunch length. In this regime, the influence of the A1 phase set point correction vanishes.

7.3 Feedback Response Matrix

As it has been shown in section 6.2 for FLASH, the feedback response matrix $\mathbf{R}$ describes the reaction of monitor readings M_i to small variations of actuator values A_j in linear order around the working point

$$\begin{pmatrix} \delta M_1 \\ \vdots \\ \delta M_m \end{pmatrix} = \mathbf{R} \begin{pmatrix} \delta A_1 \\ \vdots \\ \delta A_n \end{pmatrix} . \tag{7.1}$$

Relating to longitudinal beam-based feedback, the actuators are the amplitude and phase set points of the accelerating modules (see Figure 1.5 on page 16). The monitors are beam diagnostics measurements such as bunch arrival time and bunch compression at various locations along the machine (see Figure 2.5 on page 27 and Figure 2.7 on page 31). In the following, analytical calculations and simulations using the beam-based feedback framework introduced in chapter 5 are presented.

7.3.1 Bunch Arrival Time

For the analytical description of the bunch arrival time response, the same derivations as in section 6.2.1 apply, but using the European XFEL lattice and nomenclature (see section 1.3).

First Bunch Compressor

In contrast to FLASH, there are in total three dispersive sections between the third harmonic and the second fundamental accelerating modules at the European XFEL (see Figure 1.5 on page 16) [FZL+13][2]:

- the laser heater (LH, $R_{56,\mathrm{LH}} = 4.7\,\mathrm{mm}$),
- the injector dogleg (DL, $R_{56,\mathrm{DL}} = 30.1\,\mathrm{mm}$) and
- the first bunch compressor (BC0, $R_{56,\mathrm{BC0}} = 54.8\,\mathrm{mm}$ for a bunch charge of 500 pC).

The particle momentum at all three locations is the same: $p_{\mathrm{LH}} = p_{\mathrm{DL}} = p_{\mathrm{BC0}}$.

[2] In [FZL+13], a slightly different notation is used in which R_{56} is negative. In conformance with the derivations given in section 1.1, these values have been adjusted to have a positive sign.

Due to the linearity of Equation 1.6, the total arrival time change downstream the first bunch compressor (BC0) – and thus also immediately upstream the second bunch compressor (BC1) – is given by the sum of these contributions[3]

$$\delta t_{\mathrm{A,UBC1}} = \delta t_{\mathrm{A,LH}} + \delta t_{\mathrm{A,DL}} + \delta t_{\mathrm{A,BC0}} = -\frac{1}{c}\frac{\delta p_{\mathrm{BC0}}}{p_{\mathrm{BC0}}}\left(R_{56,\mathrm{LH}} + R_{56,\mathrm{DL}} + R_{56,\mathrm{BC0}}\right) . \quad (7.2)$$

In the interest of improving readability, the definition

$$R_{56,\mathrm{UBC1}} \coloneqq R_{56,\mathrm{LH}} + R_{56,\mathrm{DL}} + R_{56,\mathrm{BC0}} = 89.6\,\mathrm{mm} \quad (7.3)$$

is used in the following.

Like for FLASH, the nominal particle momentum at the magnetic chicane of the first bunch compressor is defined by the momentum of the particles emitted by the RF gun plus the momentum gain in the accelerating modules

$$p_{\mathrm{BC0}} = p_{\mathrm{Gun}} + \Delta p_{\mathrm{A1}} + \Delta p_{\mathrm{AH1}} = p_{\mathrm{Gun}} + \frac{|q|}{c}\left[A_{\mathrm{A1}}\cos(\phi_{\mathrm{A1}}) + A_{\mathrm{AH1}}\cos(\phi_{\mathrm{AH1}})\right] . \quad (7.4)$$

A and ϕ denote the amplitude and phase set point of the particular accelerating module in volts and radians with respect to the reference phase $\phi = 0$. The reference phase is defined such that particles traversing the cavities experience the maximum acceleration. $|q| = e$ is the absolute charge of a single particle.

AH1 decelerates the beam, as it is the case for ACC39 at FLASH. Because this scheme is already accounted for in the definition of the AH1 phase set point, unlike in Equation 6.4, the explicit addition of π is not needed in Equation 7.4. The momentum of the electrons emitted by the RF gun is slightly higher than for FLASH, $p_{\mathrm{Gun}} = 6\,\mathrm{MeV}/c$ [FZL+13, p. 2].

Equivalently to Equation 6.5, a momentum change δp_{BC0} is introduced by varying the amplitude or phase set points of the first fundamental and the third harmonic accelerating modules around the working point. The gun set point is kept constant. In linear approximation, the resulting momentum change of the particles in the magnetic chicane of the first bunch compressor reads

$$\begin{aligned}\delta p_{\mathrm{BC0}} &= \frac{\mathrm{d}p_{\mathrm{BC0}}}{\mathrm{d}A_{\mathrm{A1}}}\delta A_{\mathrm{A1}} + \frac{\mathrm{d}p_{\mathrm{BC0}}}{\mathrm{d}\phi_{\mathrm{A1}}}\delta\phi_{\mathrm{A1}} + \frac{\mathrm{d}p_{\mathrm{BC0}}}{\mathrm{d}A_{\mathrm{AH1}}}\delta A_{\mathrm{AH1}} + \frac{\mathrm{d}p_{\mathrm{BC0}}}{\mathrm{d}\phi_{\mathrm{AH1}}}\delta\phi_{\mathrm{AH1}} \\ &= \frac{|q|}{c}\big[\cos(\phi_{\mathrm{A1}})\delta A_{\mathrm{A1}} - A_{\mathrm{A1}}\sin(\phi_{\mathrm{A1}})\delta\phi_{\mathrm{A1}} \\ &\quad + \cos(\phi_{\mathrm{AH1}})\delta A_{\mathrm{AH1}} - A_{\mathrm{AH1}}\sin(\phi_{\mathrm{AH1}})\delta\phi_{\mathrm{AH1}}\big] .\end{aligned} \quad (7.5)$$

[3] The indices used here reflect the physical locations of the individual components: while the considered bunch arrival time monitor station is located immediately upstream (U) the second bunch compressor (BC1) – hence $\delta t_{\mathrm{A,UBC1}}$, the relevant particle momentum for the arrival time change is the one at the magnetic chicane of the first bunch compressor, p_{BC0}. Between the first and second bunch compressor, an accelerating section – but no further dispersive chicane – is located (see section 1.3). The acceleration only changes the particles' momentum, but not their arrival time, as their velocity is already very close to the speed of light ($v \approx c$).

Similarly to Equation 6.6, the analytical representation of the linear arrival time response matrix coefficients downstream the first bunch compressor with respect to the relative amplitude $\tilde{A} = \frac{A}{A_{\mathrm{WP}}}$ and the phase in degrees $\Phi = \frac{180^\circ}{\pi}\phi$ reads

$$\begin{aligned}\mathbf{R}(t_{\mathrm{A}})_{\mathrm{UBC1}} &= -\frac{R_{56,\mathrm{UBC1}}}{p_{\mathrm{BC0}}c}\left(\frac{\mathrm{d}}{\mathrm{d}\tilde{A}_{\mathrm{A1}}}, \frac{\mathrm{d}}{\mathrm{d}\Phi_{\mathrm{A1}}}, \frac{\mathrm{d}}{\mathrm{d}\tilde{A}_{\mathrm{AH1}}}, \frac{\mathrm{d}}{\mathrm{d}\Phi_{\mathrm{AH1}}}\right) p_{\mathrm{BC0}} \\ &= -\frac{|q|}{c^2}\frac{R_{56,\mathrm{UBC1}}}{p_{\mathrm{BC0}}}\Bigg(A_{\mathrm{A1}}\cos(\Phi_{\mathrm{A1}}), -\frac{\pi}{180^\circ}A_{\mathrm{A1}}\sin(\Phi_{\mathrm{A1}}), \\ &\qquad A_{\mathrm{AH1}}\cos(\Phi_{\mathrm{AH1}}), -\frac{\pi}{180^\circ}A_{\mathrm{AH1}}\sin(\Phi_{\mathrm{AH1}})\Bigg)\,.\end{aligned} \tag{7.6}$$

For the accelerator working point corresponding to a bunch charge of 500 pC [FZL+13]

$$\begin{aligned}A_{\mathrm{A1}} &= 153.47\,\mathrm{MV}\,, \quad \Phi_{\mathrm{A1}} = 16.71^\circ\,, \\ A_{\mathrm{AH1}} &= 23.49\,\mathrm{MV}\,, \quad \Phi_{\mathrm{AH1}} = -175.46^\circ\,,\end{aligned} \tag{7.7}$$

the resulting values are given in Table 7.1. The particle momentum in the magnetic chicane of the first bunch compressor at the working point is $p_{\mathrm{BC0}} = 130\,\mathrm{MeV}/c$. Figure 7.3 shows the phase space distribution of the bunch in the diagnostics section upstream BC1 at the nominal working point.

The analytical and simulation results are presented in Figure 7.4 together with the simulated bunch compression monitor (BCM) signal. For each sub-plot, all but one component of Equation 7.6 have been set to zero. The curves for the analytical solution

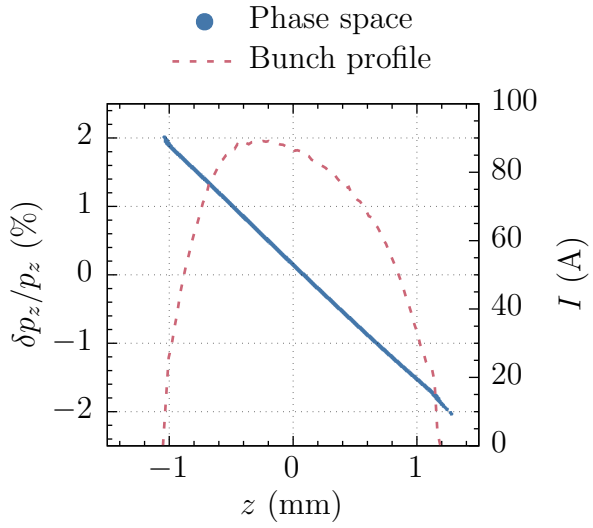

Figure 7.3: `RF Tweak` simulation of the phase space distribution of the electron bunch immediately upstream the magnetic chicane of the second bunch compressor of the European XFEL at the nominal working point.

Module	Amplitude $\left(\frac{\text{ps}}{\%}\right)$	Phase $\left(\frac{\text{ps}}{^\circ}\right)$
A1	−3.38	1.77
AH1	0.54	−0.07

Table 7.1: Analytical values of the linear arrival time response matrix coefficients for the first bunch compressor at the European XFEL for a bunch charge of 500 pC.

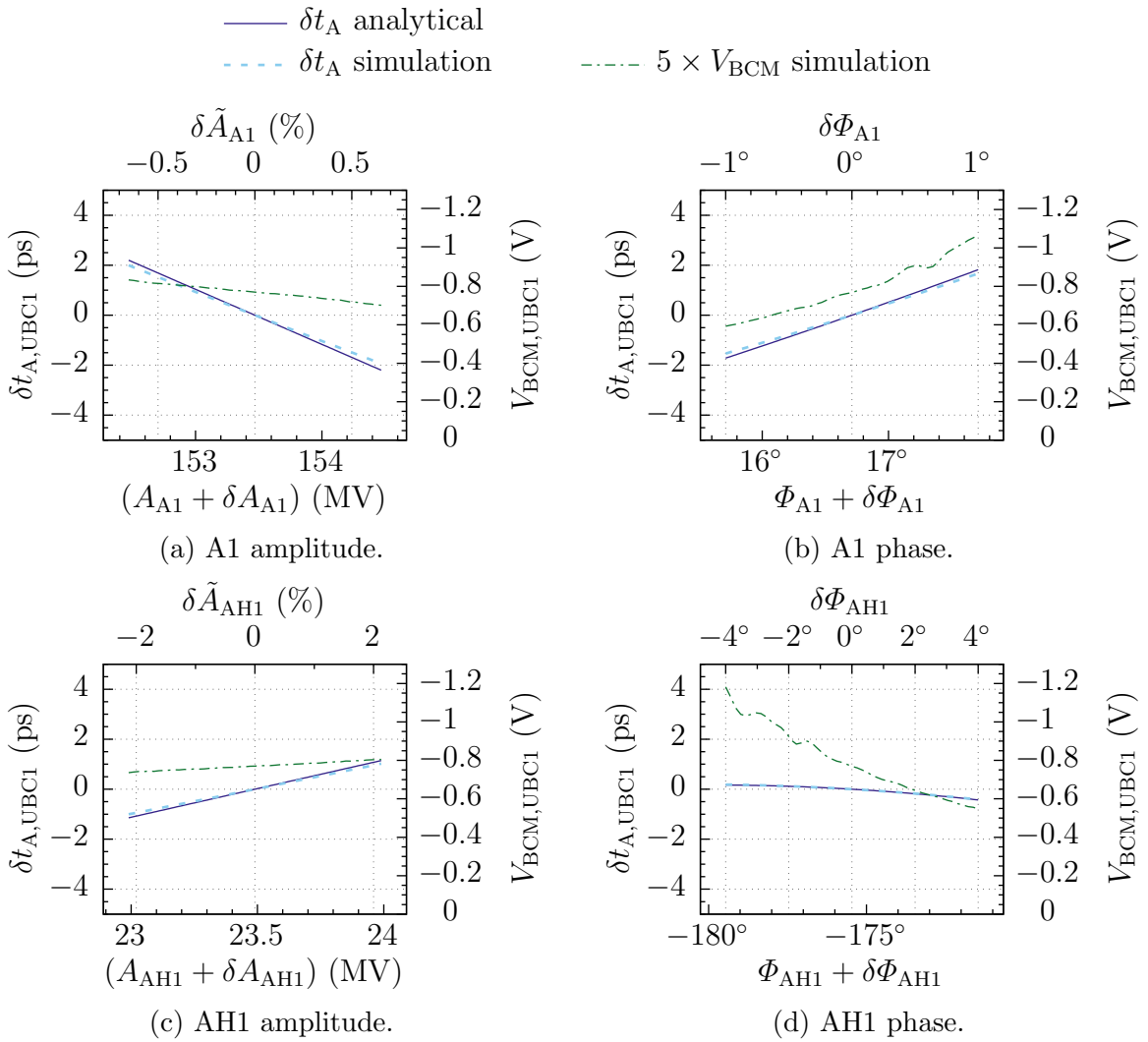

(a) A1 amplitude.

(b) A1 phase.

(c) AH1 amplitude.

(d) AH1 phase.

Figure 7.4: Analytical results and simulation of the bunch arrival time and bunch compression monitor signals downstream the first bunch compressor at the European XFEL as a function of the set point of A1 and AH1 for a bunch charge of 500 pC. The V_BCM axis is reversed for better readability.

and simulation results of the bunch arrival time are in good agreement, their slopes at the working point ($\delta = 0$) correspond to the values presented in Table 7.1. The slight discrepancy between the curves might be caused by the analytical description – unlike `RF Tweak` – neglecting higher order dispersion terms. The bunch compression monitor signal has been scaled in order to use the available data range.

Second Bunch Compressor

Similarly to Equation 7.4, the nominal particle momentum at the magnetic chicane of the second bunch compressor is defined by the momentum of the electrons in the first bunch compression chicane plus the momentum gain in the subsequent accelerating section

$$p_{\mathrm{BC1}} = p_{\mathrm{BC0}} + \Delta p_{\mathrm{L1}} = p_{\mathrm{BC0}} + \frac{|q|}{c} A_{\mathrm{L1}} \cos(\varphi_{\mathrm{L1}}) \,, \tag{7.8}$$

with $|q| = e$. Like for FLASH, arrival time changes downstream the first bunch compressor cause the electrons to traverse the subsequent accelerating modules at a different RF phase. As shown in section 6.1, a timing difference δt corresponds to a phase shift of $\psi = 2\pi f_{\mathrm{RF}} \delta t$, amounting to $0.47\,^\circ$/ps for the fundamental frequency of $f_{\mathrm{RF}} = 1.3\,\mathrm{GHz}$. This leads to a changed momentum gain of the particles in the subsequent accelerating section, which in turn affects the bunch arrival time and compression state downstream the next magnetic chicane.

In Equation 7.8, this effect is accounted for by using

$$\varphi_{\mathrm{L1}} \coloneqq \phi_{\mathrm{L1}} + \psi_{\mathrm{L1}} = \phi_{\mathrm{L1}} + 2\pi f_{\mathrm{RF}} \delta t_{\mathrm{A,UBC1}} \,. \tag{7.9}$$

φ_{L1} describes the effective phase at which the bunch gets accelerated in L1, considering the nominal phase set-point ϕ_{L1} and the timing change contribution $\delta t_{\mathrm{A,UBC1}}$ caused by a changed momentum in the first bunch compressor. $\delta t_{\mathrm{A,UBC1}}$ can be obtained from Equation 1.6 yielding

$$\varphi_{\mathrm{L1}} = \phi_{\mathrm{L1}} - 2\pi f_{\mathrm{RF}} \frac{R_{56,\mathrm{UBC1}}}{c} \frac{\delta p_{\mathrm{BC0}}}{p_{\mathrm{BC0}}} \,, \tag{7.10}$$

with δp_{BC0} given by Equation 7.5. For bunches with nominal momentum in the magnetic chicane of the first bunch compressor ($\delta p_{\mathrm{BC0}} = 0$), no phase adjustment occurs and $\varphi_{\mathrm{L1}} = \phi_{\mathrm{L1}}$.

A momentum change δp_{BC1} is introduced by varying the amplitude and phase set points of the first two fundamental and the third harmonic accelerating stations around the working point. The resulting momentum deviation of the particles in the magnetic chicane of the second bunch compressor at the design momentum ($\varphi_{\mathrm{L1}} = \phi_{\mathrm{L1}}$) has a similar structure to Equation 7.5, but with additional terms originating from Equation 7.10.

In linear approximation, it reads

$$\begin{aligned}\delta p_{\mathrm{BC1}} &= \sum_{\substack{X\in\{A,\phi\}\\ M\in\{\mathrm{A1,AH1,L1}\}}} \frac{\mathrm{d}p_{\mathrm{BC1}}}{\mathrm{d}X_M}\delta X_M = \delta p_{\mathrm{BC0}} + \sum_{\substack{X\in\{A,\phi\}\\ M\in\{\mathrm{A1,AH1,L1}\}}} \frac{\mathrm{d}\Delta p_{\mathrm{L1}}}{\mathrm{d}X_M}\delta X_M \\ &= \frac{|q|}{c}\big[\,(1+C_{\phi_{\mathrm{L1}}})\cos(\phi_{\mathrm{A1}})\delta A_{\mathrm{A1}} - (1+C_{\phi_{\mathrm{L1}}})\,A_{\mathrm{A1}}\sin(\phi_{\mathrm{A1}})\delta\phi_{\mathrm{A1}} \\ &\quad + (1+C_{\phi_{\mathrm{L1}}})\cos(\phi_{\mathrm{AH1}})\delta A_{\mathrm{AH1}} - (1+C_{\phi_{\mathrm{L1}}})\,A_{\mathrm{AH1}}\sin(\phi_{\mathrm{AH1}})\delta\phi_{\mathrm{AH1}} \\ &\quad + \cos(\phi_{\mathrm{L1}})\delta A_{\mathrm{L1}} - A_{\mathrm{L1}}\sin(\phi_{\mathrm{L1}})\delta\phi_{\mathrm{L1}}\big]\,.\end{aligned} \tag{7.11}$$

The coefficient

$$C_{\phi_{\mathrm{L1}}} = 2\pi f_{\mathrm{RF}}\frac{|q|}{c^2}\frac{R_{56,\mathrm{UBC1}}}{p_{\mathrm{BC0}}}A_{\mathrm{L1}}\sin(\phi_{\mathrm{L1}})$$

is a measure of the influence of the changed L1 phase operating point due to a different transit time through the magnetic chicane of the first bunch compressor. With $R_{56,\mathrm{UBC1}} = 89.6\,\mathrm{mm} > 0$ and $0 < \phi_{\mathrm{L1}} < \pi$ (see Equation 7.13), $C_{\phi_{\mathrm{L1}}}$ is positive. This means it increases the slope of the derivative of the particular component of δp_{BC1} with respect to the operating point of the accelerating modules upstream the magnetic chicane of the first bunch compressor. Data sets illustrating this effect are included in Figure 7.6. At the machine working point as given by Equation 7.7 and Equation 7.13, the coefficient value is $C_{\phi_{\mathrm{L1}}} = 5.93$.

The linear arrival time response matrix coefficients downstream the second bunch compressor (DBC1) – with respect to the *relative amplitude* and *phase in degrees* – read, similar to Equation 6.12,

$$\begin{aligned}\mathbf{R}(t_{\mathrm{A}})_{\mathrm{DBC1}} &= -\frac{R_{56,\mathrm{BC1}}}{p_{\mathrm{BC1}}c}\left(\frac{\mathrm{d}}{\mathrm{d}\tilde{A}_{\mathrm{A1}}},\frac{\mathrm{d}}{\mathrm{d}\Phi_{\mathrm{A1}}},\frac{\mathrm{d}}{\mathrm{d}\tilde{A}_{\mathrm{AH1}}},\frac{\mathrm{d}}{\mathrm{d}\Phi_{\mathrm{AH1}}},\frac{\mathrm{d}}{\mathrm{d}\tilde{A}_{\mathrm{L1}}},\frac{\mathrm{d}}{\mathrm{d}\Phi_{\mathrm{L1}}}\right)p_{\mathrm{BC1}} \\ &= -\frac{|q|}{c^2}\frac{R_{56,\mathrm{BC1}}}{p_{\mathrm{BC1}}}\Bigg(\begin{aligned}&(1+C_{\phi_{\mathrm{L1}}})\,A_{\mathrm{A1}}\cos(\Phi_{\mathrm{A1}}),\\ &-(1+C_{\phi_{\mathrm{L1}}})\,\frac{\pi}{180^\circ}A_{\mathrm{A1}}\sin(\Phi_{\mathrm{A1}}),\\ &(1+C_{\phi_{\mathrm{L1}}})\,A_{\mathrm{AH1}}\cos(\Phi_{\mathrm{AH1}}),\\ &-(1+C_{\phi_{\mathrm{L1}}})\,\frac{\pi}{180^\circ}A_{\mathrm{AH1}}\sin(\Phi_{\mathrm{AH1}}),\\ &A_{\mathrm{L1}}\cos(\Phi_{\mathrm{L1}}),\\ &-\frac{\pi}{180^\circ}A_{\mathrm{L1}}\sin(\Phi_{\mathrm{L1}})\Bigg)\,.\end{aligned}\end{aligned} \tag{7.12}$$

For the accelerator working point as given in Equation 7.7, in combination with the operating point of the second fundamental accelerating section [FZL+13]

$$A_{\mathrm{L1}} = 651.95\,\mathrm{MV}\,,\quad \Phi_{\mathrm{L1}} = 29.00^\circ\,, \tag{7.13}$$

Module	Amplitude $\left(\frac{\text{ps}}{\%}\right)$	Phase $\left(\frac{\text{ps}}{^\circ}\right)$
A1	−2.43	1.27
AH1	0.39	−0.05
L1	−1.36	1.31

Table 7.2: Analytical values of the linear arrival time response matrix coefficients for the second bunch compressor at the European XFEL for a bunch charge of 500 pC.

the resulting values are presented in Table 7.2. The particle momentum in the magnetic chicane of the second bunch compressor at the working point is $p_{\text{BC1}} = 700\,\text{MeV}/c$. Figure 7.5 shows the phase space distribution of the bunch downstream BC1 at the nominal working point.

The analytical and simulation results are presented in Figure 7.6 together with the simulated bunch compression monitor (BCM) signal. For each sub-plot, all but one component of Equation 7.12 have been set to zero. The slopes of the analytical curves at the working point ($\delta = 0$) correspond to the values presented in Table 7.2. The discrepancy between the analytical and simulation results might be caused by the analytical description – unlike `RF Tweak` – neglecting higher order dispersion terms. The bunch compression monitor signal has been scaled in order to use the available data range.

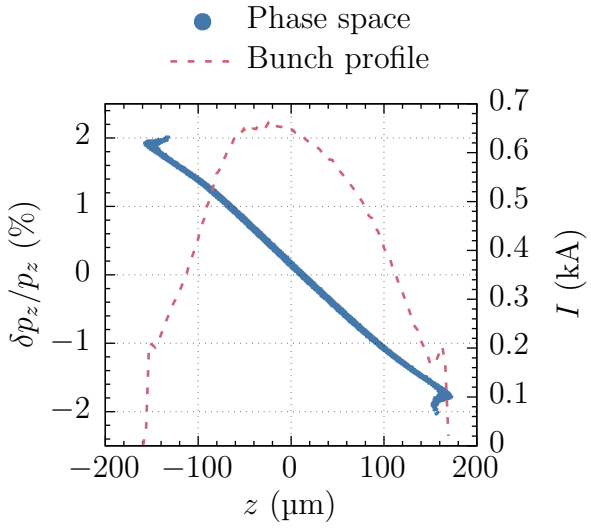

Figure 7.5: `RF Tweak` simulation of the phase space distribution of the electron bunch downstream the magnetic chicane of the second bunch compressor at the European XFEL at the nominal working point.

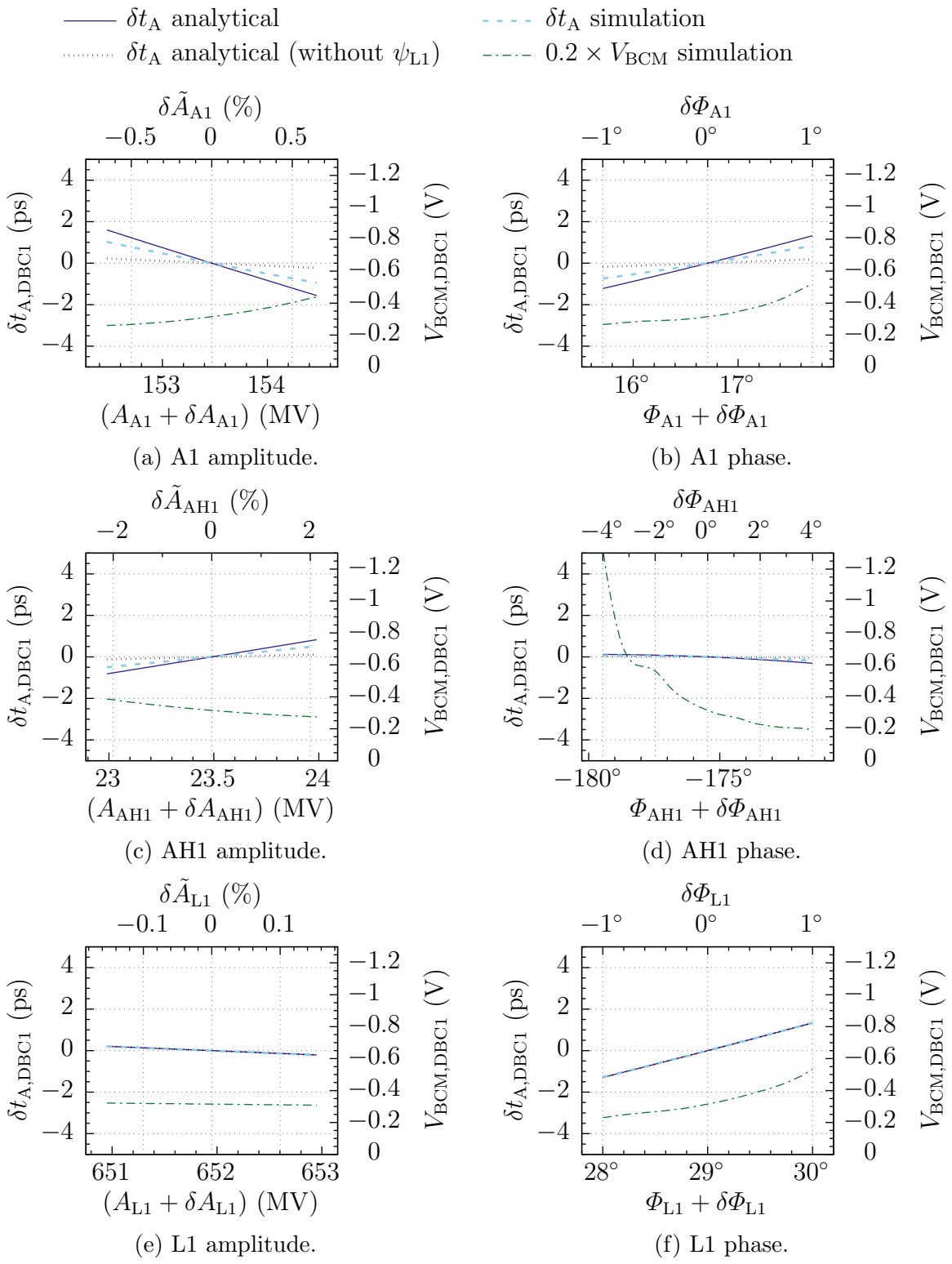

(a) A1 amplitude.

(b) A1 phase.

(c) AH1 amplitude.

(d) AH1 phase.

(e) L1 amplitude.

(f) L1 phase.

Figure 7.6: Analytical results and simulation of the bunch arrival time and bunch compression monitor signals downstream the second bunch compressor at the European XFEL as a function of the set point of A1, AH1 and L1 for a bunch charge of 500 pC. The V_BCM axis is reversed for better readability.

The dotted lines in Figure 7.6a to 7.6d represent the analytical arrival time when ψ_{L1} is not taken into account in Equation 7.9. For these data sets, the arrival time change is only caused by the changed particle momentum. The slopes of the curves are significantly smaller than for the true case. This implies that the contribution of the changed effective phase the bunch experiences in L1 is larger than the effect of the momentum variation itself. The fact that $C_{\phi_{\mathrm{L1}}} = 5.93 > 1$ in Equation 7.12 confirms this observation.

7.3.2 Bunch Compression

As shown in section 6.2.2 for FLASH, an analytical estimation of the bunch compression monitor signal is not feasible due to the frequency dependencies of the coherent diffraction radiation transmission line and the detector response, for which no analytical descriptions are available. Consequently, for this case only simulations – but no analytical curves – are presented.

Summary and Outlook

In the beginning of this thesis, a motivation for working on the field of longitudinal diagnostics for beam-based intra bunch-train feedback (BBF) at high repetition rate free-electron laser (FEL) facilities has been given. Possible options for improvements have been identified and questions to be addressed have been defined. During the course of this work, the different topics have been assessed and the obtained results have been discussed.

An upgrade of the electro-optical unit for the bunch arrival time monitors (BAMs) at FLASH and the European XFEL in order to improve the measurement resolution for small bunch charges and enable the detection of bunches from different sub-macropulses has been presented. The signal flow and the interconnection of the involved subsystems have been described. The individual components have been characterised and their suitability for the intended use has been verified with measurements.

The thermal concept of the unit in order to reduce the influence of environmental disturbances on the measurement accuracy has been explained. The employed stabilisation scheme consisting of an insulated and actively temperature stabilised compartment housing sensitive components in combination with Peltier elements and a digital temperature controller has been described. It has been shown with measurements in a climate chamber that this setup is able to compensate external temperature changes and fulfils the requirement of limiting short-term fluctuations inside the thermo box to below 10 mK (rms).

Several units have been assembled, installed at the respective locations along the accelerator and commissioned. A procedure for the assembly and alignment of the optical delay stages has been developed and further refined in the process. It is documented in Appendix A. A camera software aiding in the alignment procedure with the help of user-defined markers and a lever mechanism indicating the optimal position of the laser beam has been developed. In the meantime, this program has become a standard tool in other laboratories as well.

The bunch compression monitor (BCM) for the European XFEL has been presented. The layout of the measurement stations and the signal path from the diffraction screen to the detectors have been described. The dependency of the spectral intensity of the diffraction radiation on the electron beam energy and the hole diameter of the diffraction screen has been simulated.

It has been demonstrated that the placement of the first BCM at the European XFEL downstream (instead of upstream) the first main accelerating section leads to a significantly higher spectral intensity and an extension of the spectrum towards shorter

wavelengths due to the larger electron beam energy, increasing the sensitivity to short structures in the longitudinal bunch profile. Based on the individual constituents of the signal genesis – the longitudinal profile of the electron bunch, the radiation generation at the diffraction screen and its transport to the detector as well as the spectral responsivity of the measurement system – start-to-end simulations of the BCM signal at all three compression stages of the European XFEL have been performed.

For the first time since the transition of the accelerator control and detector electronics from the legacy VME system to the MicroTCA standard at FLASH, the beam-based intra bunch-train feedback has successfully been reinstated at the first bunch compressor in the course of this work. It has been demonstrated that the intra-train arrival time jitter is reduced from 35 fs to 10 fs (in-loop) respectively from 44 fs to 22 fs (out-of-loop), significantly improving the beam stability.

The weighting parameters for the field and beam errors in the combined feedback scheme have been scanned and an optimal setting ensuring stable operation while minimising the intra-train arrival time jitter has been found. Interferences between different regulation systems – such as the feedforward set point of the accelerating station competing with the intra-train feedback due to a shifted machine operating point caused by drifts – have been identified and possible solutions have been discussed.

Since then, the beam-based intra bunch-train feedback has become a frequently requested functionality which is by now routinely employed during user experiments. This rapid development points out the significance of this achievement. The weighting parameters for the field and beam errors are adjustable by the operators and with scripts through the standard machine control system interface. Additional tools for monitoring and tuning the feedback performance have been created.

The influence of single cavity phases of the first accelerating module on the time-of-flight of the bunches if the particles are not yet ultrarelativistic has been studied with simulations and measurements at FLASH. This effect leads to a changed effective phase in the subsequent accelerating sections which results in a systematic error between the desired and actual working point. It has been shown that the timing change is largest for the first cavity due to the low beam energy at the entrance of the accelerating module. For the subsequent cavities, the effect is significantly reduced as the beam energy increases.

During the course of this work, several longitudinal diagnostics suited as monitors in beam-based feedback systems have been described: bunch arrival time, compression and synchrotron radiation monitor. These diagnostics have been implemented in the longitudinal particle tracking software `RF Tweak 5 GUI` for aiding in the setup and tuning of the machine and studying the influence of the accelerator working point on the measured quantities. For the BCMs, the spectral intensity at the detector locations has been simulated with `ThzTransport` for different diffraction screen hole diameters. The spectra and the responsivity of the pyroelectric sensor are available in the BCM module of `RF Tweak 5 GUI` via data files.

All implemented longitudinal beam diagnostics are accessible to scripting through an application programming interface (API). In addition, graphical interfaces for controlling the detector properties and reconstructing the single steps of the signal genesis have been created for the bunch compression and synchrotron radiation monitors and integrated into `RF Tweak 5 GUI`.

A beam-based feedback (BBF) simulations framework based on particle tracking with `RF Tweak 5 GUI` and the implemented longitudinal beam diagnostics has been developed for studying feedback schemes including the not analytically describable beam dynamics and detector characteristics. The system under investigation is constructed from building blocks and interconnecting signals. A versatile timing scheme allows for the description of different bunch patterns. Due to its modular design with a defined API for data exchange and status changes, the BBF simulations framework is easily expandable and can be maintained independently of the underlying tracking code.

The BBF simulations framework has been used in the course of this work for studying the bunch arrival time and compression feedback response for the first two bunch compressors of FLASH and the European XFEL. The arrival time response matrix has additionally been derived analytically in linear order. At FLASH, measurements of the bunch arrival time and compression response have been performed during machine studies. At the European XFEL, the correlation between the bunch length and the BCM signal has been determined with simulations and measurements.

Future Work

Complex systems – such as large accelerator facilities – are subject to continuous development and further refinement of the diverse subsystems. During the course of this work, several options for possible improvements of the employed methods and components have been identified and ideas for future developments have been presented. Some of those enhancements are already in the process of being implemented at the time of this writing.

The existing bunch arrival time monitors at FLASH will be upgraded to the new electro-optical unit described in chapter 3. In order to reach the final installation goal, five more BAMs will be installed at FLASH, resulting in a total number of eight stations. At the European XFEL, three more BAMs need to be installed to complete the goal of ten devices.

In order to further reduce the influence of environmental effects on the arrival time measurement, several possibilities for improving the detector setup arise. The RF cables transporting the pick-up signals from the beamline to the electro-optical unit are currently not temperature stabilised. By compensating external fluctuations, drifts in the order of 60 fs are expected to be avoided. In addition, the consideration of temperature changes in the arrival time calculation with the help of real-time measurements by the readout electronics or the device server as suggested in section 3.5.1 could eliminate

temperature-induced drifts of up to 20 fs occurring in the signal path outside of the thermo box.

For the evaluation of the measurement resolution and the observation of residual jitter or drift of a single detector station, out-of-loop and correlation measurements can be used. Both at FLASH and at the European XFEL, pairs of detector locations suited for this purpose are available. At FLASH, the two BAM stations downstream the magnetic chicane of the second bunch compressor installed up- and downstream of the final accelerating section can be used as soon as the BAM '15ACC7' is commissioned. At the European XFEL, the two stations up- and downstream the second main accelerating section between the magnetic chicanes of the second and third bunch compressor can be used. This applies to the bunch compression monitors installed at the same locations as well.

Two BAMs are installed in series downstream the final collimation section of the European XFEL. The optical reference for the first one is provided by the master laser oscillator located close to the injector, while the second one is supplied by the slave laser oscillator located in the experimental hall. This scheme allows for an evaluation of the detector timing stability including the optical reference distribution.

After its successful reinstatement in the course of this work, the beam-based intra bunch-train feedback at the first bunch compressor of FLASH has by now become a functionality routinely employed during user experiments. In order to further improve the beam stability, the implementation of a similar system at the second bunch compressor is currently being prepared.

The beam-based intra bunch-train feedback at the European XFEL needs to be commissioned and evaluated. It is expected that the experience gained at the first bunch compressor of FLASH will be of great value for the realisation at the European XFEL due to the large similarity of the structure and the relevant subsystems – low-level radio frequency (LLRF) controllers and longitudinal beam diagnostics – of both facilities.

The bunch pattern used at FLASH and the European XFEL comprising several sub-macropulses which can be accelerated with different settings in a long train (see section 1.2 and section 1.3) is at the time of this writing not yet supported by the intra-train feedback controller. For the studies shown in this thesis, only one sub-macropulse has been used. In order to make the intra bunch-train feedback available for multiple sub-macropulses, a possibility to define different set points within one bunch train must be implemented in the LLRF controller.

In section 6.3 the effect of the feedforward set point of the accelerating station competing with the intra-train feedback due to a shifted machine operating point caused by drifts has been explained. This results in a wrong momentum gain of the bunches at the end of the train. In order to avoid this effect, the feedforward set point needs to be adjusted to the BBF-induced vector sum level. Currently the machine operators perform this correction by hand. It could instead be implemented in the LLRF controller for better automation and reliability of the system.

The LLRF controllers support the use of BCM signals in addition to the BAM data for the BBF, allowing for a better regulation of the RF amplitude and phase based on beam diagnostics sensitive to different aspects of the longitudinal phase space. The communication between the BCM stations and the LLRF systems is yet to be implemented. The performance of the combined feedback scheme needs to be investigated.

A normal conducting cavity with high bandwidth has recently been installed upstream of the magnetic chicane of the first bunch compressor at FLASH. It is intended for fast arrival time feedback with the goal to further reduce the intra bunch-train jitter [PBB+17][Pfe18]. The commissioning and performance evaluation of this system are currently being carried out.

The BBF simulations framework presented in chapter 5 supports the inclusion of the LLRF system and noisy signals into the model. These functions have not been used during the course of this work. It is of interest how they influence the feedback performance and compare with the measurement results shown in section 6.3.

The modular design of the BBF simulations framework allows for an easy integration of further beam diagnostics elements. As an example, `RF Tweak 5 GUI` already has a transversely deflecting structure (TDS) expert window available, however implemented in the core program and not yet included in the BBF simulations framework nor in the diagnostics windows supervisor scheme presented in section 5.5. Separating the TDS functionality from the core `RF Tweak` code would enable the use of this diagnostics for feedback simulations within the developed framework.

A Assembly and Alignment Procedure for the Optical Delay Stages of the New BAM Electro-Optical Unit

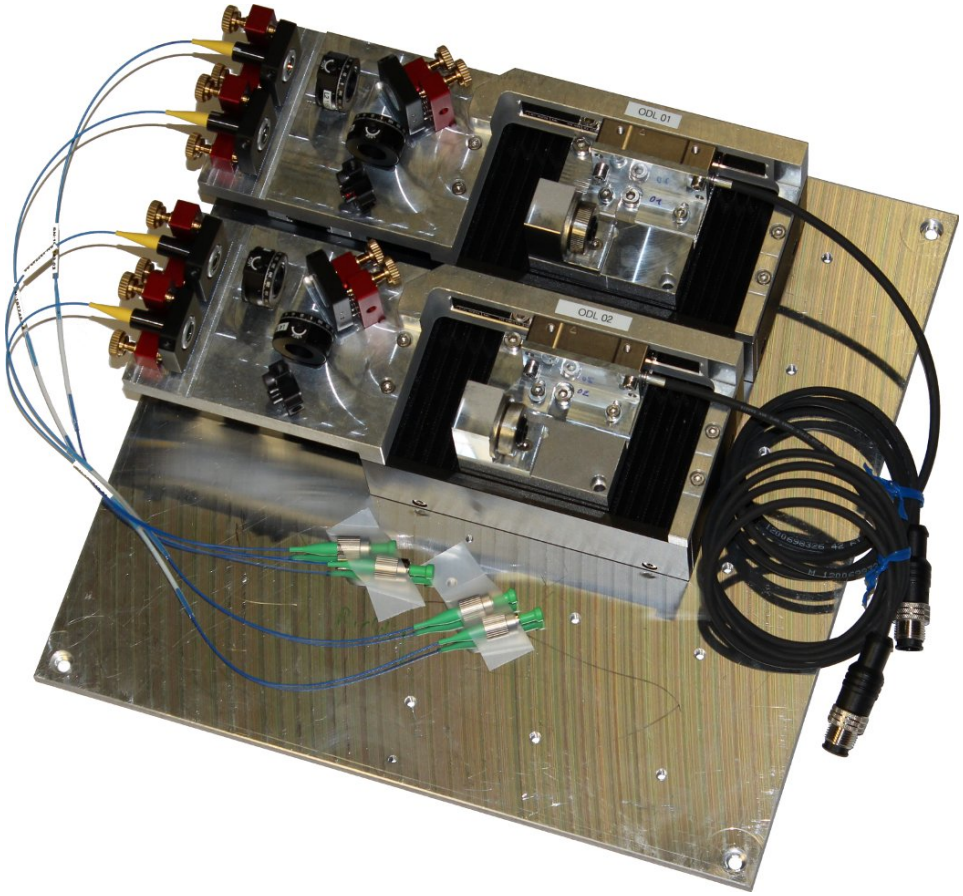

Figure A.1: Photograph of two optical delay stages, mounted on a common holder plate and pre-aligned before installation in the new BAM electro-optical unit. The holder plate supports up to three delay stages. Reproduced from Figure 3.9 on page 51.

A.1 Bill of Materials

Mechanical Parts

Component	Comment
Base plate	For mounting the delay stage(s) inside the BAM electro-optical unit
Motor stage body	Either long (70 mm travelling range) or short (40 mm travelling range) version
Optics holder plate	Plate mounted on top of motor stage body, supporting the optics components
Retroreflector holder	Including clamping fixture, washer and nut
Retroreflector holder plate	Adapter plate mounted on top of movable motor slide, supporting the retroreflector holder and the position encoder holder
Optical position encoder	
Position encoder holder	For mounting the optical position encoder on the retroreflector holder plate
Measurement tape	For optical position encoder

Mounting Material

Component	Amount	Purpose
Cylinder head screws M3×6	2	Optical position encoder on position encoder holder
Cylinder head screws M3×6 + washers	2	Position encoder holder on retroreflector holder plate
Countersunk head screw M3×8	1	Retroreflector holder on retroreflector holder plate
Cylinder head screws M3×12	2	Optics holder plate on motor stage body
Cylinder head screws M3×20	2	(see above)
Cylinder head screws M4×8	4	Motor stage body on base plate
(see above)	6	Optics components on optics holder plate
(see above)	2	Retroreflector holder plate on motor slide
Cylinder head screw M4×20 + washer	1	(see above)

Optics Components

All half-inch size, $\lambda = 1550\,\text{nm}$

Component	Amount	Comment
Radiant Dyes mount MNI-H-2-3021	3	For collimators and mirror(s)
Adapter ring for collimator mount	2	
Waveplate mount	2	
Mount for D-shaped mirror	1	
Retroreflector	1	
Silver coated mirror	1	(2 for double-pass configuration)
$\lambda/4$ waveplate	1	
$\lambda/2$ waveplate	1	
D-shaped mirror	1	

A.2 Devices and Tools Needed for Alignment

For Single-Pass Configuration

- CW laser ($\lambda = 1550\,\text{nm}$). The use of a pulsed laser source has not proven practical: the alignment is hindered by unstable intensity over time.
- Alignment laser (pen-shaped laser pointer, $\lambda \approx 700\,\text{nm}$)
- Motor controller and cable
- USB camera, camera holder for mounting on motor slide, PC with beam profiler software, USB cable
- Power meter with measurement head for fibre-coupled laser
- Fibre inspector / cleaner
- Marker card(s) (the card with deep red coating has proven practical)
- Spacer foil for correct distance between optical position encoder and measurement tape

Additionally, for Double-Pass Configuration

Optionally, only needed if the double-pass configuration is desired (see section A.6)

- Half-inch mirror (silver coated) for returning the laser beam
- Mount for placing the camera outside of the delay stage
- Fibre-coupled optical circulator for separating incoming and returning laser beams

Additionally, for Verification of Need of $^{\lambda}/_{4}$ Waveplate

Optionally, only if the need of the $^{\lambda}/_{4}$ waveplate is to be demonstrated (solely for educational purposes; see section A.5.4)

- 2× Power meter with measurement heads for free-space laser
- Polarising beamsplitting cube
- Mounts for beamsplitting cube and power meter heads

A.3 Beam Profiler Camera Graphical Tool

During the alignment procedure of the optical delay line (ODL), a camera is used for observing and tuning the pointing stability of the laser beam. This is realised by recording the laser spot position and shape during movements of the motor stage and adjusting the mounts of the optical components according to the procedures described in this chapter (q.v. section 3.3.1). In order to facilitate this process, a computer software for displaying and analysing the live camera image has been developed during the course of this work. It additionally provides alignment aid with the help of user-defined markers.

Figure A.2 shows a screenshot of the software together with a control system panel for the motor interface used during the alignment process of an optical delay stage. The tool is designed in a modal way, using different windows with specific purposes. The main window displays a live picture of the laser spot on the camera. The current beam position is marked with light blue cross-hairs. An information field presents constantly updated beam characteristics such as the centroid position, size and orientation.

A separate settings window provides control over the display and data evaluation properties. It can be used for defining markers for measurement and alignment purposes. These are shown in the camera window as red (currently selected) and yellow (all other) cross-hairs. The distance between the laser spot position and the currently selected marker is displayed in the information field among the beam parameters and updated in real time.

The markers can be used as control points for defining a lever with an adjustable scaling ratio as an alignment help (see section A.5.1.4 and section A.6.2). In order to distinguish between multiple markers, they can be assigned custom names in the settings window. Old markers can be deleted or updated if their reference position has changed.

The beam centroid can be traced for visualising its position change during movements of the motor stage. The trace colour and optional fading time are configurable via the settings window. For archiving purposes, the trace data can be written to a user-defined file. Due to the modular structure of the tool, it is very easy to implement further beam diagnostics and functionalities.

The software supports multiple cameras connected to the computer. It prompts the user at start-up for choosing one from a list of auto-detected devices. The modular

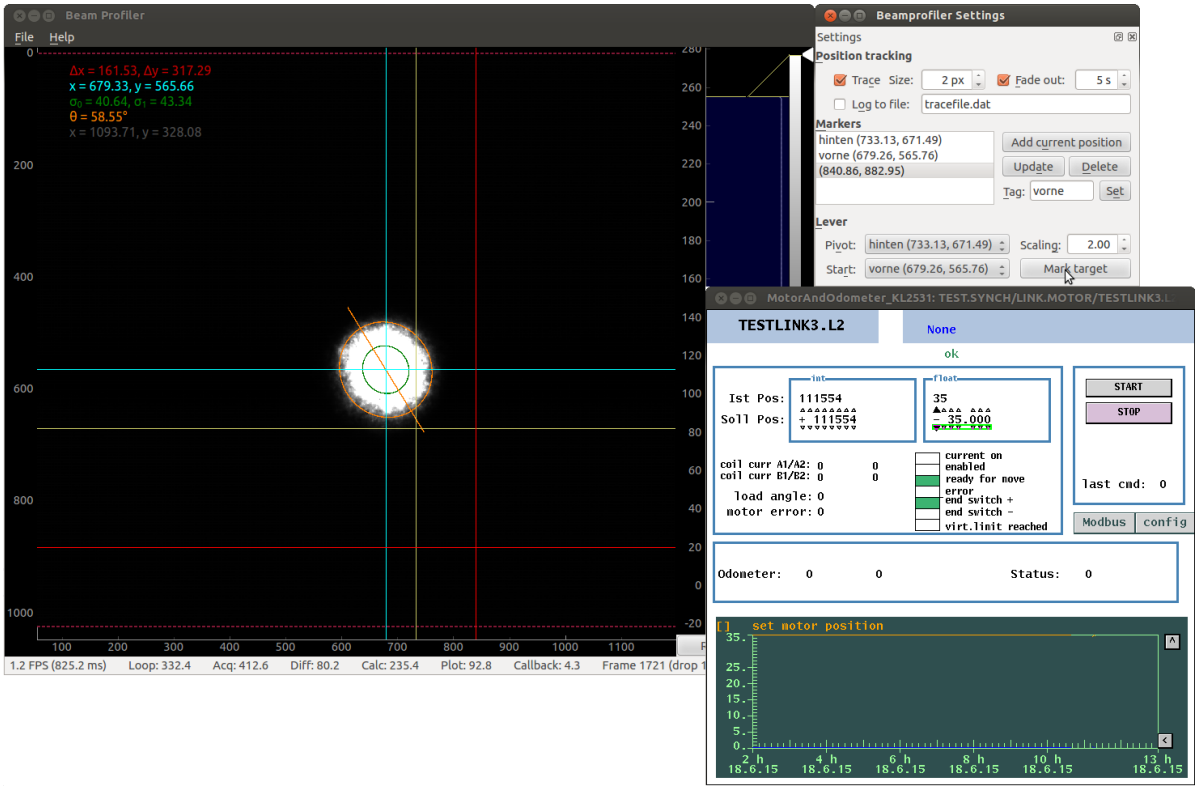

Figure A.2: Screenshot of beam profiler camera graphical tool during ODL alignment procedure. Camera window on the left side, settings and control window at the top right, `doocs` motor control panel (not part of the tool) at the bottom right.

design of the camera integration framework allows for an easy use of different camera types and facilitates the integration of new device classes into the tool.

The camera software is written in the `Python` programming language, using the `PyQtGraph` graphics library for fast live data display. The advantage of this tool kit is a very high drawing and updating speed compared to other frameworks, resulting in a higher achievable frame rate and near real-time updates. This significantly reduces the delay between adjustments of the optical components and the effects being visible on the computer screen, making the overall alignment process much more fluent. Support for zooming and panning as well as different colour maps for the visualisation of the laser beam in the main window are built in.

A.4 Assembly Considerations

The performance of the delay stage is largely affected by the positioning and alignment accuracy of all optical and mechanical components. When mounting the parts, it is important to take care not to block the beam path and to align them at their respective stop edges.

A.4.1 Positioning Tolerances

The manufacturing tolerances of all machined parts have been chosen liberally in order to provide some room for components imperfections and to allow for a coarse pre-alignment. Nonetheless, the positioning tolerances and aperture sizes of all mechanical and optical components are relatively stringent.

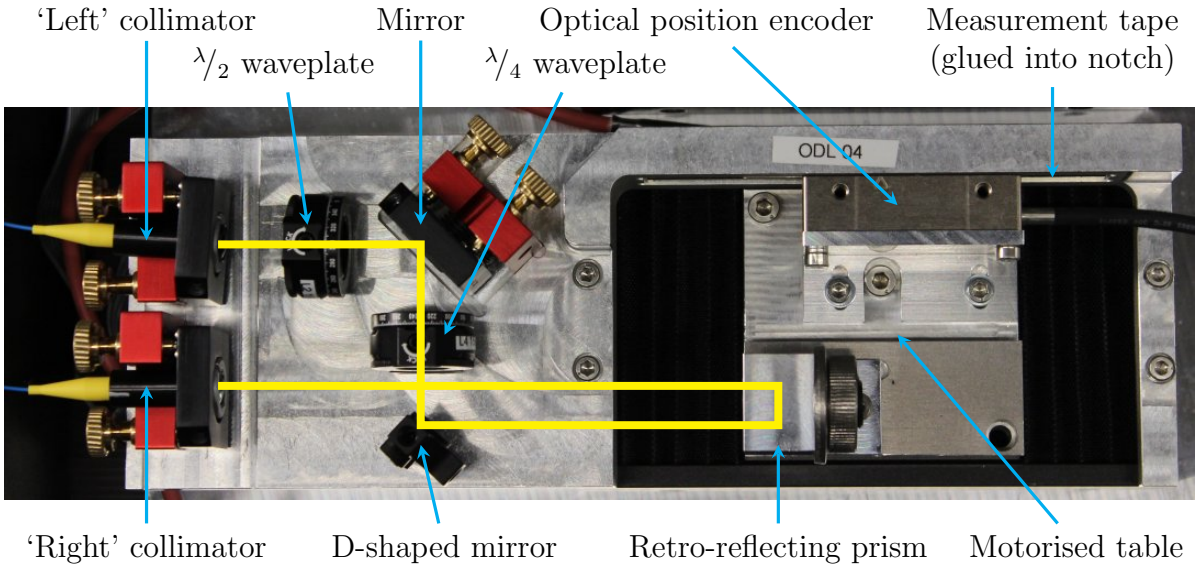

Figure A.3: Optical path through the delay stage (single-pass configuration). Adapted from Figure 3.10 on page 52.

In order for the laser beam to be able to pass through the delay stage (see Figure A.3), all parts must be fitted into place and aligned to the correct stop edges. Otherwise, even displacements of sub-millimetre order can lead to the beam being cut or blocked due to the multiple folding of the optical path within the system. The empirically determined alignment considerations for the particular components are:

Optics holder plate on top of motor stage body Twist counter-clockwise (seen from top), but take care that the retroreflector holder (respectively the camera holder during alignment) does not chafe on it when positioned at the near end (close to the collimators).

Collimator holder close to the $\lambda/2$ waveplate ('left' collimator) Align at stop edge pointing away from motor slide and laterally push to the right (towards other collimator).

Collimator holder close to the retroreflector ('right' collimator) Align at stop edge pointing away from motor slide and laterally push to the right (away from other collimator).

D-shaped mirror Align between frontal and rear stop edges, in the way that the beam hits the mirror centre (after aligning the right collimator). No lateral stop edge available. If necessary, correct the angular orientation with the fine adjustment pliers.

Half-inch mirror Align holder at rear stop edge pointing away from the waveplates, and laterally at stop edge pointing towards the motor slide (so the movable holder part has play).

$\lambda/2$ and $\lambda/4$ waveplates Align at stop edge pointing away from the degrees-labelled annulus. The orientation and lateral alignment is uncritical.

Measurement tape for optical position encoder Glue into according notch of optics holder plate.

Retroreflector holder plate on motor slide Push in direction of position encoder, taking care that the aluminium plate does not chafe on the side of the stage when driving the motor (this would lead to lateral forces and positioning imprecision).

Optical position encoder Mount only after retroreflector holder plate is finally mounted on the movable motor slide. Use the spacer foil and align parallel to the driving direction of the stage.

Retroreflector on holder plate Align at rear stop edge and lateral stop edge in direction of position encoder. When mounting the retroreflector in the holder, take care of the correct orientation as shown in section A.4.2.

A.4.2 Retroreflector Orientation

The retroreflector possesses three orthogonal faces and edges, which appear as $2 \times 3 = 6$ virtual faces and edges due to the reflection of each edge in the opposite face. In order to avoid aberrations, both the incoming and returning beams should lie on one of the six virtual faces. The position of the returning laser beam is a point reflection of the entering beam with respect to the retroreflector's centre. Because the path of the laser lies in the horizontal plane, this means that the retroreflector should be mounted in one of the ways shown in Figure A.4a.

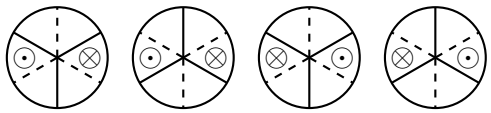

(a) Good retroreflector orientations. The laser beam lies entirely on the virtual faces. Two of the virtual edges are aligned perfectly vertically.

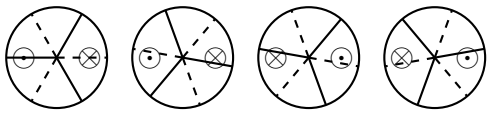

(b) Examples of bad retroreflector orientations. The laser beam hits the mirror edges.

Figure A.4: Possible ways of retroreflector mounting (view from collimators). The solid and dashed lines represent the real and virtual edges separating the 6 virtual mirror faces. The vectors represent the incoming (⊗) and reflected (⊙) laser beam.

A.5 Alignment for Single-Pass Configuration

A.5.1 Alignment of Right Collimator Mount and Motor Slide

A.5.1.1 Preparation

1. Drive motor slide to the far position (away from collimators)
2. Make sure the adjusting screws of the optics mounts are not at the limit and have some play in both directions
3. Fix right collimator in mount using adapter ring
4. Make sure that the output of the CW laser is switched off before handling optical fibres
5. Clean fibre connectors, connect CW laser to right collimator and switch on

A.5.1.2 Coarse Alignment Using Marker Card

1. Bring incoming and returning from retroreflector laser beam to roughly the same height, using marker card and vertical adjustment screw of collimator mount
2. Adjust incoming and returning from retroreflector laser beam to run approximately parallel, using marker card and horizontal adjustment screw of collimator mount

A.5.1.3 Mounting the Camera

1. Reduce output power of CW laser to minimum ($\approx 4\,\mathrm{mW}$) to protect camera
2. Switch off output of CW laser to prevent any uncontrolled reflections during mounting of components

3. Replace retroreflector holder plate on motor slide with camera holder for fine adjustment
    - Make sure the camera holder plate does not chafe on the side of the stage when driving the motor (this would lead to lateral forces and positioning imprecision)
4. Switch on output of CW laser

A.5.1.4 Fine Adjustment Using Camera

Important: After moving the motor slide, always wait for the camera image to settle down. This can take some seconds, depending on the motor driving speed and camera frame rate.

1. Check that the motor slide is at the far position (away from collimators)
2. In the camera software set marker at current position, optionally label it 'far' (or update existing 'far' marker)
3. Drive motor slide to the near position (close to collimators)
4. Set marker at current position, optionally label it 'near' (or update existing 'near' marker)
5. Make lever using 'near' marker as fulcrum and 'far' marker as start with ratio (see section A.7.2 for details on ratio calculation) of
    - 2 for the long (70 mm travelling range) stage version
    - 3.5 for the short (40 mm travelling range) stage version
6. Drive motor slide to the far position (away from collimators) to increase the sensitivity to angular misalignment
7. Bring laser beam to marker target using adjustment screws of right collimator mount
8. Repeat until result is satisfactory, iteratively adjust lever ratio if necessary

Goal: Less than 10 px (50 µm) fluctuation of laser position over the whole travelling range of the delay stage

The right collimator is now finally aligned. **Do not touch any more!**

A.5.2 Pre-Alignment of Half-Inch Mirror

1. Switch off output of CW laser to prevent any uncontrolled reflections during mounting of components

2. Replace camera holder on motor slide with retroreflector holder plate, taking into account the alignment considerations given in section A.4.1

3. Check that the motor slide is at the far position (away from collimators) to increase the sensitivity to angular misalignment

4. Fix left collimator in mount using adapter ring

5. Disconnect CW laser from the right collimator, clean fibre connectors and connect it to the left collimator

6. Connect alignment laser (pen-shaped laser pointer) to right collimator

7. Switch on alignment laser and check that the beam returning from the retroreflector hits the D-shaped mirror centrally (carefully correct lateral position of D-shaped mirror if necessary)

8. Use adjustment screws of half-inch mirror mount to bring the alignment laser spot to the centre of the left collimator

A.5.3 Coarse Alignment of Left Collimator and Half-Inch Mirror

1. Switch on output of CW laser

2. Use marker card to check overlap of the two beams
   - Increase output power of CW laser to maximum to be able to shine through marker card
   - Let CW laser illuminate the back side of the card and shine through it
   - Let alignment laser illuminate the front side of the card

   $\Rightarrow$ Both laser spots are visible on the front side of the card

3. Bring both laser beams (close) to overlap at two positions in the beam path

   Note: The two laser beams don't have to be brought to *perfect* overlap. It is sufficient if the beam path is roughly aligned so the laser is not blocked by any aperture and all optical components (mirrors, collimators) are hit by the beam. The coupling will be optimised in a later step using the power meter.

- **Far target** in front of right collimator: align using **far knob**: half-inch mirror mount
- **Near target** in front of D-shaped mirror: align using **near knob**: left collimator mount
- **Repeat** iteratively

A.5.4 (Optional) Verify that the $\lambda/4$ Plate is Needed and Adjust it

Note: This part is optional. During alignment of the delay stage prototype it was already verified (using the procedure described in section A.7.1) that the $\lambda/4$ waveplate is indeed needed. However, it has no influence on the alignment of the system and is therefore not considered further here. The interested reader is referred to section A.7.1 for a detailed description.

A.5.5 Fine Alignment of Half-Inch Mirror and Left Collimator

A.5.5.1 Preparation

1. Switch off the output of the CW laser to prevent any uncontrolled reflections during mounting of components
2. If not done during the course of section A.5.4:
   - Switch off alignment laser and disconnect it from right collimator

   Otherwise:
   - Re-insert right collimator into mount
3. Clean fibre connectors, connect fibre-coupled power meter to right collimator
4. Verify that power meter is set to $\lambda = 1550\,\mathrm{nm}$
5. Switch on output of CW laser

A.5.5.2 In-Coupling Optimisation

1. Optimise in-coupling by adjusting the following knobs and watching the power level increase
   - Half-inch mirror (both axes)
   - $\lambda/4$ waveplate and $\lambda/2$ waveplate
   - Left collimator (both axes)

   $\Rightarrow$ Repeat iteratively until (local) optimum is reached

2. 'Walking': systematic optimisation of individual axes

   You need: two hands for touching two knobs simultaneously

   a) Choose an axis: horizontal or vertical
   b) Choose a knob (half-inch mirror or left collimator)
   c) Choose a scanning direction for this knob (forward or backward)
   d) Turn knob in scanning direction by a small amount with one hand
   e) Use other knob of the same axis with other hand to scan back and forth for finding maximum power level
   f) Turn first knob further in scanning direction by a small amount
   g) Repeat scanning other knob for finding maximum power level
   h) Compare maximum levels found at both positions of first knob
   i) Decide if direction was correct (maximum increased) or not
      ⇒ Keep or decide to change direction
   j) Repeat steps 2d to 2i until optimal settings for this axis are found
   k) Repeat step 1 (in-coupling optimisation)
   l) Repeat steps 2b to 2k for other axis

   ⇒ Repeat iteratively until coupling is optimal for both axes

The half-inch mirror is now finally aligned. **Do not touch any more!**
The left collimator is now finally aligned. **Do not touch any more!**

A.5.6 Measure Coupling Uniformity over Travelling Range

1. Drive the motor to either end of travelling range
2. Set the motor target position to other end of travelling range, but don't start yet
3. Verify that the power meter is set to $\lambda = 1550\,\mathrm{nm}$
4. On the power meter: select *Measuring View* → *Tuning Graph* → *Exit*

   Note: This menu structure applies to the 'Thorlabs PM100D' power meter and might be different for other device types
5. Press *Start* on the power meter and start the motor
6. When the motor reaches the other end of the travelling range, press *Stop* on the power meter
7. Switch off the output of the CW laser (to create a safe situation for disconnecting)

8. Observe the measurement graph on the power meter: if the maximum and minimum power levels differ by less than 10 %, the alignment is ok. If not, start over!

The delay stage is now **finally aligned** for single-pass operation (laser beam entering and exiting through different collimators, passing it once). If this is the desired configuration, stop here.

A.6 Alignment for Double-Pass Configuration

To double the dynamic range of the delay stage, it is possible to replace the right collimator with a mirror. The laser beam then passes the stage twice, entering and exiting it through the same collimator. In this configuration it is necessary to split the incoming and returning beams outside of the stage using an optical circulator.

A.6.1 Dismount Right Collimator

1. Make sure the output of the CW laser is switched off to prevent any uncontrolled reflections during mounting of components
2. Disconnect power meter from right collimator
3. Remove right collimator from mount

A.6.2 Alignment of Half-Inch Mirror and Left Collimator

1. Mount camera outside of the delay stage, facing the right collimator
2. Reduce output power of CW laser to minimum ($\approx 4\,\mathrm{mW}$) to protect camera and switch on
3. Alignment using camera

   Important: After moving the motor slide, always wait for the camera image to settle down. This can take some seconds, depending on the motor driving speed and camera frame rate.

   a) Drive motor slide to the far position (away from collimators)
   b) In the camera software set marker at current position, optionally label it ‘far’
   c) Drive motor slide to the near position (close to collimators)
   d) Set marker at current position, optionally label it ‘near’
   e) Make lever using ‘near’ marker as fulcrum and ‘far’ marker as start with ratio (see section A.7.2 for details on ratio calculation) of

- 2 for the long (70 mm travelling range) stage version
- 3.5 for the short (40 mm travelling range) stage version

f) Bring laser beam to marker target using adjustment screws of left collimator mount ('near' knob)

g) Bring laser beam back to 'near' target using adjustment screws of half-inch mirror mount ('far' knob)

h) Repeat from step 3a until result is satisfactory, iteratively adjust lever ratio if necessary

Note: If this procedure requires a lot of iterations, increase the lever ratio. If increasing the lever ratio results in the lever target ending up outside of the picture area of the camera, the same result can be achieved by keeping the lever ratio factor constant and repeating steps 3f and 3g multiple times before going back to step 3a.

Goal: Less than 10 px (50 µm) fluctuation of laser position over the whole travelling range of the delay stage

A.6.3 Coarse Alignment of Mirror in Place of Right Collimator

1. Switch off output of CW laser to prevent any uncontrolled reflections during mounting of components
2. Install a half-inch mirror in the right collimator mount
3. Use marker card to check overlap of the two beams
   - Increase output power of CW laser to maximum to be able to shine through marker card
   - Let CW laser illuminate the back side of the card and shine through it
   - Let alignment laser illuminate the front side of the card

   ⇒ Both laser spots are visible on the front side of the card
4. Bring both laser beams to a close but not perfect overlap (**avoid sending reflected beam back into laser!**) using adjustment screws of right collimator (now mirror) mount

A.6.4 Fine Alignment of Mirror in Place of Right Collimator

1. Switch off output of CW laser to prevent any uncontrolled reflections during mounting of components
2. Disconnect CW laser from left collimator

3. Clean fibre connectors and
   a) Connect optical circulator to left collimator
   b) Connect CW laser to input of optical circulator
   c) Connect fibre-coupled power meter to output of optical circulator
4. Verify that power meter is set to $\lambda = 1550\,\mathrm{nm}$
5. Use adjustment screws of right collimator mount to maximise the measured intensity
6. Adjust $\lambda/4$ waveplate and $\lambda/2$ waveplate so that the measured intensity becomes maximum

The delay stage is now **finally aligned** in double-pass configuration.

A.7 Additional Checks and Calculations

A.7.1 Verification of Need and Adjustment of $\lambda/4$ Waveplate

This part is optional and takes place between section A.5.3 and section A.5.5. During alignment of the delay stage prototype it was already verified using the following procedure that the $\lambda/4$ waveplate is indeed needed. This step can safely be skipped without any negative impact on the performance of the delay stage. It is provided for educational purposes for the interested reader.

Two waveplates are installed in rotational mounts for optimising the degree and direction of polarisation. With the $\lambda/4$ plate, the polarisation can be adjusted to be purely linear in order to eliminate any elliptical component introduced by the retroreflector prism glass body and the mirrors. The $\lambda/2$ plate rotates the polarisation axis for optimal in- and out-coupling with the collimators.

For adjusting the waveplates, the two orthogonal polarisation directions have to be measured separately. This is done with the help of a free-space polarising beamsplitting cube. For this reason the right collimator must be removed temporarily.

1. Switch off output of CW laser to prevent any uncontrolled reflections during mounting of components

2. Switch off alignment laser and disconnect it from right collimator

3. Remove right collimator from mount

4. Place polarising beamsplitting cube outside of the delay stage so that the laser beam passing through the right collimator mount hits the cube centrally

5. At each exit arm of the beam cube, place one power meter with free-space head
   - Take care that the detector heads are set to the correct power range
   - Check that both power meters are set to $\lambda = 1550\,\mathrm{nm}$

6. Switch on output of CW laser

7. Adjust waveplates so that the reflected power becomes maximum and the transmitted power becomes minimum (or the other way around)

$\Rightarrow$ Verify that the result is much better when the $\lambda/4$ plate is also used

8. Continue with section A.5.5

A.7.2 Calculation of Lever Ratio

In section A.5.1.4, step 5, a lever is constructed using laser spot positions measured with a camera at two different positions of the movable slide. The aim of this procedure is to correct for angular misalignment in one shot. The displacement between the two measured positions is used together with distance information to calculate the correct beam position using the intercept theorem.

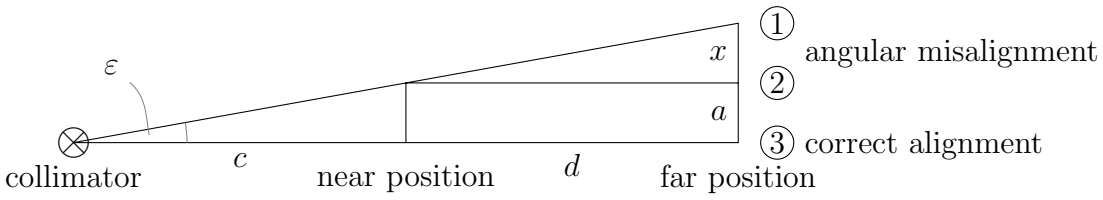

Figure A.5: Positions and distances used in lever calculation.

Only the angular orientation ε of the collimator mount is adjustable, the spatial position is fixed. The correct alignment is defined by the lateral displacement between the laser spots measured at the near and far positions being zero ($x = 0$). To achieve this goal, the collimator mount must be rotated by

$$\tan \varepsilon = \frac{a}{c} = \frac{x}{d}\,. \tag{A.1}$$

The target position of the laser spot on the camera is then given by point ③ in Figure A.5. To calculate the correct position, a class 1 lever defined by three points is constructed (see Figure A.5):

① **Start:** displacement caused by angular misalignment at far position,

② **Fulcrum:** displacement caused by angular misalignment at near position and

③ **Target:** correct alignment (no angular misalignment, no displacement).

The ratio of the two lever arms is defined by the fraction a/x, which equals c/d due to the intercept theorem (Equation A.1). When measuring the two quantities

c distance between collimator and near position and

d distance between near and far position (travelling range of the motor slide),

the lever ratio needed for a one-shot collimator alignment correction can be calculated

$$\text{Ratio} = \frac{c}{d}\,. \tag{A.2}$$

B Data Processing for Beam-Based Feedback Measurements at FLASH

In section 6.3, measurements of the intra bunch-train arrival time jitter reduction by beam-based feedback (BBF) with different settings of the field and beam weighting parameters are shown. For each parameter setting 600 macropulses (referred to as events) have been recorded, corresponding to one minute of data with a macropulse repetition rate of 10 Hz. Every macropulse comprised 100 bunches with a bunch repetition rate of 500 kHz.

Due to sporadic malfunction of several components used for data acquisition and accelerator control during the measurement shift, single events needed to be excluded from the analysis. In addition, plausibility checks and a safety margin around faulty events have been employed. The filtering has been applied to both the background (BBF off) and the sweep (BBF on with different feedback weighting parameter settings) data sets. Events falling into either of the following categories have been excluded from further processing:

1. Component malfunction
   a) **VME BAM missing data:** sometimes the number of bunches in the train reported by the old BAM electronics (used in the out-of-loop channel) was smaller than the actual number of bunches present in the machine; the bunch train appeared to be cut. In this case no arrival time information was obtained for the bunches in the tail of the train. This type of failure occurred only with this channel, all other diagnostics observed the full bunch train length for all recorded events. However, due to the missing arrival time information for the last bunches these events had to be discarded.

      → Criterion for event exclusion: number of bunches measured with the out-of-loop BAM is less than the requested bunch train length.

   b) **ACC23 vector sum jumps:** for several macropulses, the vector sum amplitude of the second accelerating station jumped by a large amount (several MV). This was a known issue at the time of the experiment which led to a drastically changed transit time of the electrons through the magnetic chicane of the second bunch compressor (downstream which the out-of-loop BAM is located) by $\approx 500\,\mathrm{fs/MV}$ according to Equation 6.12, while the experiment was interested in changes on the femtosecond level.

→ Criterion for event exclusion: ACC23 vector sum amplitude deviates from the mean value of all events with this setting by more than 1 MV.

c) **Low-latency link data corruption:** the fast data channel for sending the in-loop arrival time information from the BAM to the LLRF controller intermittently suffered from communication problems resulting in wrong data for the first few bunches. This was a known issue at the time of the experiment.

→ Criterion for event exclusion: received signal is zero for the first bunch.

2. Plausibility considerations

a) **Deviating ACC1 amplitude**

- Linked to item 1c: when the LLRF controller receives wrong data for the first bunches, the resulting feedback action changes the ACC1 amplitude by a large amount leading to flat top oscillations over the whole bunch train.

→ Criterion for event exclusion: ACC1 vector sum amplitude deviates from the mean value of all events with this setting by more than 0.15 MV either at the beginning (bunches 10 . . . 14) or at the end (last two bunches) of the train.

b) **Deviating in-loop BAM data**

- Linked to item 2a: when the ACC1 amplitude changes by a large amount (potentially even with oscillations over the bunch train), this is propagated to the in-loop and out-of-loop arrival time measurements.

→ Criterion for event exclusion: measurement deviates from the mean value of all events with this setting by either more than 250 fs within the first ten bunches or more than 500 fs within the last two bunches.

c) **Deviating out-of-loop BAM data**

- Linked to items 1a, 1b and 2a: this monitor suffered from intermittent data corruption resulting in missing arrival time information for the end of the bunch train. In addition, by being the farthest downstream element in the measurement setup this BAM observed all timing changes caused by instabilities of any of the upstream accelerating stations.

→ Criterion for event exclusion: measurement deviates from the mean value of all events with this setting by either more than 300 fs within the first ten bunches or more than 550 fs within the last two bunches.

3. **Safety margin:** One event immediately before and after filtered out events have been discarded as well in order to avoid side effects of imminent issues and allow the system to recover from incidents.

Table B.1 summarizes the number of events falling into each of the above categories over all measurements. Some events meet more than one criterion. Of course they have been excluded only once. On average, 23.7 (maximum: 50) events per feedback weighting parameter setting have qualified for being excluded from further processing.

Reason	Labelling in Figure B.1	Events per data point	
		On average	Maximum
1a	VME	0.1 (0.0 %)	2 (0.3 %)
1b	ACC23	0.3 (0.1 %)	2 (0.3 %)
1c	LLL	4.6 (0.8 %)	10 (1.7 %)
2a	ACC1	5.3 (0.9 %)	14 (2.3 %)
2b	ILBAM	3.5 (0.6 %)	12 (2.0 %)
2c	OOL	6.1 (1.0 %)	16 (2.7 %)
Subtotal	Subtot.	9.3 (1.6 %)	20 (3.3 %)
3	Safety	14.4 (2.4 %)	32 (5.3 %)
Overall	Overall	23.7 (3.9 %)	50 (8.3 %)

Table B.1: Statistical analysis of events excluded from the calculation of the intra bunch-train arrival time jitter.

Figure B.1 shows the individual occurrence numbers for each of the measurements done with different feedback parameter settings. The first three categories show a uniform distribution as expected for random events. For the next three categories more suspicious events occur with higher field weighting and lower beam weighting values, indicating that the cause of these instabilities is related to the feedback acting on the field. This pattern is also propagated to the totalised numbers.

After identifying and excluding problematic events, the data analysis has been continued in the following way:

- Use the last 540 good events (of the ones not filtered out) for the calculation of the intra bunch-train arrival time jitter. The reason for using the last events is to grant the system a bit more adaptation time.

- Flat top selection: use the bunches starting from bunch number 10 (time needed for the intra-train feedback adaptation) until the end of the train $\Rightarrow$ 91 bunches per event.

- Estimation of the residual jitter over the flat top: calculate the standard deviation of the bunch arrival times (individually for each event).

- Averaging of the individual arrival time jitter values over the 540 used events.

- Division of the background jitter (beam-based feedback switched off) by the value obtained with the current feedback weighting parameters in order to obtain the improvement ⇒ this number corresponds to one data point in Figure 6.11a and Figure 6.11b on page 109. The same events have been used for the in-loop and out-of-loop calculations.

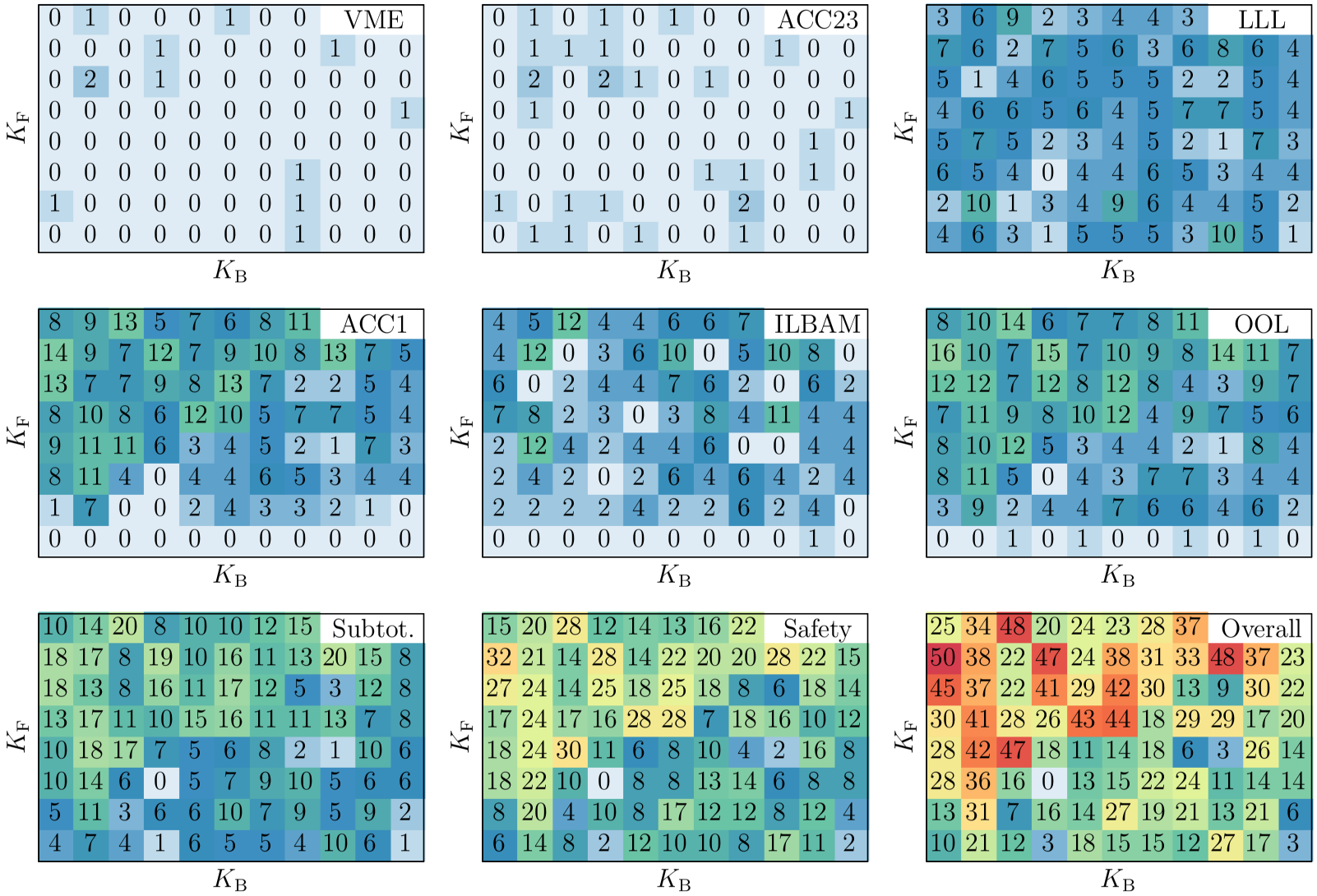

Figure B.1: Number of events needing to be excluded from further processing by category. The same data domain as in Figure 6.11a and Figure 6.11b is shown. For the meaning of the labels see Table B.1.

C RF Tweak 5 GUI Expert Windows Program Flow Logic

In section 2.2.3 and section 2.3.2, the `RF Tweak 5 GUI` diagnostics expert windows for the bunch compression and synchrotron radiation monitors have been introduced. Figure C.1 and Figure C.2 show the flow diagrams of the underlying program logic handling the interaction between the `RF Tweak 5 GUI` core, the respective detector class and the user interface. The meaning of the used shapes and colours is as follows:

◊ Diamond-shaped nodes represent events outside of the expert window, such as particle tracking taking place in the `RF Tweak 5 GUI` core, the user requesting to open a new expert window, or a measurement being scheduled to be performed by a detector class. These events either trigger an action on or are called by the expert GUI in order to calculate an updated value of a displayed quantity.

□ Rectangular nodes handle internal data structures of the expert GUI, triggered for example by the user modifying the detector settings on the panel.

⬭ Elliptical nodes are procedures running inside the expert window code.

- The signal flow direction is from top to bottom. Nodes without incoming edges are triggered by `RF Tweak 5 GUI` tracking events or user actions and must therefore be either diamond-shaped or rectangular.
- Functions are executed in serial order, no parallel processing is applied. Numbers on the edges refer to the calling order of subroutines. When a subroutine exits, the numerically next one is invoked. When there is no next one, the respective function returns to its own caller, where the same scheme applies. The execution completes when the event is fully processed.
- Solid edges are always executed, dashed and dotted edges only if the given conditions are fulfilled.
- The colours mark nodes and edges belonging to the same logical unit and distinguish different streams of cause and effect. Components that can be reached via multiple paths and are not assigned to a particular unit are drawn in black.

For details on the general concept of integrating the diagnostics monitor expert windows into `RF Tweak 5 GUI`, see section 5.5.

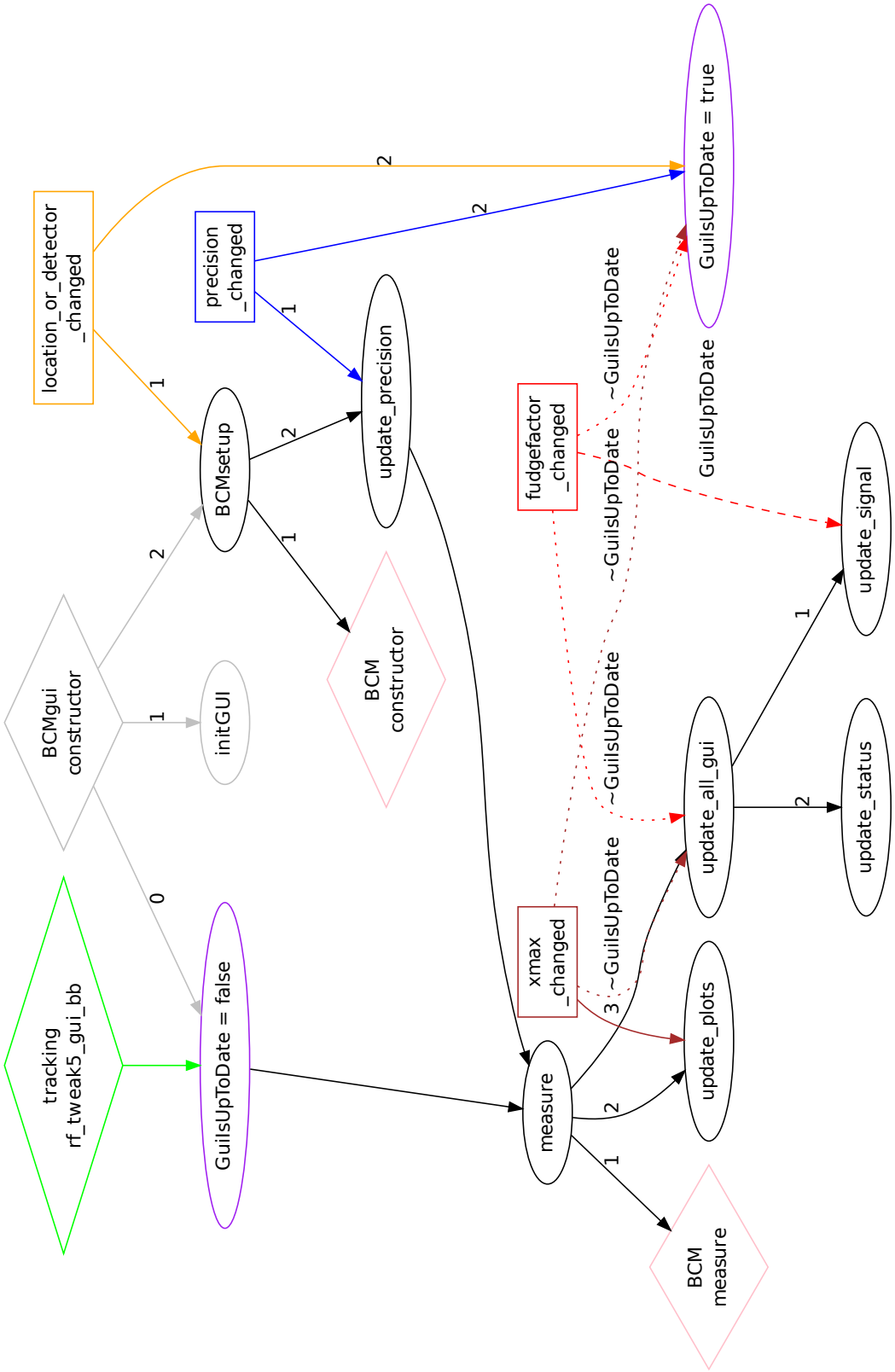

Figure C.1: Flow diagram of the bunch compression monitor expert window program logic in `RF Tweak 5 GUI`. For the meaning of the node shapes and colours, see page 155.

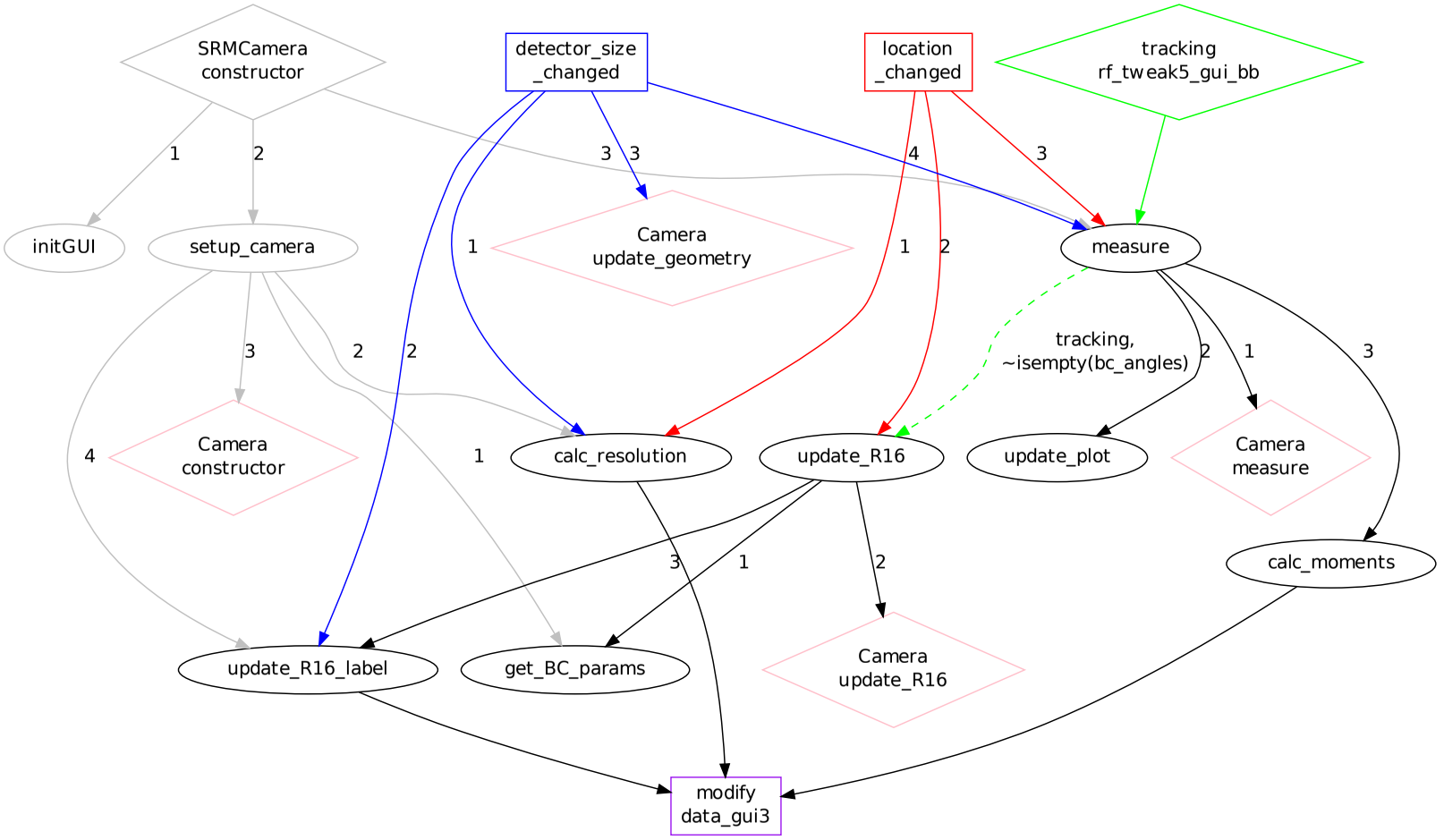

Figure C.2: Flow diagram of the synchrotron radiation monitor expert window program logic in `RF Tweak 5 GUI`. For the meaning of the node shapes and colours, see page 155.

Bibliography

[AAB+15] V. Ayvazyan, S. Ackermann, J. Branlard, B. Faatz, M. Grecki, O. Hensler, S. Pfeiffer, H. Schlarb, C. Schmidt, M. Scholz, S. Schreiber, and A. Piotrowski, *Low Level RF Control Implementation and Simultaneous Operation of Two FEL Undulator Beamlines at FLASH*, Proceedings of ICALEPCS2015, Melbourne, Australia, 2015, pp. 42–45.

[ABB+16] A. Aschikhin, C. Behrens, S. Bohlen, J. Dale, N. Delbos, L. di Lucchio, E. Elsen, J.-H. Erbe, M. Felber, B. Foster, L. Goldberg, J. Grebenyuk, J.-N. Gruse, B. Hidding, Z. Hu, S. Karstensen, A. Knetsch, O. Kononenko, V. Libov, K. Ludwig, A. R. Maier, A. Martinez de la Ossa, T. Mehrling, C. A. J. Palmer, F. Pannek, L. Schaper, H. Schlarb, B. Schmidt, S. Schreiber, J.-P. Schwinkendorf, H. Steel, M. Streeter, G. Tauscher, V. Wacker, S. Weichert, S. Wunderlich, J. Zemella, and J. Osterhoff, *The FLASHForward facility at DESY*, Nuclear Instruments and Methods in Physics Research A **806** (2016), 175–183, doi:10.1016/j.nima.2015.10.005.

[Agia] Agiltron, Inc., *CrystaLatch^{TM} 1×2 Fiberoptic PM Switch*, Data sheet.

[Agib] ———, *etMEMS^{TM} 1×1, 1×2 Square Column Fiberoptic Switch*, Data sheet.

[Agic] ———, *LightBend^{TM} 2×2 PM High Power OptoMechanical Fiberoptic Switch*, Data sheet.

[Agid] ———, *NanoSpeed^{TM} 1×2 Fiberoptic Switch*, Data sheet.

[BBF+12] M. Bousonville, M. K. Bock, M. Felber, T. Ladwig, T. Lamb, H. Schlarb, S. Schulz, C. Sydlo, S. Hunziker, P. Kownacki, and S. Jablonski, *New Phase Stable Optical Fiber*, Proceedings of BIW2012, Newport News, VA USA, 2012, pp. 101–103.

[BDD15] B. Beutner, M. Dohlus, and H. Dinter, *RFTweak 5 – An Efficient Longitudinal Beam Dynamics Code*, Proceedings of FEL2015, Daejeon, Korea, 2015, pp. 176–180.

[Boc12] M. K. Bock, *Measuring the Electron Bunch Timing with Femtosecond Resolution at FLASH*, Ph.D. thesis, Universität Hamburg, 2012.

[Bou11] M. Bousonville, *Fiber Drift Measurement*, DESY Internal Measurement Protocol, Hamburg, Germany, 2011.

[Cas03] P. Castro, *Beam Trajectory Calculations in Bunch Compressors of TTF2*, Tech. report, Dt. Elektronen-Synchrotron DESY, 2003.

[CGS+13] M. K. Czwalinna, C. Gerth, H. Schlarb, S. Bou Habib, S. Korolczuk, J. Szewinski, and A. Kuhl, *New Design of the 40 GHz Bunch Arrival Time Monitor Using MTCA.4 Electronics at FLASH and for the European XFEL*, Proceedings of IBIC2013, Oxford, UK, 2013, pp. 749–752.

[Cid96] P. E. Ciddor, *Refractive index of air: new equations for the visible and near infrared*, Appl. Opt. **35** (1996), no. 9, 1566–1573.

[CMTZ13] A. W. Chao, K. H. Mess, M. Tigner, and F. Zimmermann (eds.), *Handbook of accelerator physics and engineering; 2nd ed.*, World Scientific, Hackensack, 2013.

[CSS05] S. Casalbuoni, B. Schmidt, and P. Schmüser, *Far-Infrared Transition and Diffraction Radiation Part I: Production, Diffraction Effects and Optical Propagation*, TESLA Report **15** (2005).

[CSS+09] S. Casalbuoni, B. Schmidt, P. Schmüser, V. Arsov, and S. Wesch, *Ultrabroadband terahertz source and beamline based on coherent transition radiation*, Phys. Rev. ST Accel. Beams **12** (2009), 030705, doi:10.1103/PhysRevSTAB.12.030705.

[Czw] M. K. Czwalinna, private communication.

[DCG+15] H. Dinter, M. K. Czwalinna, C. Gerth, K. Przygoda, R. Rybaniec, H. Schlarb, and C. Sydlo, *Prototype of the Improved Electro-Optical Unit for the Bunch Arrival Time Monitors at FLASH and the European XFEL*, Proceedings of FEL2015, Daejeon, Korea, 2015, pp. 478–482.

[Deu17a] Deutsches Elektronen-Synchrotron, *FLASH Accelerator*, https://flash.desy.de/accelerator/, 2017.

[Deu17b] ———, *Free-Electron Laser FLASH*, https://flash.desy.de/, 2017.

[DiC] DiCon Fiberoptics, Inc., *PM MEMS 1xN Optical Switch*, Data sheet.

[DL13] W. Decking and T. Limberg, *European XFEL Post-TDR Description*, Tech. Report XFEL.EU TN-2013-004, 2013.

[Flö17] K. Flöttmann, *ASTRA: A Space Charge Tracking Algorithm*, https://www.desy.de/~mpyflo/, 2017.

[FLP01] K. Flöttmann, T. Limberg, and P. Piot, *Generation of Ultrashort Electron Bunches by cancellation of nonlinear distortions in the longitudinal phase space*, TESLA-FEL **6** (2001).

[FZL+13] G. Feng, I. Zagorodnov, T. Limberg, H. Jin, Y. Kot, M. Dohlus, and W. Decking, *Beam Dynamics Simulations for European XFEL*, TESLA-FEL **4** (2013).

[GBH+12] C. Gerth, M. K. Bock, M. Hoffmann, F. Ludwig, H. Schlarb, and C. Schmidt, *Beam Energy Measurements in the FLASH Injector Using Synchrotron Radiation and Bunch Arrival Monitors*, Proceedings of FEL2011, Shanghai, China, 2012, pp. 489–492.

[Ger] C. Gerth, private communication.

[Ger07] ———, *Synchrotron Radiation Monitor for Energy Spectrum Measurements in the Bunch Compressor at FLASH*, Proceedings of DIPAC 2007, Venice, Italy, 2007, pp. 150–152.

[Gri07] O. Grimm, *Coherent Radiation Diagnostics for Short Bunches*, Proceedings of PAC07, Albuquerque, New Mexico, USA, 2007, pp. 2653–2657.

[HZ13] M. Hamberg and V. Ziemann, *Status of the EU-XFEL Laser Heater*, Proceedings of FEL2013, New York, NY, USA, 2013, pp. 271–275.

[KBB+10] W. Koprek, C. Behrens, M. K. Bock, M. Felber, P. Gessler, K. Hacker, H. Schlarb, C. Schmidt, B. Steffen, S. Wesch, S. Schulz, and J. Szewinski, *Intra-Train Longitudinal Feedback for Beam Stabilization at FLASH*, Proceedings of FEL2010, Malmö, Sweden, 2010, pp. 537–543.

[KS14] R. Kammering and C. Schmidt, *Feedbacks and Automation at the Free Electron Laser in Hamburg (FLASH)*, Proceedings of ICALEPCS2013, San Francisco, CA, USA, 2014, pp. 1345–1347.

[LAF+10] F. Löhl, V. Arsov, M. Felber, K. Hacker, W. Jalmuzna, B. Lorbeer, F. Ludwig, K.-H. Matthiesen, H. Schlarb, B. Schmidt, P. Schmüser, S. Schulz, J. Szewinski, A. Winter, and J. Zemella, *Electron Bunch Timing with Femtosecond Precision in a Superconducting Free-Electron Laser*, Phys. Rev. Lett. **104** (2010), 144801, doi:10.1103/PhysRevLett.104.144801.

[Lam17] T. Lamb, *Laser-to-RF Phase Detection with Femtosecond Precision for Remote Reference Phase Stabilization in Particle Accelerators*, Ph.D. thesis, Technische Universität Hamburg-Harburg, 2017.

[Löh09] F. Löhl, *Optical Synchronization of a Free-Electron Laser with Femtosecond Precision*, Ph.D. thesis, Universität Hamburg, 2009.

[Mee] Meerstetter Engineering GmbH, *Thermo Electric Cooling Temperature Controller TEC-1091*, Data sheet.

[NLSH12] E. Negodin, J. Liebing, H. Sokolinski, and M. Hoffmann, *Technische Spezifikation der Elektronikracks für den XFEL-Tunnel*, Tech. report, Deutsches Elektronen-Synchrotron, 2012.

[OK15] F. Obier and J. Kahl, *FLASH2 Extraction*, Accelerators 2014. Highlights and Annual Report, Deutsches Elektronen-Synchrotron DESY, Hamburg, Germany, 2015, pp. 40–41.

[OWI] OWIS GmbH, *Hochpräzisions-Lineartische LIMES 60*, Data sheet.

[OZ] OZ Optics Ltd., *Polarization Maintaining and Singlemode Fiber Optic Switches*, Data sheet.

[PBB+17] S. Pfeiffer, N.-I. Baboi, J. Branlard, L. Butkowski, M. K. Czwalinna, H. Dinter, C. Engling, K. Flöttmann, C. Gerth, O. Hensler, M. Hierholzer, M. Hoffmann, K. Honkavaara, M. Hüning, R. Jonas, M. Körfer, S. Lederer, L. Lilje, C. Martens, N. Mildner, R. Neumann, A. Petrov, M. Pröll, H. Schlarb, C. Schmidt, S. Schreiber, F.-R. Ullrich, S. Vilcins-Czvitkovits, M. Vogt, A. de Zubiaurre Wagner, J. Zemella, and M. Fakhari, *Renewal and upgrade of the fast beam-based feedback system at FLASH*, LLRF2017 workshop, Barcelona, Spain, 2017, `http://www.llrf2017.org/pdf/Posters/P-03.pdf`.

[PBC+16] K. Przygoda, L. Butkowski, M. K. Czwalinna, H. Dinter, C. Gerth, E. Janas, F. Ludwig, S. Pfeiffer, H. Schlarb, C. Schmidt, M. Viti, and R. Rybaniec, *MicroTCA.4 Based Optical Frontend Readout Electronics and its Applications*, Proceedings of IBIC2016, Barcelona, Spain, 2016, pp. 67–70.

[PDG14] P. Peier, H. Dinter, and C. Gerth, *Coherent Radiation Diagnostics for Longitudinal Bunch Characterization at European XFEL*, Proceedings of FEL2014, Basel, Switzerland, 2014, pp. 925–928.

[Pei13] P. Peier, *Coherent Longitudinal Diagnostics for European XFEL*, `https://wof-cluster.desy.de/sites2009/site_msk/content/localfsExplorer_read?currentPath=/afs/desy.de/group/msk/www/html/gseminar/Seminar2013/2013_11_01-P.Peier-LongitudinalBeamDiagnostics.pdf`, 2013.

[Pfe14] S. Pfeiffer, *Symmetric Grey Box Identification and Distributed Beam-Based Controller Design for Free-Electron Lasers*, Ph.D. thesis, Technische Universität Hamburg-Harburg, 2014.

[Pfe18] ———, *BACCA (Bunch Arrival Corrector CAvity)*, https://wof-cluster.desy.de/sites2009/site_msk/content/localfsExplorer_read?currentPath=/afs/desy.de/group/msk/www/html/gseminar/Seminar2018/2018_03_16-S-Pfeiffer-BACCA.pdf, 2018.

[Pol17] M. Polyanskiy, *Python scripts for refractiveindex.info database: Ciddor 1996 – air*, https://raw.githubusercontent.com/polyanskiy/refractiveindex.info-scripts/master/scripts/Ciddor%201996%20-%20air.py, 2017.

[SBB+17] E. Savelyev, R. Boll, C. Bomme, N. Schirmel, H. Redlin, B. Erk, S. Düsterer, E. Müller, H. Höppner, S. Toleikis, J. Müller, M. K. Czwalinna, R. Treusch, T. Kierspel, T. Mullins, S. Trippel, J. Wiese, J. Küpper, F. Braußе, F. Krecinic, A. Rouzée, P. Rudawski, P. Johnsson, K. Amini, A. Lauer, M. Burt, M. Brouard, L. Christensen, J. Thøgersen, H. Stapelfeldt, N. Berrah, M. Müller, A. Ulmer, S. Techert, A. Rudenko, and D. Rolles, *Jitter-correction for IR/UV-XUV pump-probe experiments at the FLASH free-electron laser*, New Journal of Physics **19** (2017), no. 4, 043009, doi:10.1088/1367-2630/aa652d.

[SCF+13] C. Sydlo, M. K. Czwalinna, M. Felber, C. Gerth, T. Lamb, H. Schlarb, S. Schulz, F. Zummack, and S. Jablonski, *Development Status of Optical Synchronization for the European XFEL*, Proceedings of IBIC2013, Oxford, UK, 2013, pp. 135–138.

[Sch10] C. Schmidt, *RF System Modeling and Controller Design for the European XFEL*, Ph.D. thesis, Technische Universität Hamburg-Harburg, 2010.

[SDF+12] M. Scholz, W. Decking, B. Faatz, T. Limberg, and B. Liu, *Extraction Arc for FLASH2*, Proceedings of FEL2011, Shanghai, China, 2012, pp. 601–604.

[SGB+15] S. Schulz, I. Grguraš, C. Behrens, H. Bromberger, J. T. Costello, M. K. Czwalinna, M. Felber, M. C. Hoffmann, M. Ilchen, H. Y. Liu, T. Mazza, M. Meyer, S. Pfeiffer, P. Prędki, S. Schefer, C. Schmidt, U. Wegner, H. Schlarb, and A. L. Cavalieri, *Femtosecond all-optical synchronization of an X-ray free-electron laser*, Nature communications **6** (2015), 5938, doi:10.1038/ncomms6938.

[SLP+08] J. Skupin, Y. Li, J. Pflüger, B. Faatz, and T. Vielitz, *Undulator Demagnetization due to Radiation Losses at FLASH*, Proceedings of EPAC08, Genoa, Italy, 2008, pp. 2308–2310.

[SNF+07] J. R. Schneider, R. H. Nielsen, J. Feldhaus, B. Keitel, W. Laasch, P. Schmüser, B. Sonntag, and K. Tiedtke, *FLASH. The Free-Electron*

Laser in Hamburg, Deutsches Elektronen-Synchrotron DESY, Hamburg, Germany, 2007.

[SY11] E. A. Schneidmiller and M. V. Yurkov, *Photon Beam Properties at the European XFEL*, Tech. report, 2011.

[Tan13] T. Tantau, *Graph Drawing in TikZ*, Journal of Graph Algorithms and Applications **17** (2013), no. 4, 495–513, doi:10.7155/jgaa.00301.

[VCD+17a] M. Viti, M. K. Czwalinna, H. Dinter, C. Gerth, K. Przygoda, R. Rybaniec, and H. Schlarb, *The Bunch Arrival Time Monitor at FLASH and European XFEL*, Proceedings of ICALEPCS2017, Barcelona, Spain, 2017, pp. 701–705.

[VCD+17b] M. Viti, M. K. Czwalinna, H. Dinter, C. Gerth, K. Przygoda, R. Rybaniec, and H. Schlarb, *Recent Upgrades of the Bunch Arrival Time Monitors at FLASH and European XFEL*, Proceedings of IPAC2017, Copenhagen, Denmark, 2017, pp. 695–698.

[Wes12] S. Wesch, *Echtzeitbestimmung longitudinaler Elektronenstrahlparameter mittels absoluter Intensitäts- und Spektralmessung einzelner kohärenter THz-Strahlungspulse*, Ph.D. thesis, Universität Hamburg, 2012.

[WG09] A. Wilhelm and C. Gerth, *Synchrotron Radiation Monitor for Bunch-Resolved Beam Energy Measurements at FLASH*, Proceedings of DIPAC09, Basel, Switzerland, 2009.

[Wie03] H. Wiedemann, *Synchrotron Radiation*, Advanced texts in physics, Springer, Berlin, 2003.

[Wun16] S. Wunderlich, *Development and Commissioning of a Double-Prism Spectrometer for the Diagnosis of Femtosecond Electron Bunches*, Ph.D. thesis, Universität Hamburg, 2016.

[Yan16] M. Yan, *Online Diagnostics of Time-Resolved Electron Beam Properties with Femtosecond Resolution for X-Ray FELs*, Ph.D. thesis, Universität Hamburg, 2016.

[Zag13] I. Zagorodnov, *Particle Distributions for Start-to-End Simulations for FLASH I, 500 pC*, https://www.desy.de/fel-beam/s2e/flash/Nominal/flashI/nom500pC.html, 2013.

Acknowledgements

I would like to express my sincere gratitude to:

Prof. Dr. Florian Grüner and PD Dr. Bernhard Schmidt,

Dr. Holger Schlarb and Dr. Christopher Gerth,

Dr. Marie Kristin Czwalinna,

Dr. Sven Pfeiffer and Dr. Christian Schmidt,

Dr. Peter Peier, Dr. Bernd Steffen and Dr. Franziska Frei

Dr. Bolko Beutner, Dr. Martin Dohlus, Dr. Winfried Decking and DESY's MPY group,

Dr. Frank Ludwig, Dr. Matthias Hoffmann and Dr. Michele Viti,

Dr. Minjie Yan, Eugen Hass, Dr. Steffen Wunderlich and Dr. Michael Kuntzsch,

Dr. Cezary Sydlo, Falco Zummack and Matthias Felber,

Martin Schäfer, Nicole Leuschner, Jan Roever and Bartlomiej Szczepanski,

the entire FLASH team,

all shift colleagues,

my colleagues at DESY's MSK group,

my fellow PhD students and

my family and friends.

Eidesstattliche Versicherung / Declaration on oath

Hiermit versichere ich an Eides statt, die vorliegende Dissertationsschrift selbst verfasst und keine anderen als die angegebenen Hilfsmittel und Quellen benutzt zu haben.

Die eingereichte schriftliche Fassung entspricht der auf dem elektronischen Speichermedium.

Die Dissertation wurde in der vorgelegten oder einer ähnlichen Form nicht schon einmal in einem früheren Promotionsverfahren angenommen oder als ungenügend beurteilt.

Hamburg, den 27. April 2018 Hannes Dinter